Absorption of Ammonia in an Ammonia + Ionic Liquid Solution

Technische Universiteit Delft

Kalyani M. Peshave

TU Delft
Delft
University of
Technology

Challenge the future

Absorption of Ammonia in an Ammonia + Ionic Liquid Solution

by

Kalyani M. Peshave

to obtain the degree of Master of Science
at the Delft University of Technology,
to be defended publicly on Thursday December 19, 2019 at 14:00 PM.

Student number:	4701631	
Project duration:	April 10, 2019 - December 19, 2019	
Thesis committee:	Dr. Ir. C. A. Infante Ferreira,	TU Delft, supervisor
	Prof. Dr. T. J. H. Vlugt	TU Delft
	Dr. R. Delfos	TU Delft
	Ir. V. Gudjonsdottir	TU Delft

God does not play dice with the universe.

- Albert Einstein

Happiness can be found, even in the darkest of times, if one only remembers to turn on the light.

- Albus Dumbledore

Summary

Excessive consumption of non - renewable resources in the recent times has negative effects on the environment, one of the important of which include global warming. This suggests an urgent need for adaption to the sustainable use of the resources, for which the thermal technologies show a lot of scope. Absorption heat pump is a type of heat pump which uses a thermal compressor instead of a mechanical compressor as in the case for the conventional heat pumps. Thus, such heat pumps are indeed an alternative energy conversion technology. This thesis focuses on the use of an inventive fluid as an absorbent in the absorption thermodynamic cycles : ionic liquids.

In this thesis, the process of absorption of NH_3 into an NH_3 + ionic liquid solution is studied. [emim][SCN] was selected as the ionic liquid to be used as an absorbent based on it's efficiency, availability and the beneficial economic factors. In the first part of this thesis, an existing numerical vapor - liquid equilibrium model for the working pair of NH_3 - [emim][SCN] developed by Wang (2019) was validated. This is done by comparing the results of the model with the experimental data obtained by Yokozeki and Shiflett (2007) for the same working pair.

The second part of this thesis includes experimental and numerical studies of the absorption process in question. For the experimental study, the absorption setup located in Process and Energy laboratory at TU Delft was used. This setup does not accommodate the complete absorption heat pump thermodynamic cycle, but just the absorption process. Firstly, H_2O - H_2O convective heat transfer experiments were performed inside the setup, for both the lower range Reynolds numbers (40-140), and for the higher range Reynolds numbers (150-360). It was ascertained that the derived correlations governing the heat transfer for both of these ranges, along with the average correlation covering all the ranges of the Reynolds number, agree with the previous literature, to ascertain that the setup worked correctly. Consecutively, the absorption experiments were performed with NH_3 - [emim][SCN] working pair. The amount of vapor flow recorded during these experiments was quite low (maximum upto 0.1%), suggesting that most of the heat was transferred to the cooling water by means of the sensible heat transfer.

A numerical model for the absorption + sensible heat transfer process developed by Wang (2019) was used as a reference to design a similar numerical model in the present work. The data obtained from the experiments was used as an input to the numerical model. It was observed that the overall heat transfer coefficient for the absorption process is indeed more than that for the convective heat transfer process. The numerical results agree with the experimental results including a moderate error margin. Therefore, the numerical model was considered validated. The conceptual reasoning behind the error margin between the numerical and the experimental results are also presented. Little can be said about the validity of the empirical correlations governing the absorption process estimated by Wang (2019), since absorption only took place during a small part of the length of the absorber (maximum 10.5%). However, it is expected that these correlations work satisfactorily for those cases where the solution is subcooled before entering the absorber. It is concluded based on the numerical results that the correlation governing the convective heat transfer derived from the water - water experiments is considered acceptable for the present case.

Finally in the last part of this thesis, an attempt was made to predict the accurate value for the viscosity of NH_3 + [emim][SCN] solution by an experimental study. A separate set of convective heat transfer experiments was performed with NH_3 + [emim][SCN] solution and the cooling water. The experimental data obtained was analyzed using the correlations obtained from the H_2O - H_2O convective heat transfer experiments. The results of this analysis were compared with the solution viscosity values predicted by Wang (2019) with a logarithmic correlation, wherein the solution viscosity is a logarithmic function of the viscosities of the individual fluids present in the solution. The reasonable agreement (with on an average 32.05 % accuracy, as was estimated by Wang (2019)) between the viscosity values obtained by the analysis and the values predicted by Wang (2019) confirmed the validity of this logarithmic function. Recommendations are presented in the last part of this thesis for future studies.

Acknowledgement

I would sincerely like to thank Dr. Carlos Infante Ferreira for supervising my thesis work. He was always supportive and kind. He offered me his expert advice at every stage of my thesis. He appreciated my work and encouraged me to improve constantly. I am immensely grateful for the confidence he showed in me. I owe a great deal of the success of completion of the project to him.

I also acknowledge the help and guidance from Dr. Meng Wang, who kindly lent me his research as a reference, for my thesis. His guidance with the Matlab codes that were designed in this work, proved priceless. He provided me with the technical guidance despite being far away from TU Delft, which led me to the successful completion of my thesis.

I would like to thank the students of Bachelors of Science at the TU Delft- Boyan Klifman, Bram Oude Aarninkhof, Frank Schilperoort, Nico Franco Pinto and Sabet Rahro. They provided friendly support in all the stages of my thesis. They also offered their guidance during the experimentation for the project.

I appreciate the strong support and constant encouragement from my parents. They always edged me forward and inspired me to improve with their own example. My brother and my sister-in-law, being in the same education line as me, always provided me with their technical help, support and love. I am not to forget the constant love and support from the rest of my family in India, as they are always parental to me. I am also not to forget my friends in the Netherlands, who were always there for me and helped me in the technical bits of the project, Siddharth Kalra, Marlinda Bauer, Shweta Kamble, Gayatri Mujumdaar, Maaike Leichsenring, Fenna Westserbaan van der Meij.

All of these people undoubtedly share the credit for the completion of my Masters thesis at TU Delft.

Contents

List of Symbols

A	Area (m^2)
b	Corrugation depth of the absorber (m)
c	Concentration (kmol m^{-3})
COP	Coefficient of Performance (-)
c_p	Specific heat (J $kg^{-1}K^{-1}$)
D	Mass diffusivity (m^2s^{-1})
d	diameter (m)
F	Objective function (-)
f	Circulation ratio (-)
G	A parameter in NRTL model (-)
$\dot{G}$	Mass flux (kg $m^{-2}s^{-1}$)
G^e	Excess Gibb's energy (J sec^{-1})
h	Enthalpy (J kg^{-1})
$\hat{h}$	Component partial enthalpy (J kg^{-1})
$LMTD$	Logarithmic Mean Temperature Difference (K, °C)
L	Length (m)
L_v	Vapor port - to - port length (m)
M_w	Molecular weight (g mol^{-1}, kg $kmol^{-1}$)
$\dot{m}$	Mass flow rate (kg s^{-1})
n	Number (-)
P	Pressure (kPa, MPa)
P	Pitch (m)
$\dot{Q}$	Heat duty (J s^{-1})
q	Vapor quality (-)

T	Temperature (K, °C)
t	Thickness (m)
U	Overall heat transfer coefficient (W $\mathrm{m^{-2}K^{-1}}$)
V	Volume ($\mathrm{m^3}$)
$\dot{V}$	Volume flow rate ($\mathrm{m^3s^{-1}}$)
v	Specific volume ($\mathrm{m^3kg^{-1}}$)
W	Width (m)
w	Mass concentration (kg $\mathrm{kg^{-1}}$)
x	Mole concentration (mol $\mathrm{mol^{-1}}$)

Greek symbols

α	A parameter in NRTL model (-)
$\bar{\alpha}$	Heat transfer coefficient (W $\mathrm{m^{-2}K^{-1}}$)
β	Corrugation angle (radians)
$\bar{\beta}$	Mass transfer coefficient (m $\mathrm{s^{-1}}$)
δ	Film thickness (m)
Δ	Difference (-)
ϵ	Void fraction ($\mathrm{m^3m^{-3}}$)
γ	Activity coefficient (-)
λ	Thermal conductivity (W $\mathrm{m^{-1}K^{-1}}$)
μ	Viscosity (Pa-s)
ϕ	Surface enlargement factor (-)
ρ	Density (kg $\mathrm{m^{-3}}$)
σ	Surface tension (N $\mathrm{m^{-1}}$)
τ	A parameter in NRTL model (-)

Subscripts and superscripts

A	Solvent A
abs	Absorber side
avg	Average
B	Solvent B
b	Bulk
C	Cold
c	Coolant, corrugation
ch	Channel
con	Condenser
cv	control volume
cw	Cooling water side
exp	Experimental
eva	Evaporator
g	Plate gap
gen	Generator
H	Hot
h	Hydraulic (diameter)
ht	Heat transfer
i	Inside, interface
IL	Ionic liquid
in	Going into an equipment
int	Interface
L	Liquid
lb	Liquid bulk
li	Liquid at the interface
losses	Energy losses
NH_3	Ammonia

o	Outside
out	Coming out of an equipment
p	Plate
sat	Saturated
sim	Simulated
sol	Solution
sp	Spacing
strong	Strong solution coming out of the absorber
TSB	Thermostatic bath
V, v	Vapor
vb	Vapor bulk
W	Wall
weak	Weak solution going into the absorber

Abbreviations

ABS	Absorber
CON	Condenser
EOS	Equation of state
EVA	Evaporator
FS	Full scale
GEN	Generator
HEX	Heat exchanger
NRTL	Non - random two liquid model
PC	Precooler
PHX	Plate heat exchanger
PRVdW	Peng Robinson with van der Waals mixing rules model
PRWS	Peng Robinson with Wong-Sandler mixing rules model

RD	Reading
RK	Redlich Kwong model
RMSD	Root mean square difference
SHX	Heat exchanger
TSB	Thermostatic bath
UNIFAC	UNIFAC functional group activity model
VAHP	Vapor absorption heat pump
VLE	Vapor - liquid equilibrium

Dimensionless numbers

Nusselt number	$\mathrm{Nu} = \frac{\bar{\alpha} d_h}{\lambda}$
Prandtl number	$\mathrm{Pr} = \frac{C_p \mu}{\lambda}$
Reynolds number	$\mathrm{Re} = \frac{\dot{G} d_h}{\mu}$
Schmidt number	$\mathrm{Sc} = \frac{\mu}{\rho D}$
Sherwood number	$\mathrm{Sh} = \frac{\bar{\beta} d_h}{D}$

1

Introduction

1.1. Background

About 50% of the total energy demand in Europe falls into heating and cooling sector. Heat pumps are conventional means to create and exploit heat. Most usage of the heat pumps lies in industrial sector as well as in the residential energy sector. There is a wide variety of heat pumps that can satisfy the need of space heating and cooling, whether in industrial or residential sector.

A heat pump functions based on a well known thermodynamic concept of the transfer of the thermal energy from a source of the system to the sink of the system. A heat pump cycle makes use of a compressor and an expansion valve in order to achieve the required pressure and temperature gradients. Working fluid is passed through a compressor. Thus the fluid at high pressure passes to the condenser where it gives off the heat and cools down. It is then passed through the expansion valve to relieve it's pressure, and then, gets heated up in the evaporator thus consuming the heat from the surroundings. Thus, useful thermal energy is collected at the condenser.

Figure below shows the simple outline of the working of a heat pump.

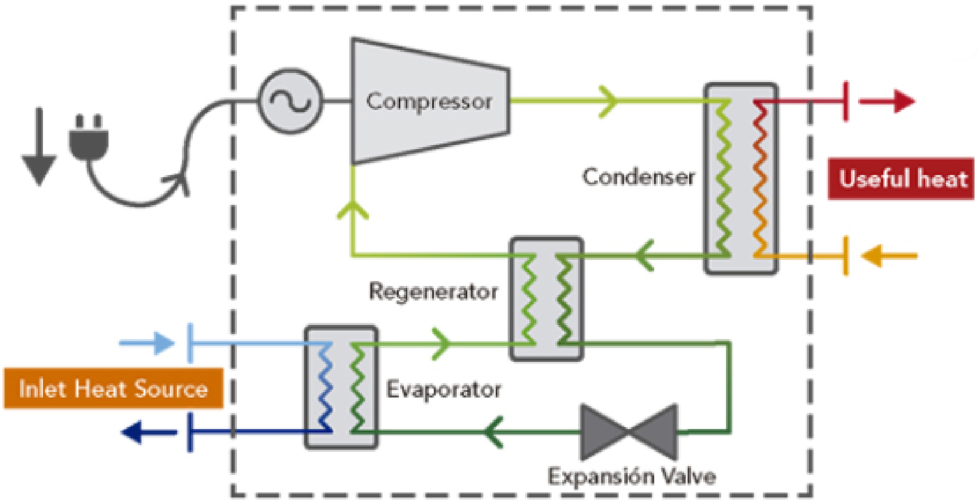

Figure 1.1: Schematic of the working of a heat pump (Images.google.com. (2019))

A heat pump cycle is displayed in figure 1.2, in terms of a Pv diagram.

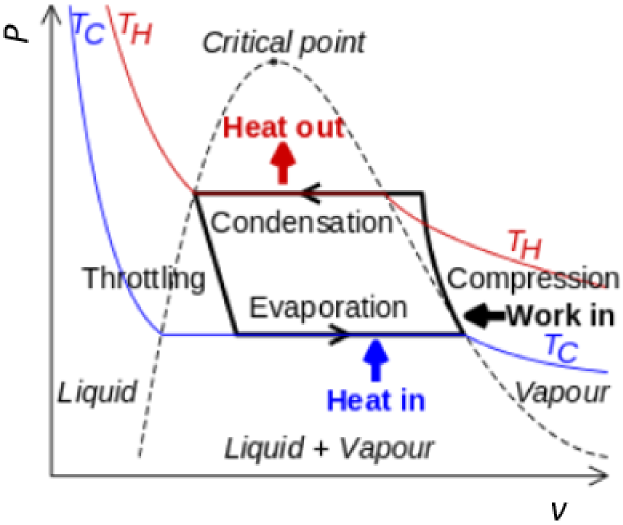

Figure 1.2: A heat pump cycle : *Pv* diagram (Images.google.com. (2019))

1.2. Why absorption heat pumps?

Every action of humankind has consequences on the environment, either beneficial or destructive. Excessive consumption of non renewable resources has negative effects on the environment, one of the important ones include global warming. A research conducted by the NASA's Goddard Institute for Space Studies (GISS), states that the average global temperature of the Earth has increased by about 0.8 °C since 1880. This global temperature mainly depends on how much the energy does the Earth receive from the Sun, and how much does it radiate back. This radiation of the energy by the Earth depends on the chemical composition of the atmosphere around it, and hence, on the amount of the greenhouse gases around the Earth that trap this energy. These greenhouse gases around the Earth's atmosphere mainly include water vapor, carbon dioxide, methane, nitrous oxides and ozone. There is no doubt that human activities have a huge contribution to the increase of carbon dioxide in the atmosphere.

A large amount of the atmospheric carbon dioxide emissions are caused due to the combustion of the fossil fuels, mainly oil, coal and natural gas. Human activities like the deforestation, change in the use of the land and industrial processes also contribute to the carbon emission. A carbon footprint is defined as the amount of the greenhouse gases emitted into the atmosphere to suit human activities, usually also represented in tons of carbon dioxide. It is of utmost importance to take the necessary measures in order to reduce the carbon footprint to help slow down or curb the climate change that is progressing rapidly as a result of the human activities. One of the important ways to achieve this is to replace the usage of non renewable resources with the usage of the renewable ones. It is only fair that the future generations of humankind should get to exploit the natural resources as the current generations do. All this dictates the urgent need to use resources like fossil fuels sparingly. This would in turn reduce the risk of the global warming by reducing the emission of greenhouse gases.

There is a great potential in the thermal energy sector to achieve the goal of sparing the consumption of natural resources. Figure 1.3 shows the thermal energy consumption in the Netherlands for space heating an space cooling purposes. In 2015, in the Netherlands, the thermal energy used was about 939 PJ (about 45 %) of the total energy consumption of the Netherlands in 2015 (Wang, 2019). This usage is expected to be reduced to 867 PJ by 2030 (Wang, 2019). It is clear from figure 1.3, that this reduction is expected to be achieved mainly by the built environment.

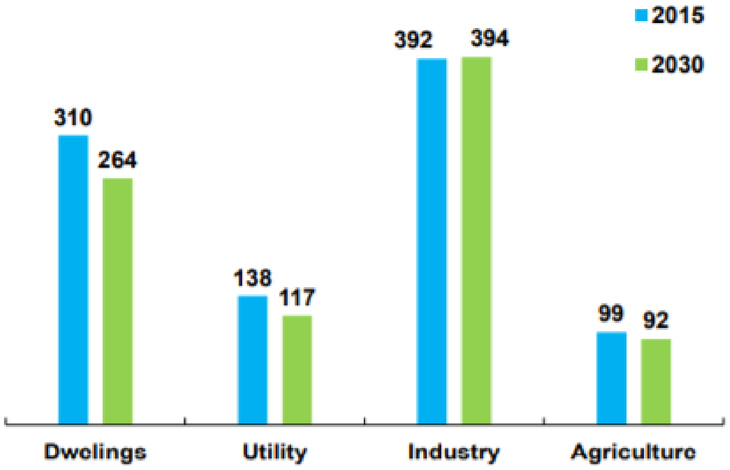

Figure 1.3: Thermal energy used in 2015 and expected to be used in 2030 in the Netherlands (Wang, 2019)

So, thermal technologies show a lot of scope for a sustainable design to be used in the buildings, in order to achieve the goal of the energy conservation. Absorption heat pump is a type of heat pump which produces heat output on being given heat input, using a thermal compressor instead of a mechanical compressor as in case of the conventional heat pumps. Thus, such heat pumps are indeed an alternative energy conversion technology. Most of such absorption heat pumps use NH_3 - H_2O or H_2O - LiBr as a working pair. Functioning of such absorption heat pumps is described below.

1.2.1. Vapor Absorption Heat Pump (VAHP) cycle

Principle

Absorption cycles of the type Vapor Absorption Heat Pump (VAHP) are considered and studied in this work. The working fluids in such cycles are a refrigerant and an absorbent fluid. Figure 1.4 displays the schematic of a VAHP cycle. As shown in figure 1.4, the pure refrigerant vapor from the evaporator (EVA) is absorbed in the absorbent fluid in absorber (ABS), thus making the solution in the absorber the strong solution. This strong solution passes through the heat exchanger (SHX), thus taking up the heat from the hot weak solution passing through the exchanger. This strong solution then enters the generator (GEN), where some heat is provided to it thus making the refrigerant in the solution to evaporate and be sent to the condenser (CON) where it gets cooled. The weak solution that comes out of the generator passes back to the heat exchanger and gets cooled, after which it enters the absorber again and the cycle continues. After the condenser, refrigerant is throttled and enters the evaporator (EVA) where it cools the surroundings. Thus, the cooling effect is achieved at the evaporator. When the refrigerant vapour is absorbed into the solution inside the absorber, temperature of the solution increases. This heat can be transferred to the coolant and used. Also, at the condenser, the refrigerant gives off heat. Thus, in the overall cycle, heating effect is achieved at the condenser and absorber.

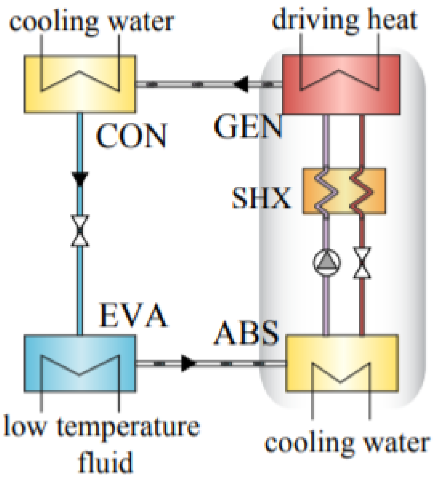

Figure 1.4: Vapor Absorption Refrigeration cycle (Wang, 2019)

Single effect VAHP cycle is considered in this work. Coefficient of performance of such a cycle is calculated as follows

$$COP = \frac{\dot{Q}_{\text{abs}} + \dot{Q}_{\text{con}}}{\dot{Q}_{\text{gen}}} = \frac{\dot{Q}_{\text{eva}} + \dot{Q}_{\text{gen}}}{\dot{Q}_{\text{gen}}} = 1 + \frac{\dot{Q}_{\text{eva}}}{\dot{Q}_{\text{gen}}} \tag{1.1}$$

Thermodynamic *PT* diagram of this cycle is shown in the figure 1.5.

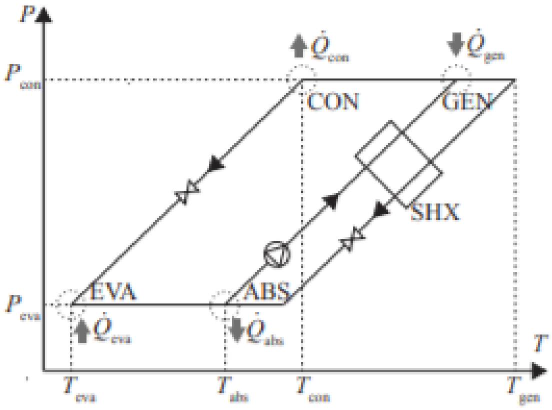

Figure 1.5: *PT* diagram of Vapour Absorption Heat Pump cycle (Wang, 2019)

Advantages of Vapour Absorption Heat Pump (VAHP) cycles over Vapour Compression Heat Pump (VCHP) cycles

1. In VAHP cycles, use of a mechanical compressor is avoided and it is replaced by the use of thermal compression. The driving force of this type of cycles is the heat that is provided to the generator. Thus, all the input needed is the heat input needed for the generator.
2. Coefficient of Performance (COP) of the overall cycle when this thermal compressor is used in the heat pump cycle, is found to be comparable with that obtained when a mechanical compressor is used.
3. Degradation of the cycle performance due to the damage to a mechanical compressor can alltogether be avoided when a thermal compressor is used in it's place.

Working fluids

The performance of such VAHP cycles depends highly on the choice of the working fluids. Thus, making an appropriate choice of the refrigerant and the absorbent fluid is of utmost importance, taking into the consideration the physical and thermodynamic properties of both. In most cases, water or LiBr is used as the absorbent fluid in VAHP cycles. NH_3 - H_2O or H_2O - LiBr perform considerably good in such cycles. However, there are some disadvantages associated with the use of these working fluid pairs.

1. Water cannot be cooled below 0 ° C.
2. Use of H_2O - LiBr pair has a risk of corroding the equipment.
3. When the temperature window of *PT* diagram is high, H_2O - LiBr pair may solidify.
4. The boiling point of NH_3 is close to that of water, so the vapour stream may contain some water as well. This will negatively impact the performance of the cycle. This implies that in order to remove water vapour from ammonia vapor, a rectifier should be used, which makes the system bulky, and reduces it's efficiency.

Use of ammonia in refrigeration cycles dates way back. Ammonia has a low freezing point (-33 ° C). It has relatively high latent heat, which justifies it's use in the refrigeration and absorption cycles. It also has low viscosity. Thus, it is of utmost importance to choose an absorbent fluid which has high affinity with ammonia. Some of such fluids include salts such as NaSCN and $LiNO_3$. However, such salts have high viscosities. These salts can also crystallize during the operation.

When it comes to the exploration of the concept of the use of the ionic liquids as a substitute for water or LiBr in VAHP cycles, it is seen that the high viscosity of ionic liquids can be considered against the use of them in absorption heat pump cycles. However, some other properties like hydrophilic nature, and low melting points of ionic liquids also make them attractive for their use in heat cycles. Since the ionic liquids have low melting point, they remain in liquid state at normal working temperatures. Hence, this property works in favour of their selection for the absorption processes. Ionic liquids also have negligible vapour pressures, making them further practical for use in absorption processes.

1.3. Research questions

This work focuses on the following research questions,

1. Estimation of the validity of the thermodynamic properties of the fluids in question.

   For this purpose, the vapour liquid equilibrium model designed by Wang (2019) is tested in comparison with the experimental data by Yokozeki and Shiflett (2007). It is found out whether or not the VLE model in question comes close to this experimental data. By doing this, further use of this VLE model in this work is justified.

2. Estimation of the validity of the relation used by Wang (2019) for the viscosity of the ammonia + [emim][SCN] solution as a logarithmic function of the individual fluid viscosities.

   For this purpose, the logarithmic viscosity relation in question is tested with help of experimental data. For this purpose, a separate set of sensible heat transfer experiments was performed with ammonia + [emim][SCN] solution being cooled by water. Accuracy of the viscosity calculated by the logarithmic relation in question is determined, with the help of the values of the solution viscosity obtained from the experiments.

3. Validation of the heat and mass transfer model developed by Wang (2019) for the absorption + convective heat transfer process in a plate heat exchanger.

   For this purpose, the experimental results are used as input values to a numerical model developed in Matlab, in order to obtain the output conditions of the absorber.

   (a) A setup at the Energy and Process department of the Delft University of Technology is used for the experiments. Firstly, two sets of water-water experiments without a phase change are performed, and an empirical correlation governing the convective heat transfer is derived. This correlation is a function of Nusselt, Reynolds, and Prandtl numbers.

(b) Afterwards, the setup is made ready for the absorption experiments using ammonia + [emim][SCN] solution in one side of the absorber and water on the other side. Absorption experiments are performed with appropriate operating conditions and output values are recorded. The operating conditions under which the experiments are performed, are given as an input to a numerical model. The results obtained by the model are compared with the actual experimental results. By making this comparison, an attempt is made to validate the heat transfer correlations for the absorption process derived by Wang (2019).

(c) Also, these results of the numerical modelling are used to acertain that the empirical correlation governing the convective heat transfer obtained from the water - water experiments can be trusted to yield accurate temperature outputs.

(d) Results obtained by the numerical model are studied in order to get a sound knowledge of the absorption + convective heat transfer process that took place during the experimentation, and to identify the limitations of both the experimental setup and the numerical model. Based on this study, some recommendations are made for the future.

1.4. Approach towards the goal

Figure 1.6 displays all the steps followed during this research, in order to address the research problems. These steps include the literature review, experimental work, numerical analysis, and the validation of the numerical model.

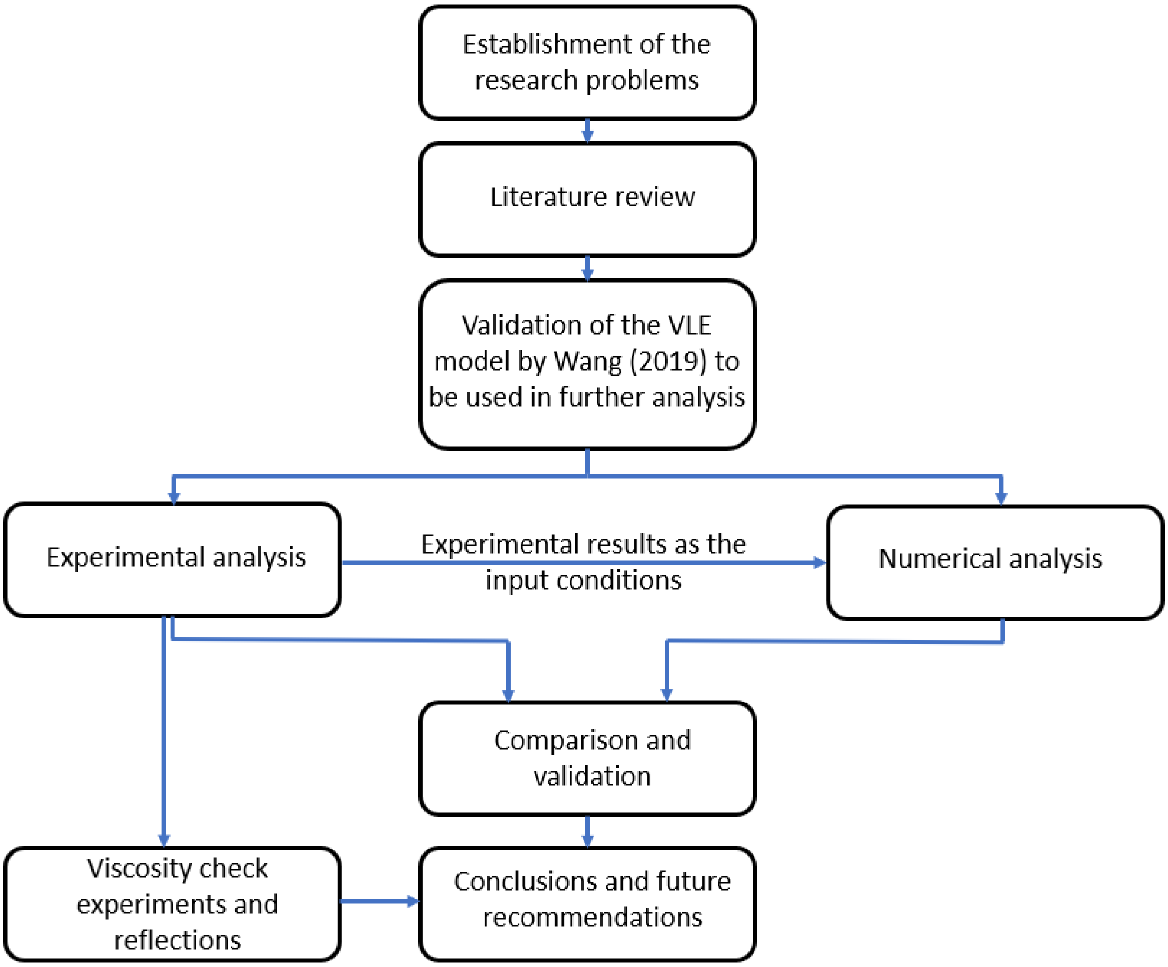

Figure 1.6: Outline of the present research

2

Literature review

Not a lot of literature is available currently to make a perfect choice of the ionic liquid and the refrigerant. However, some works present and compare the transport and thermodynamic properties of different ionic liquids. Similarly, some works are available which analyze the use of such ionic liquids in absorption thermodynamic cycles, both experimentally and numerically. These literature studies help in making an optimum choice of the materials to be used in the cycle.

2.1. Thermodynamic equilibrium

Domańska et al. (2010) determined the phase diagrams of 1-ethyl-3-methylimidazolium thiocyanate ([emim][SCN]) or 1-ethyl-3-methylimidazolium tosylate ([emim][TOS]) + water, or + an alcohol at atmospheric pressure. It was observed that the water showed a complete miscibility with [emim][SCN]. Liquid-liquid and liquid-solid phase equilibria involving the miscibility in the liquid phase region were observed for the systems involving alcohols and [emim][SCN] or [emim][TOS]. NRTL method is used to obtain the *PTx* trend. This paper was referred in the present work to get a better understanding of the thermodynamic equilibrium of the working pairs involving ionic liquids.

Vataščin and Dohnal (2017) studied the thermodynamic behaviour of the aqueous solutions of two ionic liquids - [emim][SCN] and [emim][DCA]. Properties like the conditions for the vapor liquid equilibrium, excess enthalpy, density and viscosity were recorded in the whole range of the composition at different temperatures, and the results are compared. NRTL type of model was used to calculate the equilibrium conditions from the previously available experimental data. Excess volumes and the viscosity of the solution were correlated as functions of the composition and temperatures. It was seen that the aqueous solutions of both the [emim][SCN] and [emim][DCA] exhibit similar behaviour energetically. This paper is referred in the present work to compare the transport properties of pure [emim][SCN] to be used in the calculations.

Wang (2019) considered and analyzed different models to calculate the equilibrium conditions for the vapor liquid equilibrium of different ionic liquids with ammonia vapor. The analysis performed is as follows :

1. Vapor-liquid equilibrium relations for different models are used to predict the performance of the system at desired conditions of temperature. These predicted trends are compared with the results of experimental analysis for the same working pair and in the same conditions. Both these trends are plotted together. The validity of the model is determined using the root mean square deviation (RMSD) of the predicted values from the experimental ones. The most suitable model is the one which has least RMSD.

2. To avoid repeatibility error in the measurement and comparison, experimental data for the same conditions from different sources are considered.

3. Further, enthalpy of mixing is calculated for each of these models in order to analyze heat and mass transfer equations.

PRVdW, PRWS, RK, NRTL and UNIFAC models are considered for a comparison of the predictions of VLE data. Of these, the NRTL model was seen to predict the vapour liquid equilibrium behaviour with least mean deviation from experimental results when a graph of equilibrium pressure versus temperature is plotted. The enthalpy of mixing is found out in this work using three different methods, Equation of State (EOS), Excess Gibb's energy (G^e) method, and Clausius-Clapeyron method. The results obtained using these three methods are compared in his work. A generic RK - EOS model is used to calculate the mixing enthalpy by Wang, 2019, referred from Kim et al. (2012), and Yokozeki and Shiflett (2007).

Yokozeki and Shiflett (2007) measured the solubilities of ammonia in different ionic liquids at room temperature. These ionic liquids include 1-ethyl-3-methylimidazolium acetate, 1-ethyl-3-methylimidazolium thiocyanate, 1-ethyl-3-methylimidazolium ethylsulfate, and N,N-dimethylethanolammonium acetate. Six different mixture compositions of each of the binary systems were taken into account and pressure - temperature - molar composition (*PTx*) data were measured at different temperature conditions. A generic RK model was used to calculate the equilibrium conditions and the plots so obtained were compared with experimental results and negative deviation from the ideal solution behaviour was found. This paper is referred in the present work, in order to check the temperature dependent equations for the thermodynamic properties of the pure ionic liquid.

2.2. Transport properties

Gao and Wagner (2016) proposed a logarithmic relation in order to calculate the viscosity of the solution of ionic liquid + water. According to them, the solution viscosity is a logarithmic function of the individual fluid viscosities.

Valkenburg et al. (2005) encouraged the use of the ionic liquids for heat transfer applications and for the heat storage in power plants with the help of parabolic trough solar collectors, and analyzed the effect of impurities on the thermal and transport properties of ionic liquids. They selected [emim][BF_4], [bmim][BF_4] and [DMPI]Im for the analysis. Thermal properties of the three chosen ionic liquids like the melting point, boiling point, liquidus range, heat of fusion, heat capacity, vapor pressure and thermal conductivity, and other properties like the density, viscosity and chemical compatibility with certain metals are either measured or collected from the literature, and analyzed. They also estimated the effect of various impurities on these properties.

They concluded, that these three ionic liquids have a potential to be used in heat transfer applications, based on their thermal and transport properties, and that in many ways, they are superior to the present heat transfer fluids. They also concluded that the contamination of these ionic liquids by water, metal cations and chlorine has a negative effect on their transport and thermal properties. Also, they identified the high cost and less availability of the ionic liquids as hindrances of their use as commercial heat transfer fluids.

Wang (2019) suggested the use of the logarithmic relation of the solution viscosity (Gao and Wagner, 2016) for the working pair of ammonia - ionic liquid in the absorption process. In this logarithmic relation, the excess viscosity term is neglected, the effect of which was to have a maximum of -90% deviation of the calculated viscosity values from the actual viscosity values. Based on the calculated deviations between the actual values of the viscosity and the logarithmically calculated values of the viscosity, Wang (2019) concluded that this logarithmic approach was a better approach to calculate the solution viscosity as compared to the linear weight average method.

An attempt is made in the present work, to check the validity of this logarithmic relation.

2.3. Heat and mass transfer during the absorption process

Cerezo et al. (2009) studied the absorption process of NH_3 in water in the bubble mode both experimentally and numerically. An iterative control volume method was used to model the bubble absorption process. They noted the effect of the variations of the operation parameters on the absorber thermal load and the mass absorption flux. For this bubble absorption, they report that the numerical results were well in accordance with the experimental ones. They report that the increase in the cooling water flux has a positive effect on the absorption performance, but increase in ammonia concentration in the solution stream, increase in the solution temperature and increase in the coolant temperature affected the absorption performance negatively.

Kang et al. (2000) analyzed the combined heat and mass transfer for an ammonia- water absorption process for two different absorption modes - falling film absorption and bubble absorption, using a plate heat exchanger. Their work concludes that the local coefficient of absorption was always larger in the bubble mode as compared in the falling film mode, the result of which was the fact the overall effective heat transfer area of the exchanger was much smaller (about 48 %) for the bubble absorption mode. Concentration and temperature profiles are plotted for both the modes throughout the length of the absorber for a general counter current absorption, wherein the solution and the vapor flow in one direction and water flows in the opposite direction. These overall temperature and concentration distributions are shown in figure 2.1. It can be seen generally that temperature of bulk liquid is a bit lower than that of the interface. This suggests heat transfer resistance at the liquid side is low. Also, the concentration in the bulk liquid is reasonably lower than that at the interface, which suggests that the mass transfer resistance is considerable at the liquid side. So, these two facts lead to the conclusion that the resistance to the mass transfer is dominant on the liquid side.

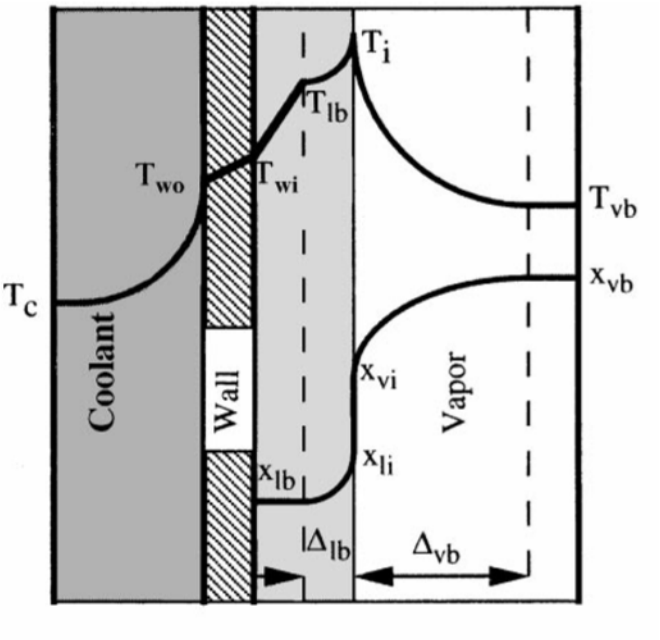

Figure 2.1: Temperature and concentration profiles for the absorption process (Kang et al., 2000).

At the vapor side, the heat transfer resistance is considerable, as the bulk vapor temperature increases a fair amount from the bottom of the absorber. There is also a substantial concentration difference in the concentration at the bulk vapour side, which indicates a considerable mass transfer resistance. Some aspects of the temperature distributions vary for the falling film mode and the bubble mode. Graphs of both these modes are shown in figures 2.2 ans 2.3 respectively.

In figures 2.2 and 2.3, the lines representing the interface temperature (T_i) and the liquid bulk temperature (T_{lb}) seem to be very close together (overlapped in the falling film absorption, figure 2.2) thus indicating negligible heat transfer resistance between the interface and the bulk liquid, as compared to the heat transfer resistance from the bulk liquid to the wall. It should be noted here that the interface temperature (T_i) is the equilibrium temperature at a particular concentration and pressure. Temperature curves for the falling film mode (figure 2.2) corroborate the general assumption made from the overall temperature and concentration distributions (figure 2.1), that only the mass transfer resistance is considerable at the liquid side, whereas both heat and mass transfer resistances are considerable at the vapor side.

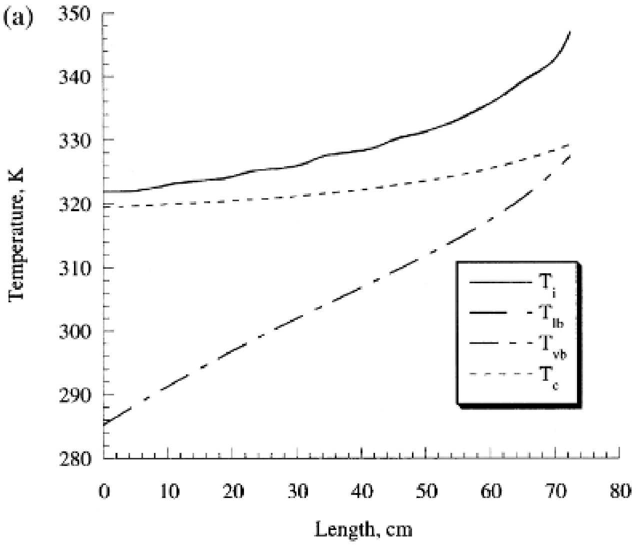

Figure 2.2: Temperature distribution for falling film absorption (Kang et al., 2000), Wherein T_i = Interface temperature; T_{lb} = Liquid bulk temperature; T_{vb} = Vapor bulk temperature; T_c = Coolant temperature

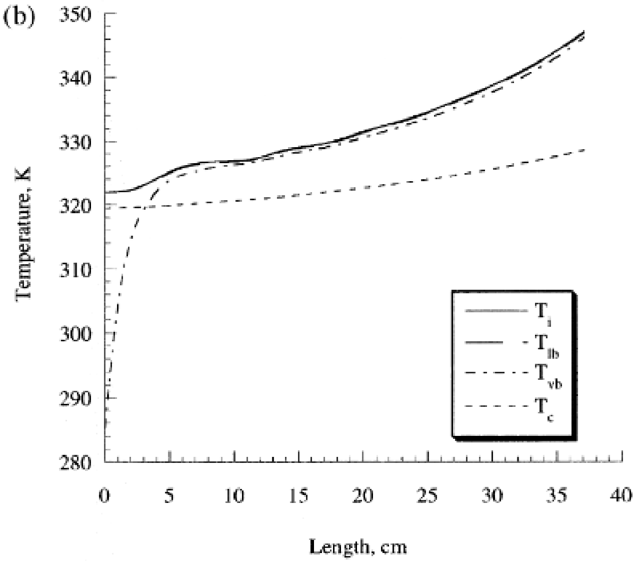

Figure 2.3: Temperature distribution for bubble absorption (Kang et al., 2000), Wherein T_i = Interface temperature; T_{lb} = Liquid bulk temperature; T_{vb} = Vapor bulk temperature; T_c = Coolant temperature

It can be seen from figure 2.3 that in the bubble absorption mode, the temperature of the vapor increases rapidly until it reaches the interface temperature. Thus, in the bubble mode, the resistance to the heat transfer from the interface to the vapor is considerable near the bottom of the absorber, till the vapor temperature stabilizes near the interface temperature. The difference in the temperature profiles of the vapor in the falling film and the bubble absorption can be because of the fact that in the bubble mode, the vapor and the solution are well mixed with each other, thus the vapor temperature rises rapidly and then stabilizes near the interface temperature. On the other hand, in the falling film mode, the vapor and the solution are not mixed as well with each other, thus exhibiting significantly higher heat transfer resistance to the vapor side than that in the bubble absorption. So, the vapor temperature remains well below the interface temperature. Also, the difference in the vapor profiles can be due to the fundamental differences between the geometry of a bubble and that of a film. They also concluded that the vapor phase flow rate was the dominant parameter for heat transfer, and the solution flow rate was the dominant parameter for the mass transfer during the absorption.

Khan et al. (2010) experimentally studied the effect of the geometry of heat exchanger on the Nusselt number, and effectively, on the heat transfer coefficient. They conducted water-water experiments in a corrugated cross flow plate heat exchanger for different plate geometries (Chevron angle, corrugation depth) and developed a Nusselt-Reynolds-Prandtl relation for equal Reynolds number on either side of the exchanger. They also validated these results with the help of the previously published literature on the topic.

Wang et al. (2019) studied absorption of ammonia in NH_3 + IL solution. Experimental data are used to find out the unknown parameters in the transfer equations and a numerical model is constructed to solve heat and mass transfer equations to find the outlet properties.

Wang (2019) modelled numerically the heat and mass transfer during absorption of ammonia in ammonia + $LiNO_3$ solution. A detailed numerical procedure is performed to calculate the overall heat transfer coefficient of the absorption cycle for ammonia as a refrigerant, and the fluid $NH_3 - LiNO_3$ as the absorbent fluid. A semi- empirical model is developed in Matlab for the absorption process. It uses several of the already established theories regarding heat and mass transfer, including the void fraction theory, two resistance theory and Chilton- Colburn analogy. It also uses heat and mass transfer equations to establish the balance. The outline of this work performed by Wang (2019) is shown in figure 2.4.

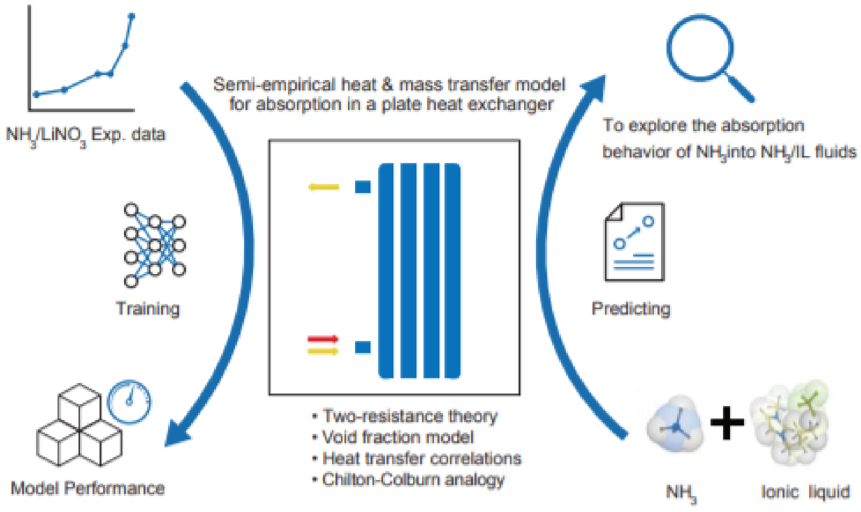

Figure 2.4: Outline of Wang's (2019) approach to develop a numerical model for the absorption process

Absorption takes place in a plate heat exchanger where the heat due to the absorption is taken by the circulation of cooling water. The efficiency of this cycle is calculated in terms of the heat transfer coefficient. This absorption model is displayed in figure 2.5.

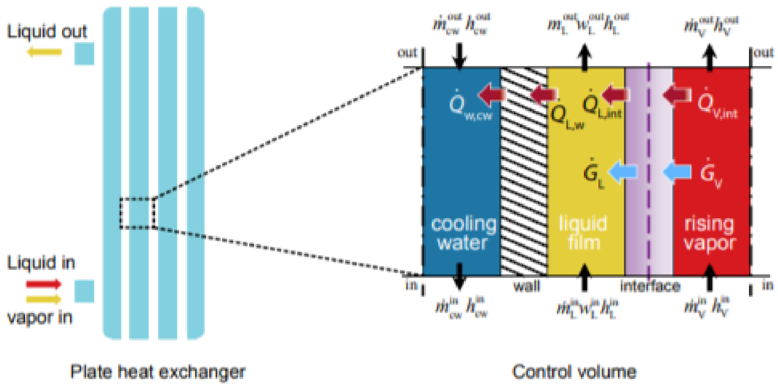

Plate heat exchanger

Control volume

Figure 2.5: Theoretical absorption model with a detail of a single control volume (Wang, 2019)

The blue stream in figure 2.5 represents the stream of cooling water going from the top to the bottom of the heat exchanger. Adjacent to it, is the wall of the plate heat exchanger. The layer adjacent to the wall displayed in yellow colour represents the absorbent solution going from bottom to the top of the heat exchanger. Layer adjacent to it is the interface between solution and the ammonia vapor. The last layer displayed in the red colour is the bulk vapor stream, also going from the bottom to the top. It is through this interface that the absorption of ammonia vapor into the bulk absorbent solution takes place.

Following assumptions are made in order to analyze the cycle.

1. The system operates in a steady state.
2. Thermal losses are neglected for the ease of calculation.
3. Thin film assumption is made at the interface. The liquid film is thin and symmetrical with the plates.
4. Interface is at equilibrium.
5. Thermal boundary layers between the single phase and two phase regions show a smooth transition.
6. Transverse and longitudinal heat conduction at the plates of heat exchanger is neglected.
7. A uniform distribution is assumed along the width of the plate.
8. Absorbents are considered non volatile, so there is no absorbent in the vapor phase.

The volume of the heat exchanger is discretized in small control volumes. Available input conditions are given to the control volume at the bottom, assuming that the cooling water enters from the top and the solution enters from the bottom. Further, vapour liquid equilibrium is established in the control volume, and the equilibrium conditions are calculated at a particular temperature and mass concentration ratio of ammonia in the absorbent solution. These conditions are used to calculate the enthalpy of the solution. This enthalpy is used to establish the heat and mass transfer balance in the control volume, thereby calculating the outlet conditions of the control volume. These outputs are given as inputs to the next control volume and the procedure is repeated. Finally, the end pressure and temperature conditions are calculated for the last control volume at the top of the absorber. A more detailed explanation and some crucial technical details of this numerical modelling are presented in chapter 6 of the present work, as this numerical model is used as a basis to develop the model used in the present work.

The end results are then used to calculate the heat transfer coefficient, and thus the performance of the system and that of the ionic liquid are evaluated. Empirical correlations of Nusselt-Prandtl-Reynolds, that govern the absorption heat transfer, have been derived by Wang (2019) using the experimental data by Amaris Castilla (2014). From this analysis, it was observed that the use of [emim][SCN] as an absorbent does not show the highest overall heat transfer coefficient. However, it still shows higher overall heat transfer coefficient than the reference pair.

Block diagram of this process is shown in figure 2.6.

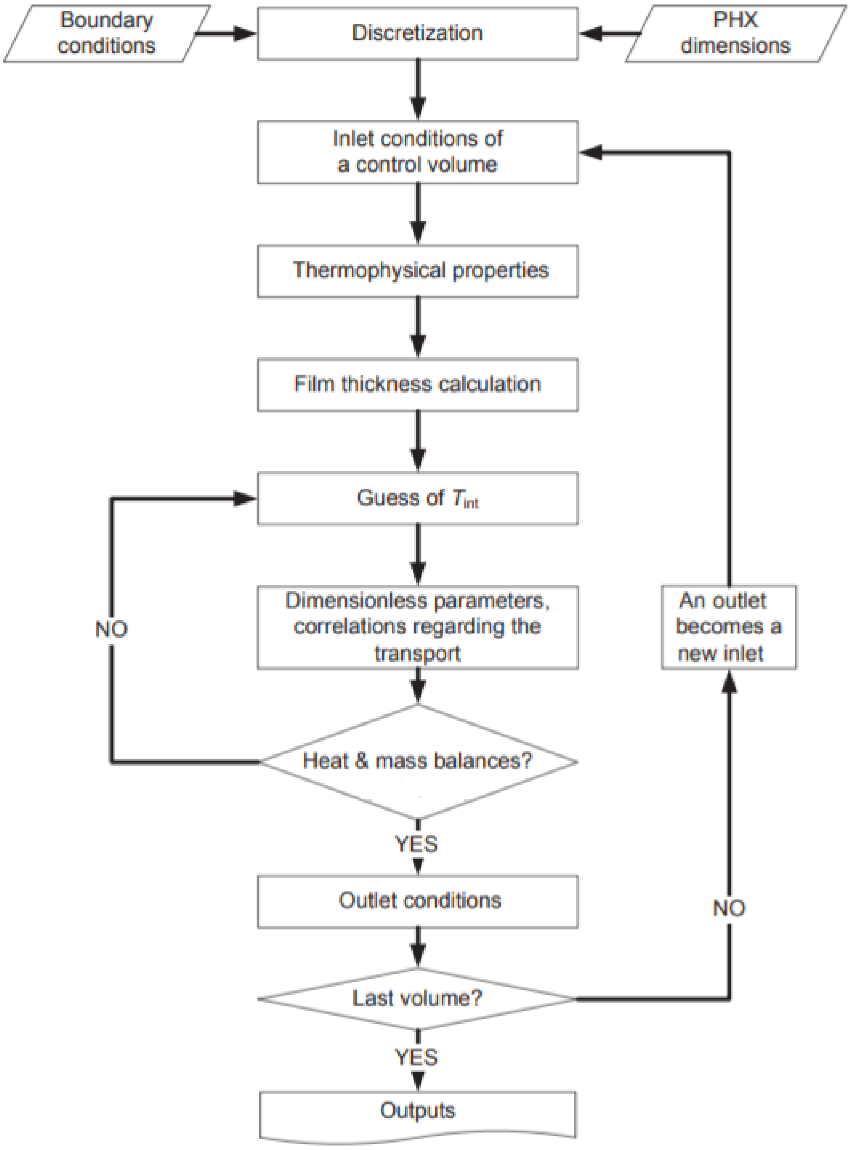

Figure 2.6: Block diagram for the numerical process used by Wang (2019)

2.4. Analytical and numerical studies regarding the absorption cycle performance

Amaris Castilla (2014) reported experimental data for an absorption heat pump cycle for the working pair of ammonia- $LiNO_3$. This data has been numerically analyzed by Wang (2019) in a numerical heat and mass transfer model to predict the performance of the absorption cycle. Using the experimental data by Amaris Castilla (2014), Wang (2019) validated his numerical model for the absorption process.

Triché et al. (2017) made a comparison of results of the numerical analysis of the falling film absorber with the results of experimentation, using ammonia-water as the working pair. Maximum of 15% deviation was found when the comparison was made. They defined the mass effectiveness as the ratio of the actual absorbed mass flow rate in the absorption process, to the maximum vapor mass flow rate that can be absorbed for an infinite counter flow absorber. The comparison between the numerical and experimental results for mass effectiveness, absorbed mass flow rate and the heat rate (the rate of the heat exchanged) is shown in figures 2.7, 2.8 and 2.9 respectively.

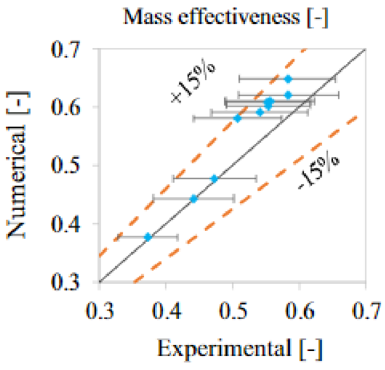

Figure 2.7: Comparison between numerical and experimental results for mass effectiveness (Triché et al., 2017)

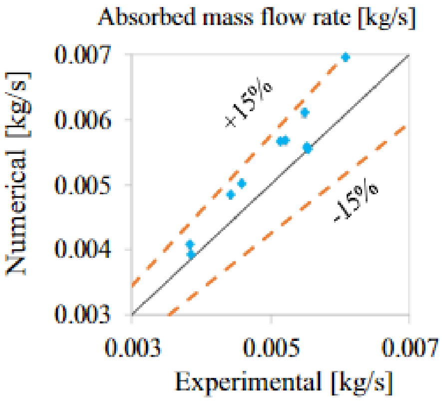

Figure 2.8: Comparison between numerical and experimental results for absorbed mass flow rate (Triché et al., 2017)

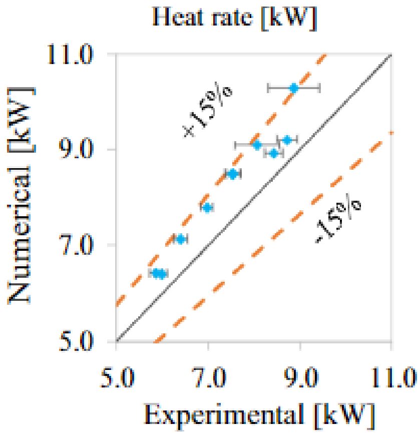

Figure 2.9: Comparison between numerical and experimental results for heat rate (Triché et al., 2017)

They particularly studied the effect of variation in the coolant mass flow rate on various parameters. They concluded that in an absorption process like this, the mass transfer resistance is dominant for the falling film mode at the liquid side as the heat transfer resistance at the liquid side is almost negligible. It was also found that the mass effectiveness is directly proportional to the coolant mass flow rate. The overall low mass effectiveness calculated during this analysis, can be linked to the fact that water evaporates in some amounts along with ammonia. Thus there is water vapor left in some fraction in the ammonia vapour, thus reducing the overall mass effectiveness of the absorption process.

Wang and Infante Ferreira (2017) studied the performance of nine NH_3 - IL pairs and compared these pairs in terms of their applications in the single effect heat pump absorption cycle.

Coefficients of performance (COP) for these pairs were also calculated and it was seen that COP of NH_3-[mmim][DMP] pair was highest. Coefficients of performance of these pairs were compared with that of ammonia-water pair and it was found that quite a lot of them had higher coefficient of performance than that of the ammonia- water pair. Also, a model of an optimized NH_3 - IL pair was developed with highest optimized COP.

Wang (2019) compared different ionic liquids based on different criteria, including the coefficient of performance of the absorption cycle, and the circulation ratio achieved when that particular fluid is used along with ammonia. Also, the performances of different pairs containing different ionic liquids are compared with that of ammonia- water pair, calculated using the same method. Simple refrigeration and absorption cycle calculations are used to calculate these parameters. These calculations are made at T_{con} /T_{abs} / T_{eva} = 45/45/10 ° C. From the analysis, it is seen that NH_3-[mmim][DMP] has the highest COP for the absorption cycle (1.79). Also, NH_3-[bmim][BF_4], NH_3-[emim][Tf_2N], and NH_3-[emim][SCN] all show COP higher than that of NH_3-H_2O pair. This analysis is shown in figure 2.10.

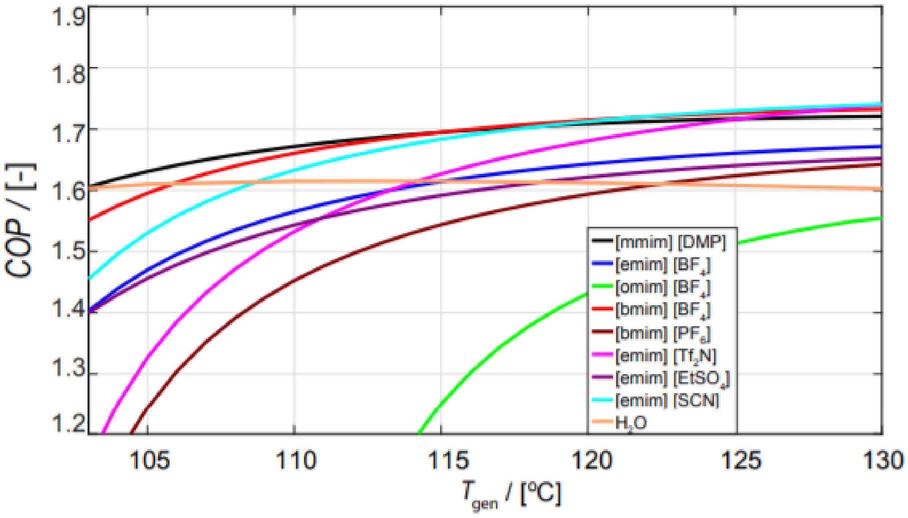

Figure 2.10: Comparison of COPs of different ionic liquid pairs (Wang, 2019)

For the functioning of the cycle, it is clear that lower the circulation ratio, the higher will be the COP of the cycle. Different ionic liquid pairs are also compared on the basis of the circulation ratio. Same operating conditions as those used in the analysis of COP are used for calculating the circulation ratio. This comparison is shown in figure 2.11.

All this literature was helpful to make an educated choice of the ionic liquid that has been used in this research. All the previously recorded readings were guidelines in understanding the trend of the absorption cycle and it gave the knowledge of what to expect in the actual experimentation. Wang (2019), decided to use [emim][SCN] as absorbent in his setup at the Delft University of Technology. The experiments are carried out on this setup as a part of the present work. Same choice of the ionic liquid, [emim][SCN], is made for these experiments based on the availability, economic factors, and the performance enhancement.

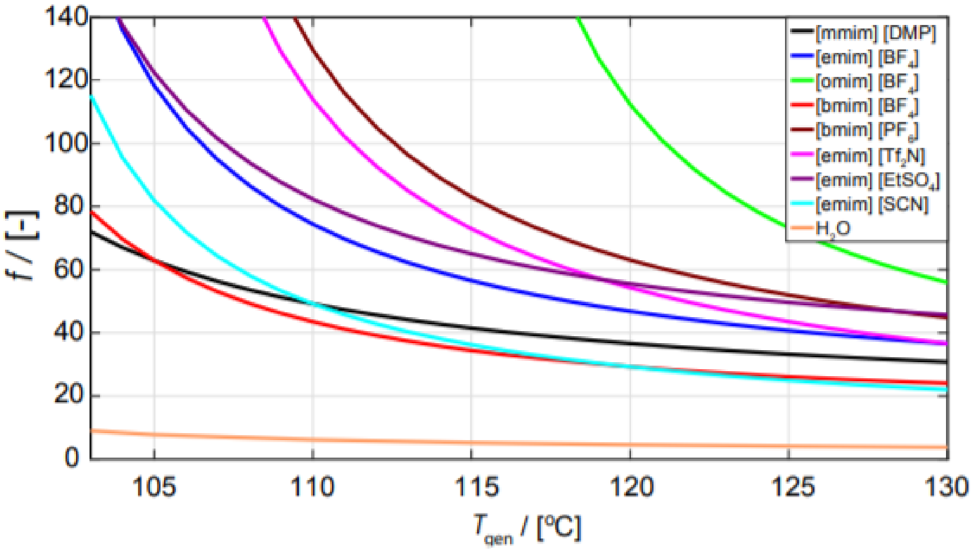

Figure 2.11: Comparison of circulation ratios of different ionic liquid pairs (Wang, 2019)

3

Thermodynamic and transport properties of the selected working pair

Based on the literature survey, the estimated heat transfer coefficients, the absorption cycle performance, the economic factors, and the availability of the ionic liquids, NH_3-[emim][SCN] is selected as the working pair for the absorption system in the present work.

It is of crucial importance to use the accurate values for the physical, transport and thermodynamic properties of the selected working pair in the analysis of the data obtained, in order to yield the results within an acceptable range of accuracy. The sources and the method of calculation of various properties of the selected working pair that are used in this work, are presented in this chapter.

3.1. Properties of the pure fluids

3.1.1. Ammonia

For the analysis of the experimental data, the thermodynamic and physical properties of ammonia at the saturated conditions are obtained from Refprop (Lemmon et al., 2010) at particular state points.

3.1.2. [emim][SCN]

Physical and chemical information of the selected ionic liquid ([emim][SCN]) is displayed in table 3.1.

Table 3.1: Details of [emim][SCN] (Yokozeki and Shiflett, 2007, Wang,2019)

[emim][SCN]]	
IUPAC name	1-ethyl-3-methylimidazoliumthiocyanate
Chemical formula	$C_7H_{11}N_3S$
CAS Number	331717-63-3

As for the ionic liquid [emim][SCN], the temperature dependent equations proposed by Wang (2019) were used for the numerical and experimental analysis in the present work. He referred to various papers from the literature to check these equations for the transport properties of pure [emim][SCN] as a function of temperature. The equations used for the thermodynamic and transport properties for pure [emim][SCN] are displayed in table 3.2. The literature from which the properties of pure [emim][SCN] are studied for the present work are listed in the rightmost column of table 3.2.

It should be noted here, that the equation for the density from table 3.2 applies to pure [emim][SCN], without any impurities. If [emim][SCN] to be used contains any amount of impurities, there may be a need to check the validity of this equation (described in chapter 7).

Wang (2019) correlated the experimental data of the viscosities and the thermal conductivities of pure [emim][SCN], [bmim][BF_4] and [emim][Tf_2N], to obtain the trends with a change in their temperatures.

Table 3.2: Thermodynamic and transport properties of pure [emim][SCN] as a function of the solution temperature (Wang, 2019)

	[emim][SCN]]	References
$M_{w,\mathrm{IL}}$	169.25	-
$c_{p\mathrm{IL}}$ (KJ/kg-K)	$c_{p\mathrm{IL}} = 0.6882 + 0.0032T$	-
λ_{IL} (W/m-K)	0.21	Tenney et al. (2014) Valkenburg et al. (2005) Fröba et al. (2010)
μ_{IL} (Pa-s)	$\ln \mu_{\mathrm{IL}} = -7.839 + \frac{486}{T-179.6}$	Salgado et al. (2014) Hofmann et al. (2015) Ficke et al. (2010) Paulechka et al. (2010)
ρ_{IL} (kg/m^3)	$\rho_{\mathrm{IL}} = 1296 - 0.602T$	Ficke et al. (2010)
σ_{IL} (N/m)	$\sigma_{\mathrm{IL}} = 7.926 * 10^{-}2 - 8.709 * 10^{-}5T$	Almeida et al. (2012)

* T in K

Viscosity

High viscosity of the ionic liquids can be considered their limitation, which might prevent the ionic liquids to be used in heat transfer applications. The trend obtained by Wang (2019) by correlating the experimental data for the viscosity values of [emim][SCN] is shown in figure 3.1 with a line of the **cyan** color.

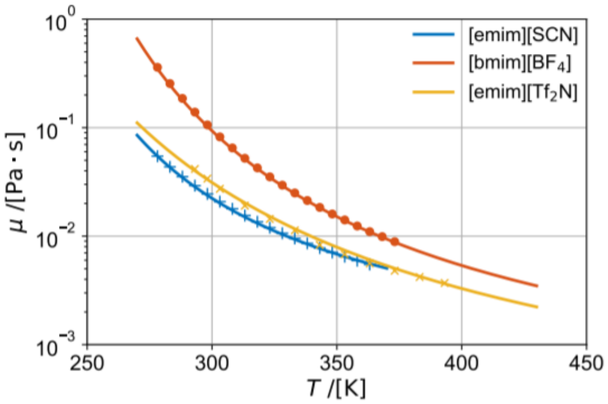

Figure 3.1: Viscosity as a function of temperature for pure [emim][SCN], [bmim][BF$_4$] and [emim][Tf$_2$N] (Wang, 2019) (Wang, 2019)

Thermal conductivity

Similar to the case for the viscosity, the trend obtained by Wang (2019) for the change in thermal conductivity of pure [emim][SCN] with temperature is shown in figure 3.2 with a line of the **cyan** color.

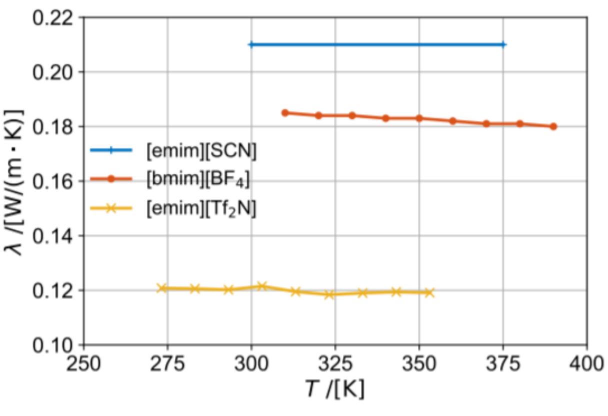

Figure 3.2: Thermal conductivity as a function of temperature for pure [emim][SCN], [bmim][BF$_4$] and [emim][Tf$_2$N] (Wang, 2019)

3.2. Properties of the solution

3.2.1. Density

Density of the solution of NH_3+[emim][SCN] is calculated using the density of pure [emim][SCN] and that of pure ammonia at a particular temperature and pressure (operating conditions), based on a linear weight average method.

$$\rho_{\mathrm{sol}} = w_{\mathrm{IL}}\rho_{\mathrm{IL}} + w_{\mathrm{NH_3}}\rho_{\mathrm{NH_3}} \tag{3.1}$$

It is observed that addition of ammonia to [emim][SCN] reduces its density.

3.2.2. Thermal conductivity

Equation for the thermal conductivity of the solution (NH_3+[emim][SCN]) is the same one used by Wang (2019). As expected, this relation shows a linear trend, as the thermal conductivity of the solution is calculated using the linear weight average method.

$$\lambda_{\mathrm{sol}} = w_{\mathrm{IL}}\lambda_{\mathrm{IL}} + w_{\mathrm{NH_3}}\lambda_{\mathrm{NH_3}} \tag{3.2}$$

3.2.3. Specific heat capacity

Similar to that of the thermal conductivity, the equation for the specific heat capacity of the solution (NH_3+[emim][SCN]) is the same one used by Wang (2019).

$$C_{p_{\mathrm{sol}}} = w_{\mathrm{IL}}C_{p_{\mathrm{IL}}} + w_{\mathrm{NH_3}}C_{p_{\mathrm{NH_3}}} \tag{3.3}$$

3.2.4. Viscosity

Viscosity of the solution is calculated based on the mole fraction and not the mass fraction like the other properties. Also, unlike other properties of the solution, there exists a logarithmic relation between the viscosity of the solution and the viscosities of the pure substances (Gao and Wagner, 2016, Wang, 2019).

$$ln\mu_{\mathrm{sol}} = x_{\mathrm{IL}}ln\mu_{\mathrm{IL}} + x_{\mathrm{NH_3}}ln\mu_{\mathrm{NH_3}} \tag{3.4}$$

The validity of this relation for this particular solution of (NH_3+[emim][SCN]) is tested in this work with the experimental observations.

A separate set of experiments was performed for the convective heat transfer between ammonia +[emim][SCN] solution and water. The process followed to perform these experiments and the results obtained are explained in the upcoming chapters. As in case of the density of the solution, it is observed that the viscosity of [emim][SCN] reduces with the addition of ammonia to it (Cera-Manjarres, 2015).

3.2.5. Surface tension

Like for thermal conductivity, the surface tension of the solution is obtained based on the weight average of the two individual fluids. As in case of the density, thermal conductivity and the specific heat capacity, this relation shows a linear trend.

$$\sigma_{\mathrm{sol}} = w_{\mathrm{IL}}\sigma_{\mathrm{IL}} + w_{\mathrm{NH_3}}\sigma_{\mathrm{NH_3}} \tag{3.5}$$

3.2.6. Mass diffusivity

Considering the fact that [emim][SCN] is a newly put-forth fluid for the absorption cycles, the relation for the mass diffusivity of ammonia in it remains unknown. However, the relation of it with the viscosity can be used in order to make a rough estimation. In the work of Wang (2019), the relation developed from the theory of the Stokes- Einstein equation, is used to calculate the mass diffusivity. This correlation permits the calculation of the mass diffusivity of ammonia (solute) based on simple property like the viscosity of the ionic liquid (solvent). This equation is displayed in equation 3.6, for solvents A and B.

$$D_{\mathrm{NH_3,IL,B}} = (\frac{\mu_{\mathrm{IL,B}}}{\mu_{\mathrm{IL,A}}})^{-1.45}D_{\mathrm{NH_3,IL,A}} \tag{3.6}$$

Since the mass diffusivities of ammonia into other ionic liquids are more or less known, equation 3.6 can be used to determine the mass diffusivity of ammonia into [emim][SCN] (Bedia et al., 2012, Wang, 2019).

Thermo-physical properties of pure [emim][SCN] are used during the calculation of the thermo-physical properties of the solution. As displayed in table 3.2, the properties of pure [emim][SCN] are calculated taking into the consideration the dependence on the operating temperature.

3.3. Vapour-liquid equilibrium

A vapour-liquid equilibrium model was developed by Wang (2019) for the estimation of the thermal properties during absorption.

3.3.1. Construction of the VLE

Non random two - liquids (NRTL) model was used in order to describe the relationship between the thermodynamic parameters - *PTw*, for the ammonia - [emim][SCN] working pair. The equations for the VLE are described below and the values of the NRTL parameters used are stated.

In the case of ammonia + [emim][SCN] working pair, owing to the negligible vapor pressure of the ionic liquid, it is assumed that there is no [emim][SCN] in the vapor stream. Following simplified equilibrium criterion is used to calculate the equilibrium pressure.

$$P = \gamma_{\mathrm{NH_3}} x_{\mathrm{NH_3}} P_{\mathrm{NH_3}}^{\mathrm{Sat}} \tag{3.7}$$

Where, the activity coefficient of NH_3 is calculated using the NRTL model, as per equation 3.8.

$$ln\gamma_{\mathrm{NH_3}} = x_2^2 \tau_{21} (\frac{G_{21}}{x_1 + x_2 G_{21}})^2 + \frac{G_{12}\tau_{12}}{(x_2 + x_1 G_{12})^2} \tag{3.8}$$

Where,

$$G_{12} = exp(-\alpha\tau_{12}) \tag{3.9}$$

$$G_{21} = exp(-\alpha\tau_{21}) \tag{3.10}$$

$$\tau_{12} = \tau_{12}^0 + \frac{\tau_{12}^1}{T} \tag{3.11}$$

$$\tau_{21} = \tau_{21}^0 + \frac{\tau_{21}^1}{T} \tag{3.12}$$

Where, the components of the solution are denoted as component 1 and component 2, and the equilibrium temperature is denoted as *T*.

The NRTL coefficients used by Wang (2019) to construct the VLE are shown in table 3.3 (referred from figure 30, Appendix A).

Table 3.3: Values of the NRTL used for the working pair of ammonia - [emim][SCN] (Wang, 2019)

NH_3 + [emim][SCN]]			NRTL parameters	
α	τ_{12}^0	τ_{12}^1	τ_{21}^0	τ_{21}^1
-0.27082	-10.66	3120.01	5.6	-1967.71

Critical conditions for [emim][SCN] and it's molecular weight is taken from figure 29, Appendix A (Wang, 2019).

3.3.2. Validation of the VLE model

The VLE model developed by Wang (2019) (see figures 25 and 26, Appendix A) is compared with the previously published experimental data by Yokozeki and Shiflett (2007) (see figure 31, Appendix A), and its further use in the numerical model of the absorption model is justified. It is important to note here, that the VLE model by Wang (2019) is derived using those values of the NRTL coefficients that are displayed in table 3.3.

A set of experimental data for the ammonia + [emim][SCN] working pair reported by Yokozeki and Shiflett (2007), is used for the validation. These data are shown in table 3.4.

Procedure for the validation

The concentrations and the temperatures for each of the six data sets are used to calculate the equilibrium pressure using the VLE model developed by Wang (2019). These obtained pressures are plotted along with the temperature and the concentrations in a Pressure- Temperature-Concentration (*PTw*) plot, where *w* is the mass concentration of ammonia in the solution. Further, pressures measured in each of the data sets for each condition, along with the operating temperatures are plotted in these figures using markers. The distance of each of these markers for the particular equilibrium concentration saturation line represents the deviation of the VLE model in question from the model established by Wang (2019).

Table 3.4: Experimental data for the Vapor Liquid Equilibrium (Yokozeki and Shiflett, 2007)

$NH_3(1)$ + [emim][SCN](2)		
T (K)	*P* (MPa)	100 x_1 (mol)
283.2	0.244	45.1 % ± 0.7 %
283.2	0.364	65.2 % ± 0.5 %
283.2	0.447	73.1 % ± 0.4 %
283.2	0.502	78.6 % ± 0.2 %
283.2	0.547	81.9 % ± 0.2 %
283.2	0.590	87.6 % ± 0.1 %
298.1	0.307	44.4 % ± 0.9 %
298.1	0.536	64.2 % ± 0.7 %
298.1	0.672	72.3 % ± 0.5 %
298.1	0.747	78.1 % ± 0.4 %
298.1	0.815	81.5 % ± 0.3 %
298.1	0.911	87.4 % ± 0.1 %
322.6	0.535	41.6 % ± 1.6 %
322.6	0.961	61.8 % ± 1.4 %
322.6	1.241	70.4 % ± 1.1 %
322.6	1.420	76.6 % ± 0.8 %
322.6	1.562	80.4 % ± 0.6 %
322.6	1.777	86.9 % ± 0.3 %
348.0	0.840	37.8 % ± 2.7 %
348.0	1.553	58.1 % ± 2.6 %
348.0	2.045	67.3 % ± 2.2 %
348.0	2.419	74.1 % ± 1.7 %
348.0	2.711	78.4 % ± 1.4 %
348.0	3.774	85.8 % ± 0.8 %
372.8	1.149	34.0 % ± 4.4 %
372.8	2.144	54.2 % ± 4.1 %
372.8	2.958	63.3 % ± 3.5 %
372.8	3.576	70.8 % ± 3.2 %
372.8	4.120	75.4 % ± 2.8 %
372.8	5.007	83.9 % ± 1.7 %
298.1	0.314	44.3 % ± 0.9 %
298.1	0.540	64.2 % ± 0.7 %
298.1	0.666	72.4 % ± 0.5 %
298.1	0.772	78.0 % ± 0.4 %
298.1	0.831	81.5 % ± 0.3 %
298.1	0.930	87.4 % ± 0.1 %

Six separate plots were made for each of the six data sets from table 3.4. These plots are displayed in figures 3.3 to 3.8.

Figure 3.3 shows the plot made to correlate the data from data set 1 in table 3.4.

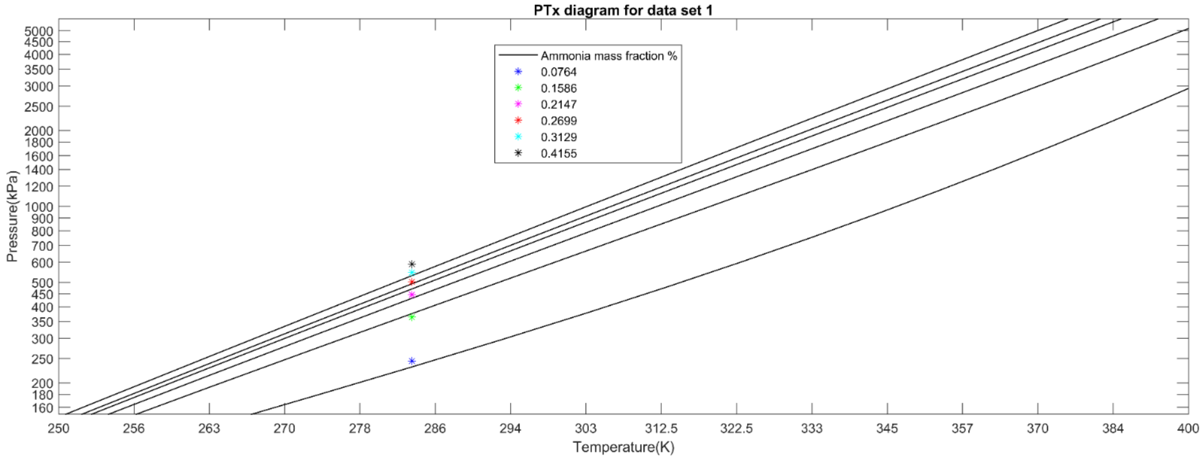

Figure 3.3: *PTw* plot for data set 1 (Temperature = 283.2 K)

Figure 3.4 shows the plot made to correlate the data from data set 2 in table 3.4.

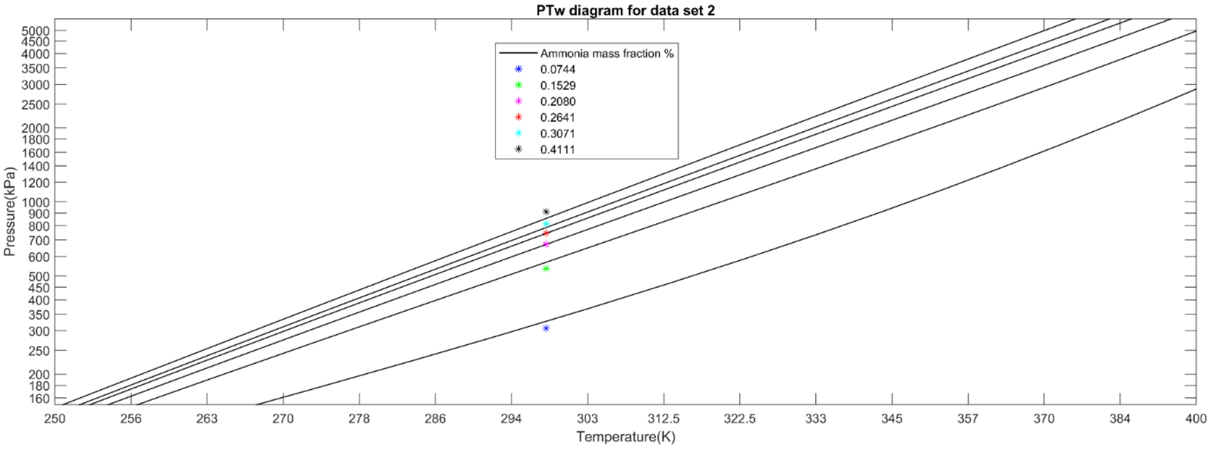

Figure 3.4: *PTw* plot for data set 2 (Temperature = 298.1 K)

Figure 3.5 shows the plot made to correlate the data from data set 3 in table 3.4.

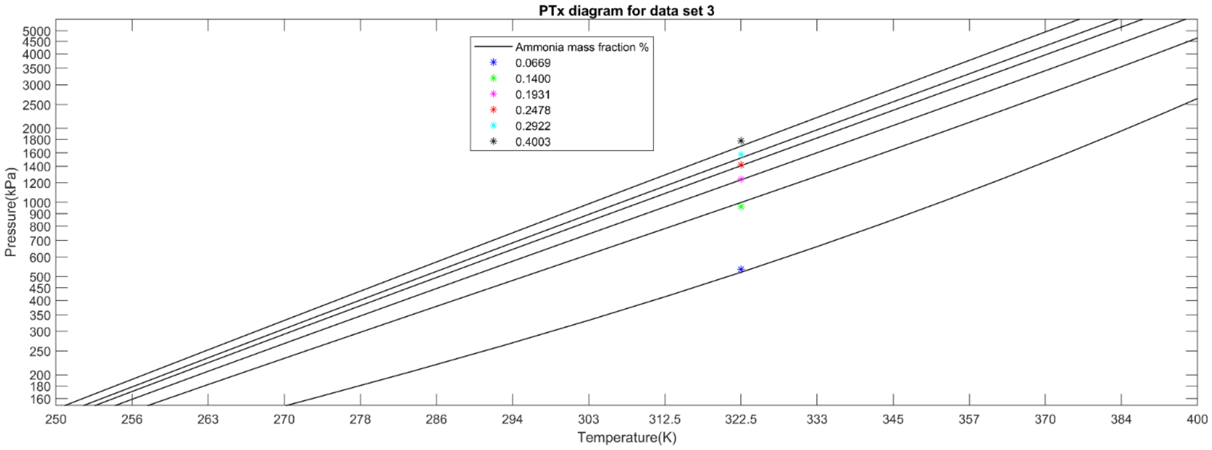

Figure 3.5: *PTw* plot for data set 3 (Temperature = 322.6 K)

Figure 3.6 shows the plot made to correlate the data from data set 4 in table 3.4.

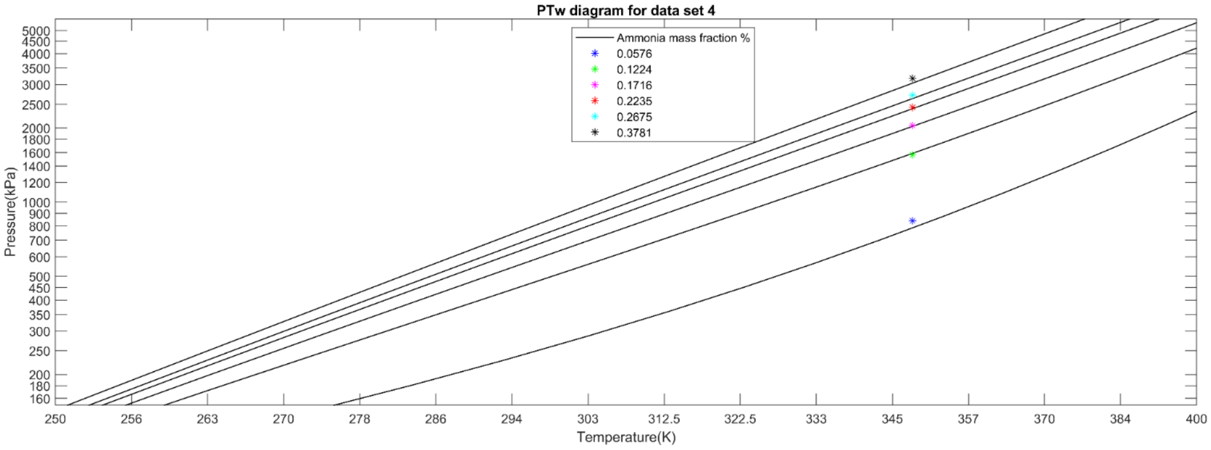

Figure 3.6: *PTw* plot for data set 4 (Temperature = 348 K)

Figure 3.7 shows the plot made to correlate the data from data set 5 in table 3.4.

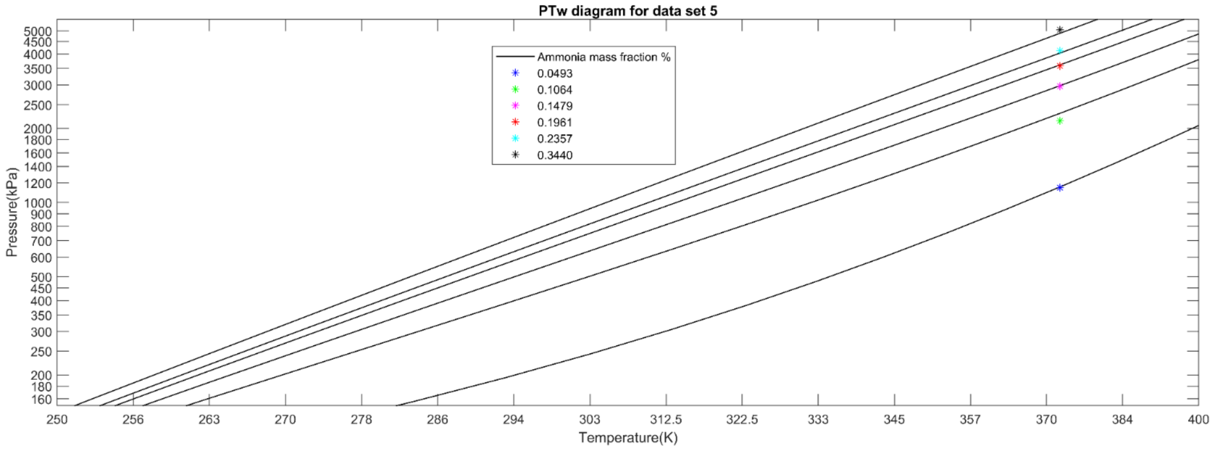

Figure 3.7: *PTw* plot for data set 5 (Temperature = 372.8 K)

Figure 3.8 shows the plot made to correlate the data from data set 6 in table 3.4.

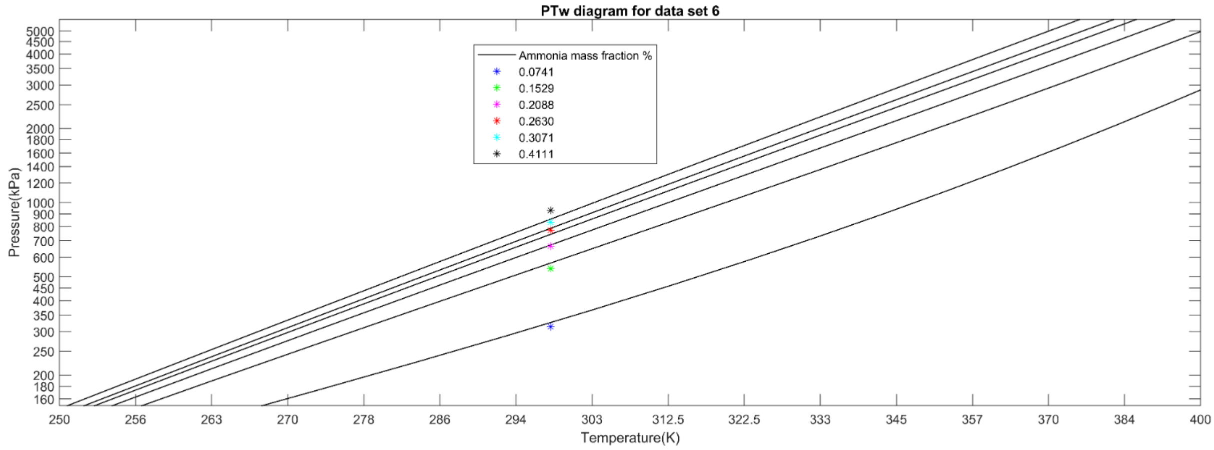

Figure 3.8: *PTw* plot for data set 6 (Temperature = 298.1 K)

The pressure sensor that was used in the experiments had an accuracy of ±5 % of the full scale (0-7 MPa) (Yokozeki and Shiflett, 2007).

It should be noted that, the value of concentrations of the equilibrium lines and the markers are shown in the legend box in each diagram in the same color as that of each of the markers in the diagram. Pressures measured experimentally by Yokozeki and Shiflett (2007) differ from the ones calculated from the VLE model of Wang (2019) by a small amount. Still, it can be seen from the plots of the six data sets, that the vapor - liquid equilibrium model developed by Wang (2019) matches reasonably with the experimental data by Yokozeki and Shiflett (2007) with an acceptable deviation. Since the vapor liquid equilibrium was established using the NRTL model (Wang, 2019), it is validated that the NRTL coefficients used in this VLE model for the working pair of ammonia - [emim][SCN] (table 3.3), work well for calculating the thermodynamic equilibrium at the vapor - liquid interface in the absorption process.

This validation of the VLE model by Wang (2019) justifies its further use in the numerical modelling of the absorption process in the present work.

4

Experimental analysis

4.1. Experimental setup

An absorption system is designed in the lab of TU Delft Process and Energy. The whole heat pump cycle is not studied experimentally, instead just the absorption process is studied. The picture and a schematic sketch of the experimental setup are displayed in figure 4.1 and 4.2 respectively.

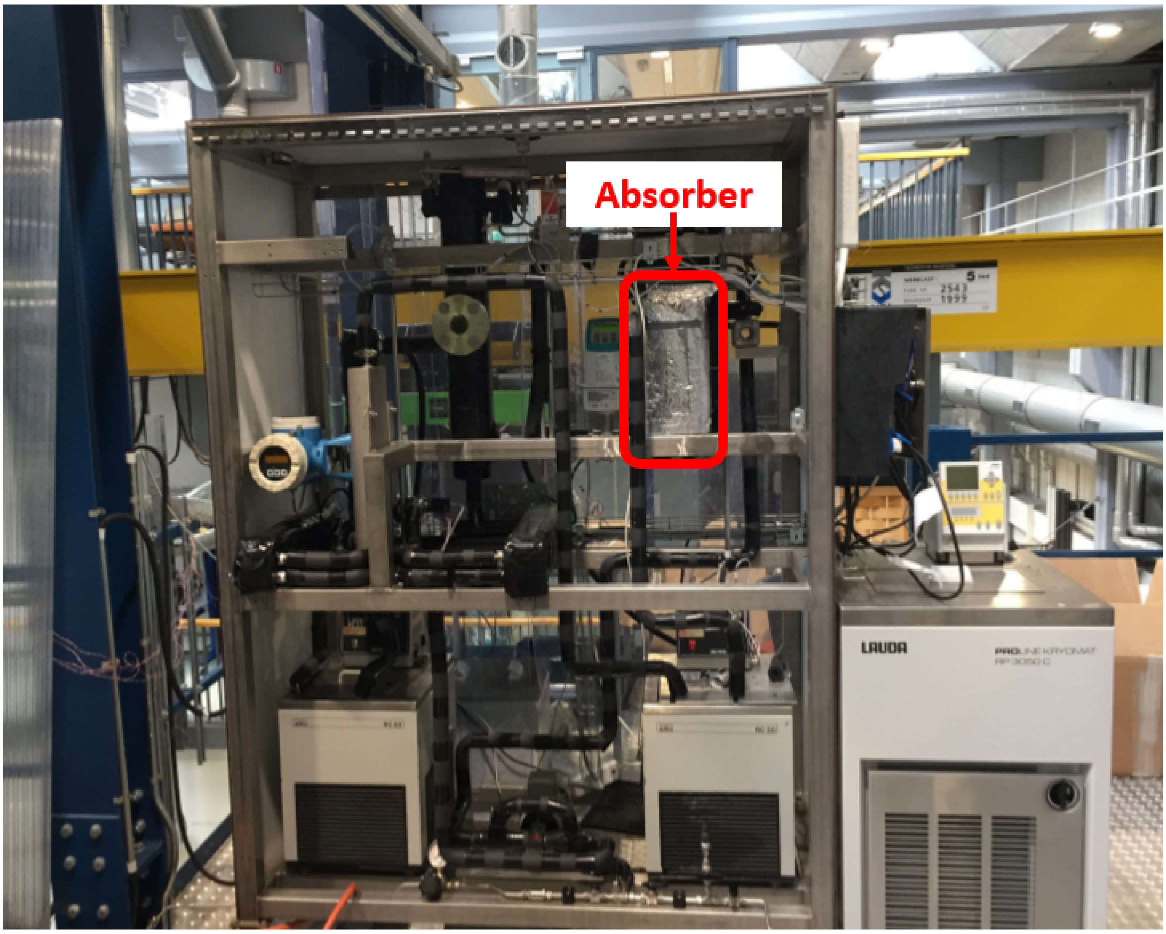

Figure 4.1: Experimental setup for the absorption process at the Energy and Process department at TU Delft

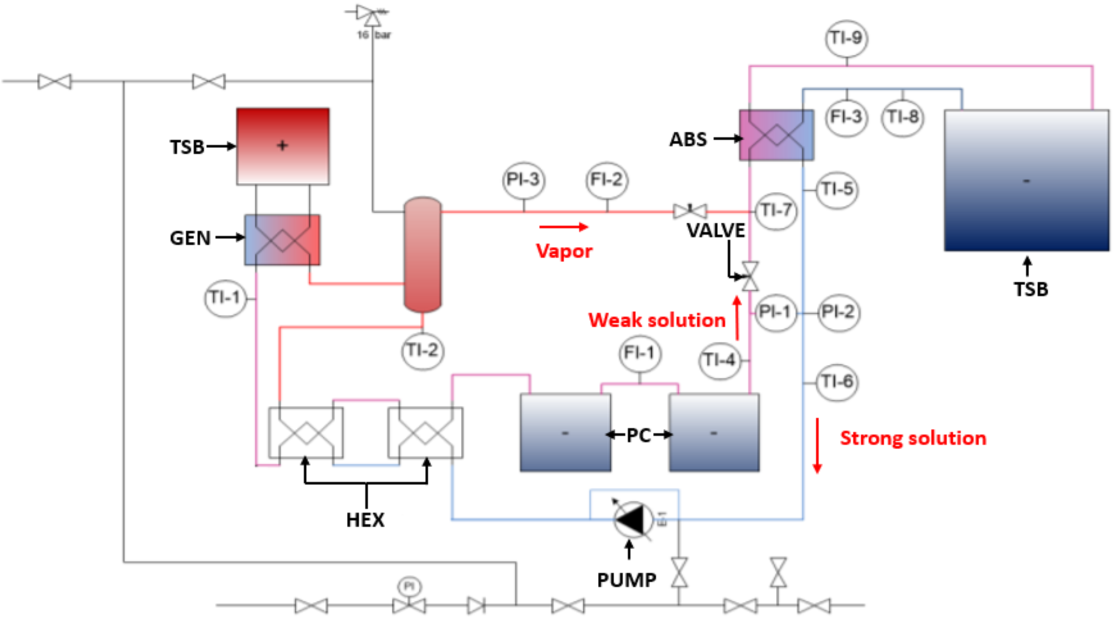

Figure 4.2: Schematic of experimental setup before being modified (Schilperoort et al., 2019)

Experiments are performed in two stages. Water- water experiments are performed initially to obtain and validate the heat transfer correlation. Later, the system is filled with 0.30 kg of ammonia and 4.70 kg of [emim][SCN] for stage 1 experiments and the actual absorption process is carried out and studied.

4.1.1. Working of the setup

The absorber is a plate heat exchanger in which cooling water flows through a total of seven channels and ammonia + [emim][SCN] solution flows through a total of six channels, in the opposite direction to that of the cooling water (counter-current flow). In the absorber (ABS), ammonia vapor is absorbed into the solution, thus releasing heat. This released heat is exchanged with the cooling water, which gets heated up. After absorbing ammonia vapor in the absorber, the strong solution that has higher weight concentration of ammonia, is pumped to the generator pressure by a pump (PUMP). This strong solution at high pressure passes through two consecutive heat exchangers (HEX) where it gains heat from the hot weak solution coming out of the generator. After the heat exchanger, the strong solution enters the generator (GEN). Heat is provided to the generator with the help of a thermostatic bath (TSB) operating within the temperature range of 90 ° C- 120 ° C. In the generator (GEN), due to the heat provided, ammonia vaporises as it's boiling point is reached. It should be noted here that it is assumed in this study, that [emim][SCN] does not vaporise since it has negligible vapor pressure. The vaporized ammonia is throttled and then is sent back to the absorber (ABS) to be absorbed in the solution.

The weak solution that comes out of the generator (GEN) is passed through two heat exchangers (HEX), where it exchanges heat with the strong solution going into the generator (GEN), and cools down. This weak solution then passes through two precoolers (PC) and cools down further. After the precoolers (PC), it is passed through a valve (VALVE) to get throttled to the absorber pressure. This weak solution at the absorber pressure enters the absorber (ABS) along with the throttled ammonia vapor from the generator, also at the absorber pressure. This process constitutes one absorption cycle, and this whole cycle is repeated.

The sensors denoted by 'TI' in figure 4.2 represent the temperature sensors, those denoted by 'PI' are the pressure sensors and the ones denoted by 'FI' are the flow meters. With the help of these various sensors, pressure, temperature and the flow at various points in the system can be measured and recorded with the help of a data logger. These results are further used to calculate the heat transfer coefficient of the system.

Table 4.1 lists the locations of various sensors in the experimental setup.

Table 4.1: Locations of the sensors used

Location of the sensors used		
Sensor	Type of the sensor	Location
FI-1	Density meter	Before ABS at the absorber side
FI-2	Gas flow meter	After the separator along the pipeline that connects to ABS inlet
FI-3	Volume flow meter	At the inlet to ABS at the coolant side
PI-1	Pressure sensor	In between the inlet and outlet of ABS
PI-2	Pressure sensor	At the outlet of ABS at the absorber side
PI-3	Pressure sensor	At the outlet of GEN
TI-1	Temperature sensor	At the inlet of GEN
TI-2	Temperature sensor	At the outlet of GEN
TI-4	Temperature sensor	At the inlet of ABS at the absorber side
TI-5	Temperature sensor	At the outlet of ABS at the absorber side
TI-8	Temperature sensor	At the outlet of ABS at the coolant side
TI-9	Temperature sensor	At the inlet of ABS at the coolant side

Table 4.2 lists the models of the various sensors and other equipment used in the experimental setup.

Table 4.2: models of the various sensors and other equipment used in the experimental setup

Models of the equipment used		
Sensor	Type of the sensor	Model
FI-1	Density meter	Endress + Hauser Proline Promass 80 A
FI-2	Gas flow meter	Bronkhorst Flow Controller F - 201AV - 50K - RAD - 44-V
FI-3	Volume flow meter	Siemens SITRANS F M MAG 5000
PI-1	Pressure sensor	Siemens Sitrans P500 HART
PI-2	Pressure sensor	Siemens Sitrans P - DS3 HART
PI-3	Pressure sensor	Wika Pressostat PSD - 30
TI-X	All temperature sensors	Pt - 100 precision temperature sensor
GEN side TSB	Thermostatic bath	Lauda ECO -RE2025S
CW side TSB	Thermostatic bath	Lauda Proline Kryomat RP3050C
PC	Precoolers	Lauda RC20
PUMP	Pump	Siemens ILA7070 - 2AA1

Table 4.3 lists the functions performed and the accuracies of the sensors used in the experimental setup.

Table 4.3: Accuracy of the sensors used

Accuracy of the sensors used		
Symbol	Function	Accuracy
FI-1	Measurement of the flow of the solution going into ABS	±0.5 $\mathrm{kg/m^3}$
FI-2	Measurement of the vapor flow going into ABS	±0.5 % RD + ±0.1 % FS
FI-3	Measurement of the cooling water going into ABS	0.4 % FS
PI-1	Measurement of the pressure drop across ABS	≤ 0.03 % FS
PI-2	Measurement of the solution pressure coming out of ABS	≤ 0.065 % FS
PI-3	Measurement of the pressure at GEN	≤ 0.065 % FS
TI-X	Measurement of the temperatures	±1 % 0.01 K after calibration

4.2. Geometry of the absorber : PHX

The absorber is a counter- flow plate heat exchanger. Plate heat exchangers exhibit higher efficiency of the heat transfer owing to higher heat transfer area and the added swirl to the flow due to the currugations as compared to other types of heat exchangers. The heat exchanger in question has corrugations on the surface, in order to increase the effective heat transfer area. Schematic of the PHX cross section is shown in figure 4.3.

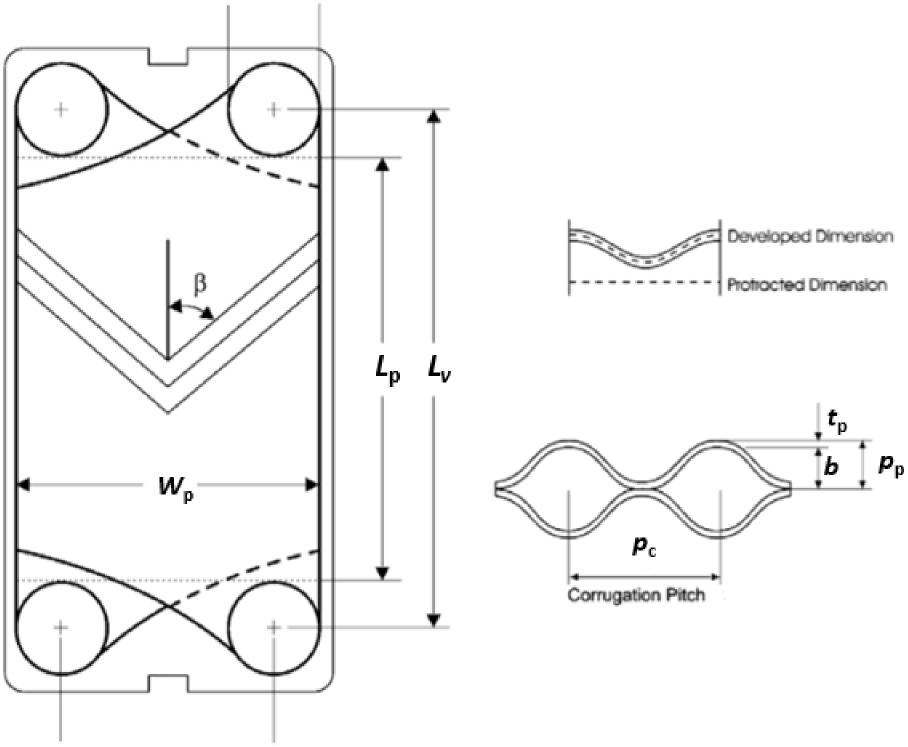

Figure 4.3: Cross section of the plate heat exchanger (Khan et al., 2010)

The geometric parameters of the PHX used in the experimentation are listed in table 4.4. Hydraulic diameter of the channel is calculated using equation 4.1, as proposed by Bell (2019).

$$d_\mathrm{h} = \frac{2L_\mathrm{g}W_\mathrm{p}}{L_\mathrm{g} + W_\mathrm{p}\phi} \tag{4.1}$$

Table 4.4: Details of the PHX geometry

Details of the PHX geometry			
Parameter	Symbol	Value	Unit
Number of plates	n_p	14	-
Number of channels	n_ch	13	-
Thermal conductivity of plates	λ_p	16.3	W/m-K
Corrugation depth	b	0.00188	m
Corrugation pitch	P	0.00348	m
Thickness of the plate	t_p	0.0004	m
Length of the plate	L_p	0.467	m
Width of the plate	W_p	0.114	m
Total heat transfer area	A_ht	0.71	m^2
Volume per channel	V	0.00010	m^3
Plate spacing	L_sp	0.002	m
Plate gap	L_g	0.0018	m

Φ from equation 4.1 is the surface enlargement factor which is the ratio of total effective heat transfer area to the planar plate area. It is calculated as

$$\Phi = \frac{A_\mathrm{ht}}{12W_\mathrm{p}L_\mathrm{p}} \tag{4.2}$$

4.3. Processing of the experimental data

4.3.1. Water - water experiments

In this case, the fluid at both sides of the heat exchanger is water. No phase change is involved.

Low Reynolds number experiments

Water- water experiments are performed in order to test the setup and to obtain the trend of the heat transfer in case of water. This experimentation is performed for different flows of both the cooling water and the absorber side water flow. Flows are varied for every reading. Temperature conditions are as follows - $T_{\text{gen}}/T_{\text{con}}\ /T_{\text{abs}}\ /\ T_{\text{eva}}$ = 95/45/45/10 ° C. These temperature conditions are maintained for every reading of the low Reynolds number experimental data points. The low Reynolds experiments are to be performed with equal Reynolds number at the absorber side and the coolant side. Thus, the heat transfer coefficient on each side is equal in this case. To achieve the condition of equal Reynolds numbers, the flows on the coolant and absorber sides are taken in the ratio of 7:6, owing to the fact that there are seven channels in the coolant side and six on the absorber side in the plate heat exchanger in the setup. The procedure followed is discussed in the next paragraphs.

The heat transferred at both the coolant and the absorber side are equated. For this, the heat transferred at the cooling water side is determined using the temperature readings.

$$\dot{m}_{\text{abs}} c_{p,\text{abs}} (\Delta T)_{\text{abs}} = \dot{Q}_{\text{abs}} \tag{4.3}$$

Further, using the known heat transfer area and the Logarithmic Mean Temperature Difference (LMTD), the overall heat transfer coefficient is calculated. LMTD is calculated as

$$LMTD = \frac{(T_{\text{abs,in}} - T_{\text{cw,out}}) - (T_{\text{abs,out}} - T_{\text{cw,in}})}{ln\frac{(T_{\text{abs,in}} - T_{\text{cw,out}})}{(T_{\text{abs,out}} - T_{\text{cw,in}})}} \tag{4.4}$$

The overall heat transfer coefficient (U) is

$$U = \frac{\dot{Q}_{\text{abs}}}{A_{\text{ht}} LMTD} \tag{4.5}$$

Where A_{ht} is the total heat transfer area. Using the heat network relation for the system, we can calculate the absorber side heat transfer coefficient as follows

$$\frac{1}{U} = \frac{1}{\bar{\alpha}_{\text{cw}}} + \frac{1}{\bar{\alpha}_{\text{abs}}} + \frac{t}{\lambda_{\text{p}}} \tag{4.6}$$

Further, heat transfer coefficient on the coolant side is calculated using equation 4.7, as both coefficients are equal in this particular case.

$$\bar{\alpha}_{\text{cw}} = \frac{2}{\frac{1}{U} - \frac{t}{\lambda_{\text{p}}}} \tag{4.7}$$

Using this coefficient and the known Reynolds number, a graph of f(Nu,Pr) versus Reynolds number can be plotted, and an empirical correlation can be obtained.

Higher Reynolds number experiments

Due to the fact that there is limitation to the speed of the pump on the absorber side of the heat exchanger, in order to obtain the experimental data for higher Reynolds numbers, a different procedure than the one described above is followed.

In this case, speed on the absorber side is kept constant, and the coolant speed is varied. The temperature conditions are kept same as above. Again, the heat transfer coefficient on the coolant side is calculated as per equation 4.6; as in this case the two heat transfer coefficients are not the same. Heat transfer coefficient on the absorber side can be found out using the previously developed empirical relation for the low Reynolds number (listed asequation 4.8).

The data obtained from both these cases are plotted in the graph to obtain the overall empirical correlation.

4.3.2. Viscosity check

After the water-water experiments have been performed, a separate set of experiments was performed wherein the convective heat transfer between ammonia + [emim][SCN] solution and water was measured and recorded experimentally in order to attempt to predict the behaviour of the viscosity of ammonia + [emim][SCN] solution with changes in the operating conditions.

These experiments were performed to attempt to validate the viscosity of the solution as a logarithmic function of the viscosities of the individual fluids. There is no absorption of ammonia vapor in the ammonia + [emim][SCN] solution in this set of experiments. Just the fluid-fluid convective heat transfer experiments were performed with ammonia + [emim][SCN] solution and cooling water. The pump that pumps the solution in the experimental setup has a higher limit to which it can pump the solution, thus restricting the speed of the solution in the setup. As a result, the data points obtained were in a low range of Reynolds numbers. The empirical correlation as obtained from the Nusselt-Reynolds-Prandtl plot, as a result of the water - water experiments for the low Reynolds numbers is solved for the value of the viscosity. This equation is mentioned below.

$$\mathrm{Nu} = 0.275\mathrm{Re}^{0.684}\mathrm{Pr}^{0.333} \tag{4.8}$$

This equation was obtained from the experimental readings of the water - water experiments for Reynolds numbers in the range between 48 and 140. Since this correlation was obtained for water-water convective heat transfer experimentation, it can also be considered to govern the convective heat transfer between the ammonia + [emim][SCN] solution and water.

In order to check for the value of the viscosity, the thermophysical properties of the solution [emim][SCN]+ammonia at the operating conditions used are used in equation 4.9.

$$\mu = \left(\frac{0.275c_{p\mathrm{sol}}^{0.333}\lambda_{\mathrm{sol}}^{0.666}G_{\mathrm{sol}}^{0.684}}{\bar{\alpha}_{\mathrm{abs}}d_{\mathrm{h}}^{0.316}}\right)^{\frac{1}{0.351}} \tag{4.9}$$

The absorber side heat transfer coefficients, temperatures and the flow rates are obtained from the fluid-fluid heat transfer experiments. Equation 4.9 is solved for the value of the viscosity for five data points and a comparison is made between the values of viscosity obtained from equation 4.9, and those obtained from equation 3.4, which depicts the viscosity of the solution to be a logarithmic function of the individual fluid viscosities. Along with the logarithmic relation, a linear relation is also used to calculate the viscosity values for comparison. This linear equation is as follows.

$$\mu_{\mathrm{sol}} = w_{\mathrm{IL}}\mu_{\mathrm{IL}} + w_{\mathrm{NH_3}}\mu_{\mathrm{NH_3}} \tag{4.10}$$

A Matlab code is designed for this purpose. The equation for the viscosity of [emim][SCN]+ ammonia solution - both in logarithmic and the linear forms- are checked, and the deviation of those values from the actual rough estimate of the viscosity as from equation 4.9. The methodology of these experiments is explained in the following sections.

4.3.3. Ammonia- ionic liquid experiments

In this case, the fluid at absorber side is [emim][SCN] and ammonia, whereas coolant is water. Of the total amount of fluid ([emim][SCN]+ammonia), the mass of ammonia was to be 6%. Weak solution enters the absorber, absorbs ammonia, and leaves as a strong solution. In the generator, ammonia vaporizes and the vapour stream is separated from the weak solution. Using the density meter before the entrance of the absorber in the setup, the concentration of ammonia in the weak solution can be derived. This calculation is shown in equation 4.11.

$$w_{\mathrm{NH_3,weak}} = \frac{\rho_{\mathrm{IL}} - \rho_{\mathrm{sol}}}{\rho_{\mathrm{IL}} - \rho_{\mathrm{NH_3}}} \tag{4.11}$$

Thermodynamic and transport properties of ammonia at the saturated conditions are obtained from Refprop (Lemmon et al., 2010). Literature review is used to calculate the thermo-physical properties of [emim][SCN]. Further, the mass concentration of ammonia in the strong solution is calculated as per equation 4.12.

$$w_{\mathrm{NH_3,strong}} = \frac{\dot{m}_{\mathrm{v}} + w_{\mathrm{NH_3,weak}}\dot{m}_{\mathrm{IL}}}{\dot{m}_{\mathrm{v}} + \dot{m}_{\mathrm{IL}}} \tag{4.12}$$

After obtaining both the concentrations, the *PTw* diagram of this mixture can be used to check the experimental pressure and temperature readings. The cycle followed in **stage 1** of ammonia-ionic liquid experiments is as shown in figure 4.4.

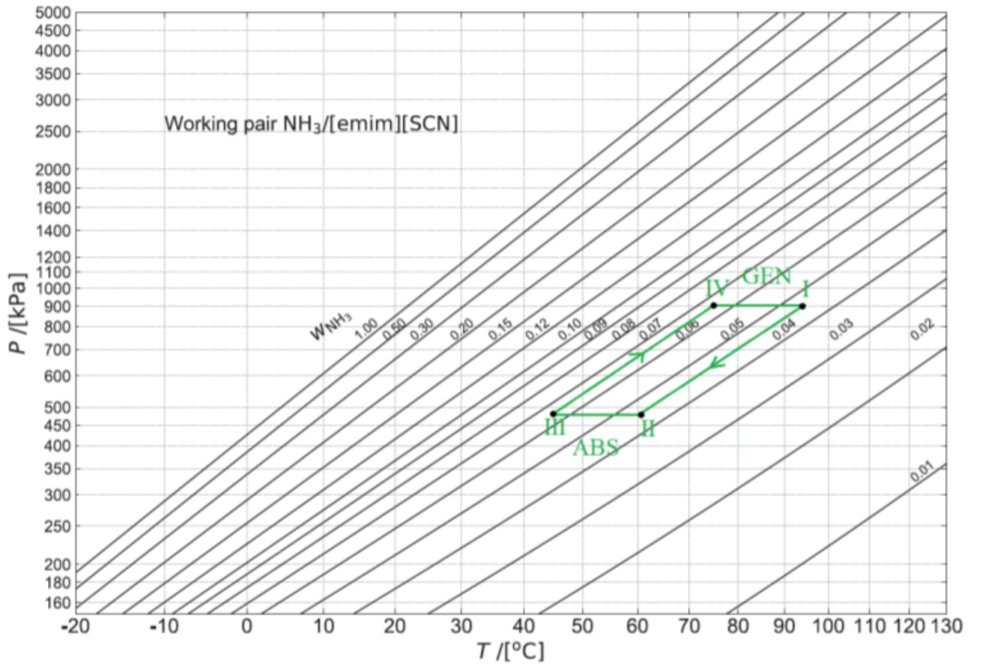

Figure 4.4: *PTw* diagram of [emim][SCN]+ammonia for initial (stage 1) experiments

As in the previous case, the overall heat transfer coefficient can be determined using equation 4.5. To calculate the absorber side heat transfer coefficient, equation 4.6 is used. The coolant side heat transfer coefficient can be calculated using previously derived empirical Nu-Re-Pr relation for water. Again, using this heat transfer coefficient, the Nu-Re-Pr correlation for [emim][SCN]+ammonia solution can be plotted.

4.4. Methodology : Water water experiments

To test the system, water water experiments are performed on the system and overall as well as the absorber side heat transfer coefficients are calculated. The following procedure is followed.

1. The system is emptied and vacuumized properly.
2. After this, water is filled into the system from the bottom, making use of the vacuum in the system, till half the level in separator (generator) is reached.
3. Later, nitrogen in gaseous state is filled into the system from the top of the setup, in order to pressurize the system.

4.4.1. Low Reynolds number experiments

Both the coolant side and the absorber side flows, in the ratio of 7:6, are varied from the lowest flow rate to the highest possible. Temperature and pressure conditions used are listed in table 4.5.

Table 4.5: Temperature and pressure conditions for low Reynolds number water-water experiments

Water-water experiments		
Parameter	Value	Unit
$T_{\text{cw,in}}$	20	°C
$P_{\text{abs,in}}$	6	bara

Flow rates used are listed in table 4.6.

Table 4.6: Flow rates for low Reynolds number water-water experiments

Water-water experiments					
Flow rates	Value				
$\dot{m}_{\text{abs}}$(kg/hr)	42.9	67.6	89.1	113.2	126.4
$\dot{V}_{\text{cw}}$(l/hr)	50.9	79.7	106.1	131.9	149.8

4.4.2. Higher Reynolds number experiments

For this case, absorber side flow rate is kept constant, and the coolant side flow is varied in steps. Temperature and pressure conditions applied follow.

Table 4.7: Temperature and pressure conditions for high Reynolds number water-water experiments

Water-water experiments		
Parameter	Value	Unit
$T_{\text{cw,in}}$	20	°C
$P_{\text{abs,in}}$	6	bara

The results obtained for these conditions are enlisted in the following chapter. The plots obtained are also included.

4.5. Methodology : Viscosity check

These experiments were performed with the gas valve completely closed, so as to prevent any absorption of the ammonia vapour into ammonia - [emim][SCN] solution. Flow rate of cooling water was kept constant as well as the temperature of the generator side thermostatic bath. Temperature of the cooling water entering the absorber was varied gradually and the temperature of the solution going into the absorber was adjusted accordingly for each variation of the cooling water temperature. The flow rate of the solution at which the absorber pressure could be stabilized, for each range of the solution temperature, was chosen. It should be noted that the maximum flow rate for a particular range of solution temperature is the one at which the generator side pressure and the temperature start to drop.

The experiments were performed for five such cases. The values of different parameters for these four data points are displayed in table 4.8.

Table 4.8: Temperature and mass flow values for viscosity check experiments

Viscosity check parameters						
Case	$T_{\text{cw,in}}$ (°C)	$T_{\text{abs,in}}$ (°C)	$T_{\text{abs,avg}}$ (°C)	$T_{\text{TSB,gen}}$ (°C)	$\dot{m}_{\text{abs}}$ (kg/hr)	$\dot{m}_{\text{cw}}$ (kg/hr)
1	24.94	34.61	29.84	87.76	92.23	201.44
2	24.94	45.98	35.59	85.25	101.43	201.83
3	34.97	55.71	45.44	87.15	100.00	202.11
4	40.00	59.87	50.08	91.45	76.27	202.09
5	50.11	64.24	57.20	90.91	45.49	200.77

Results obtained from these experiments are analysed with the help of a Matlab code and are presented in chapter 7.

4.6. Methodology : Ammonia- ionic liquid experiments

4.6.1. Ammonia- ionic liquid experiments stage 1

For the experimental validation of the numerical model, same setup as shown in figure 4.2 is used.

The system needs to be prepared before filling it with [emim][SCN] and ammonia. After the water-water experiments, the system is emptied from the bottom while being pressurized with the nitrogen from the top. To remove all the water that is inside the system, an extra nitrogen duct is connected from bottom of the system (from nitrogen supply) to the top of the system. The nitrogen that comes to the top of the system through this duct blows the system and the rest of the water comes out of the system from the bottom.

After this, the system is vacuumized for 24 hours to remove all the stray water vapor inside the system. Later, the system is kept under vacuum for 48 hours and checked if it retains it's pressure. This confirms that there is no leak in the system. This was an important step to be followed, considering the toxicity of ammonia.

First, about 4.70 kg of [emim][SCN] is sucked into the system from the valve at the bottom making use of the vacuum in the system. This task is performed making sure that no air enters the system. While filling the system, [emim][SCN] is weighed with the help of a scale. Later, 0.30 kg of ammonia is filled into the system from the bottom with the help of a vacuumized tube that is connected to a pressuarized ammonia tank. Thus, the mass concentration of ammonia in the solution being injected into the system is about 6 %. Once both the fluids are into the system, the pump is started to ensure their mixing and distribution in the system. In this case, the cooling water flow is kept constant and the absorber side flow ([emim][SCN] + ammonia) is varied. Results obtained from the system for this stage are shown in the following chapter.

4.6.2. Ammonia- ionic liquid experiments stage 2

After stage 1 experiments, the system was emptied of ammonia and [emim][SCN]. However, the system could not be emptied completely, and about 1 kg of [emim][SCN] was still remaining in the system. Some mechanical changes to the connections were made in order to gain better accuracy. Absorber side pressure sensor was placed after the valve. Gas flow meter at the generator side was changed and fixed. The system was re-insulated and was filled with 3.92 kg of [emim][SCN] and 0.32 kg of ammonia the same way as was done previously. So, the mass concentration of ammonia in the solution in the system just after filling the system was around 6.1 %.

A sketch of the setup as it was modified is shown in figure 4.5.

Preliminary experiments were run on the newly prepared system. Finally, stage two ionic liquid- ammonia experiments were performed. Coolant flow rate was kept constant and the absorber side solution flow rate was gradually increased. Readings were taken once the steady state was achieved for each individual absorber side flow rate, after all the temperatures are stabilized. 19 data points were obtained by these experiments. The temperature and pressure conditions listed in table 4.9 were maintained.

Table 4.9: Temperature conditions for ammonia- ionic liquid stage 2 experiments

Ammonia- ionic liquid experiments: Stage 2		
Parameter	Value	Unit
$T_{\text{cw,in}}$	45	°C
$T_{\text{TSB,gen}}$	95	°C

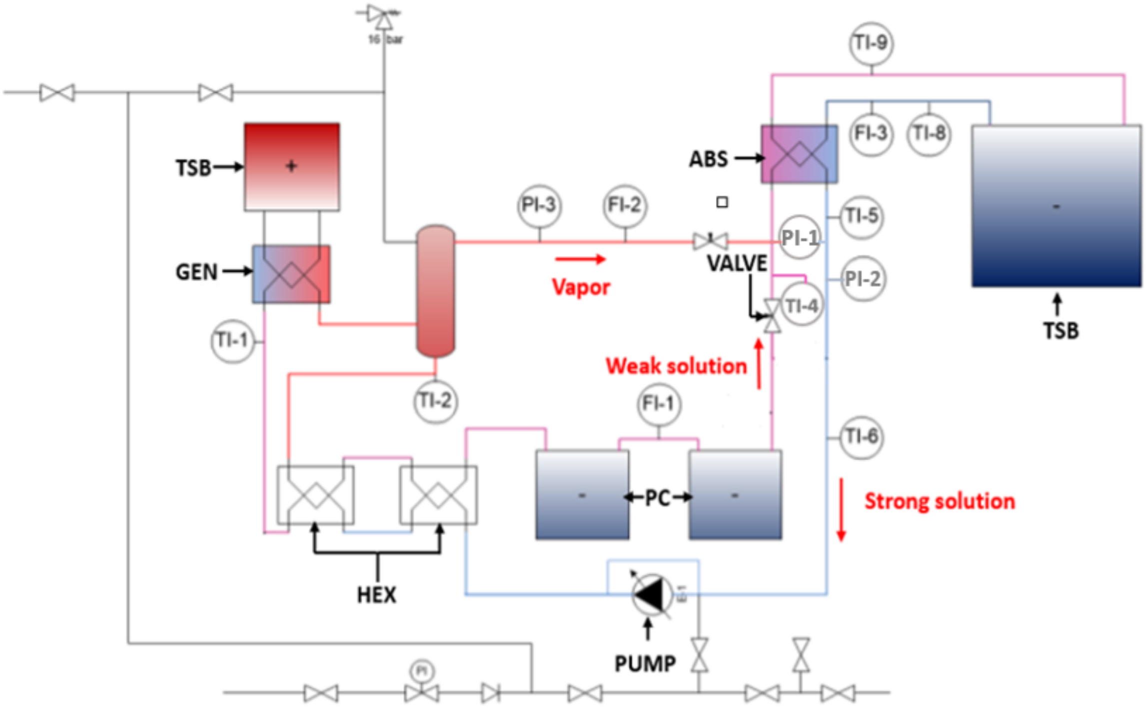

Figure 4.5: Experimental setup after the alterations used for stage 2 experiments

5

Experimental results and discussions

This chapter lists and explains the experimental results obtained in various sets of experiments.

5.1. Water water experiments

5.1.1. Low Reynolds number experiments

Water- water experiments were performed with the flow rates mentioned in section 4.4.1 and the results of the experimentation were evaluated with the help of a Matlab code designed to find out the overall heat transfer coefficient and also the absorber side heat transfer coefficient. Also, the Nusselt number as a function of the Prandtl number is plotted on a graph with the Reynolds numbers using the data points marking the flow rates mentioned in section 4.4.1. The correlation thus obtained closely resembles the ones previously obtained in various literature (Khan et al., 2010, Yan and Lin, 1999, Winkelmann, 2010, Donowski and Kandlikar, 1999, Amaris Castilla et al., 2014, Kuikhoven, 2019, Towler and Sinnott, 2013). This shows that the setup is working satisfactorily. The graph as plotted and the relation as obtained in Matlab are shown in figure 5.1.

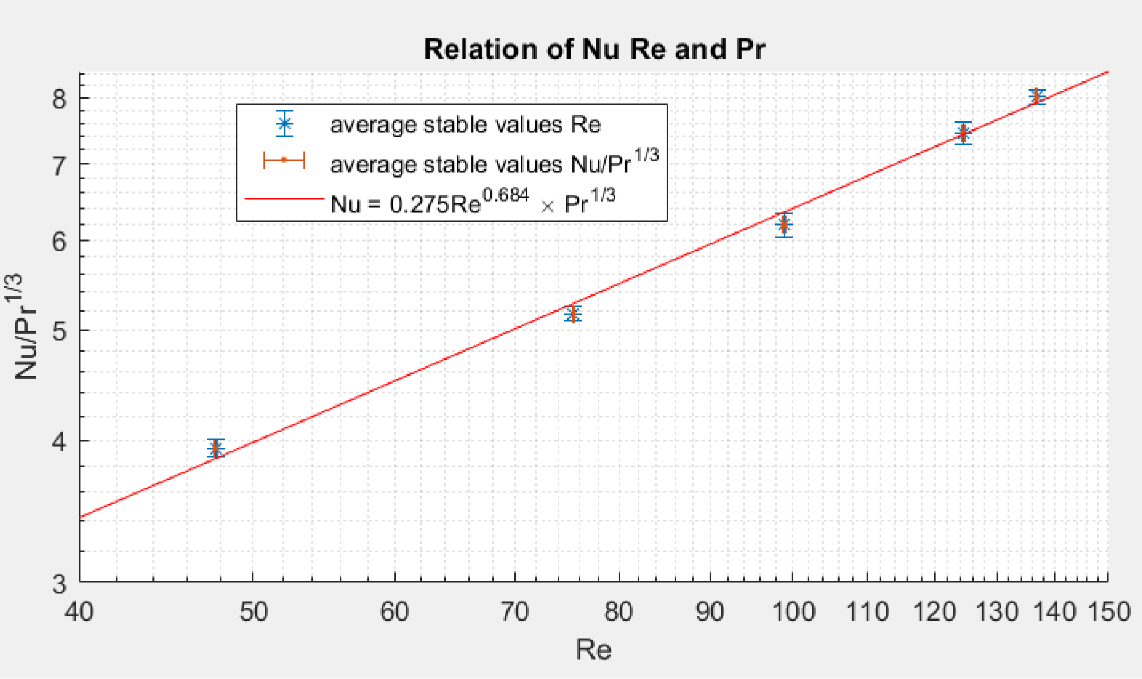

Figure 5.1: Empirical correlation obtained for low Reynolds number

The graph of coolant side heat transfer coefficient and the Reynolds number in the low ranges was plotted on a log-log scale and is displayed in figure 5.2.

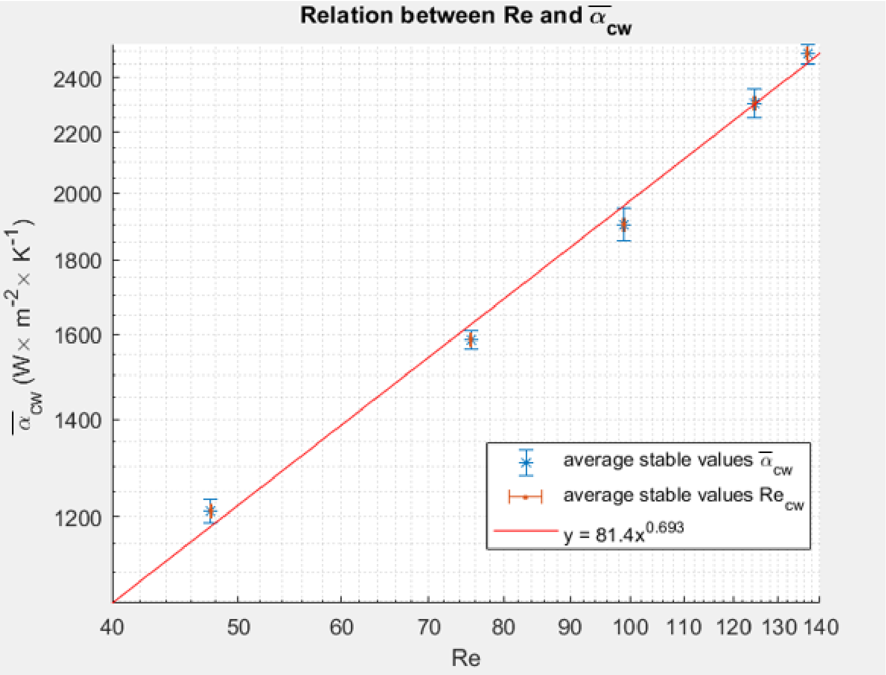

Figure 5.2: Relation between coolant side heat transfer coefficient and the low range Reynolds number

It can be seen that, as expected (Mills, 2015), the heat transfer coefficient on the cooling water side increases exponentially with the Reynolds number, and thus, the flow of the cooling water.

Figure 5.3 shows the variation of the heat transfer coefficient on the coolant side with time.

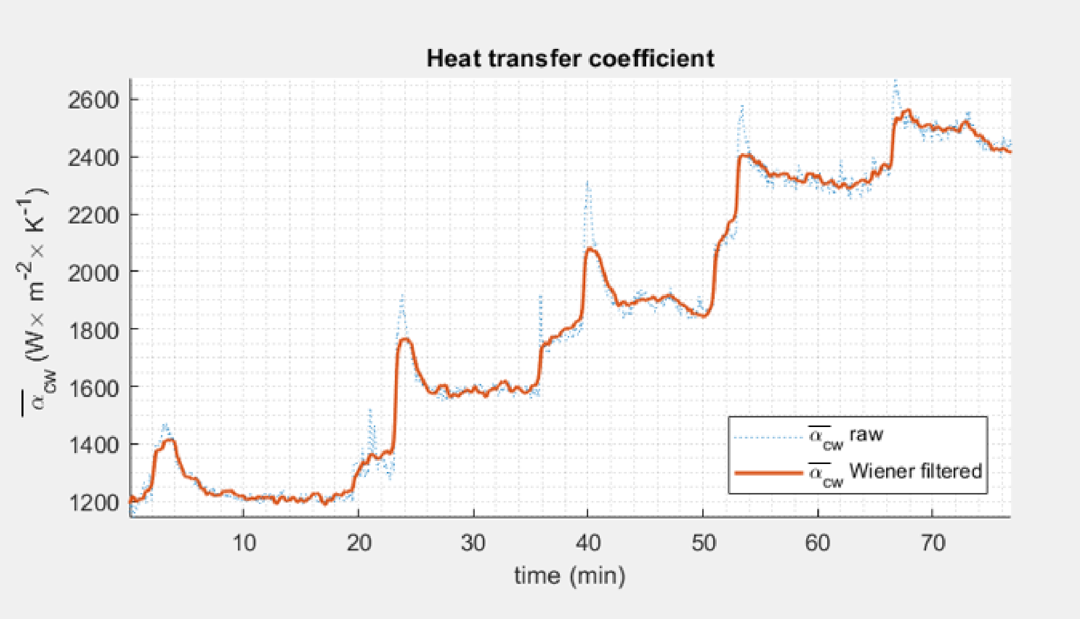

Figure 5.3: Plot of coolant side heat transfer coefficient for low Reynolds numbers versus time

It can be seen that $\bar{\alpha}_{cw}$ increases as the cooling water flow is increased with time.

5.1.2. Higher Reynolds number experiments

Experiments were performed for higher flows of water as mentioned in section 4.4.2. A relation between f(Nu-Pr) and the Reynolds number was obtained for these higher Reynolds numbers in the same way as that for the low Reynolds number. This obtained relation and the plot of the f(Nu-Pr) and the higher range Reynolds numbers are shown in figure 5.4.

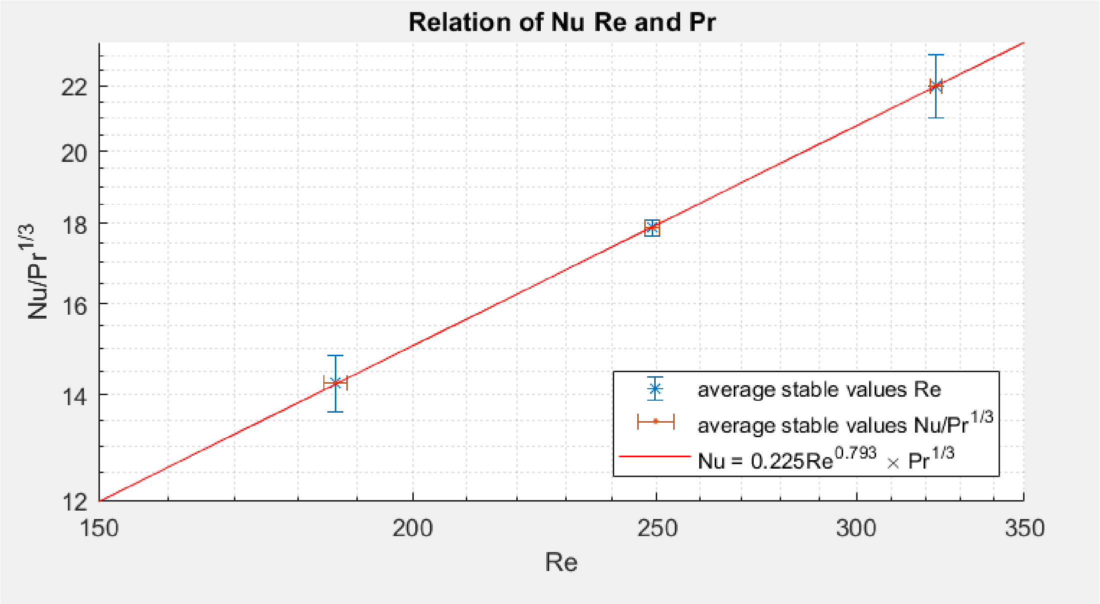

Figure 5.4: Empirical correlation obtained for higher Reynolds numbers

Also, with the help of the same code, a relation between the coolant side heat transfer coefficient and the Reynolds number over all ranges is plotted on a log-log scale. This graph is shown in figure 5.5. It is observed from figure 5.5, that, again, as expected (Mills, 2015), it is observed that the heat transfer coefficient on the cooling water side increases almost linearly with the flow of the cooling water.

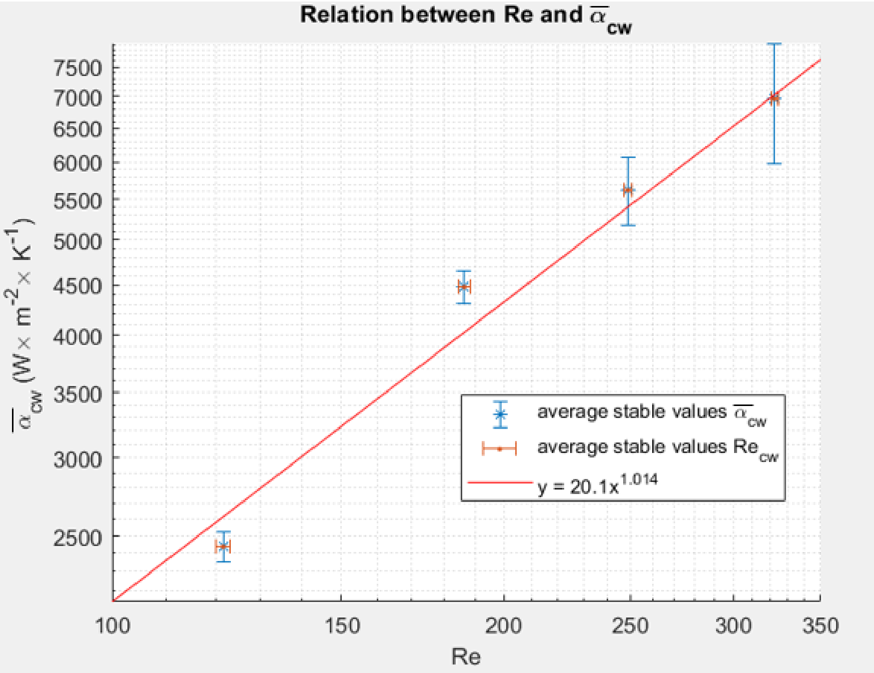

Figure 5.5: Relation between coolant side heat transfer coefficient and the higher range Reynolds number

Figure 5.6 shows the variation of the heat transfer coefficient with the time.

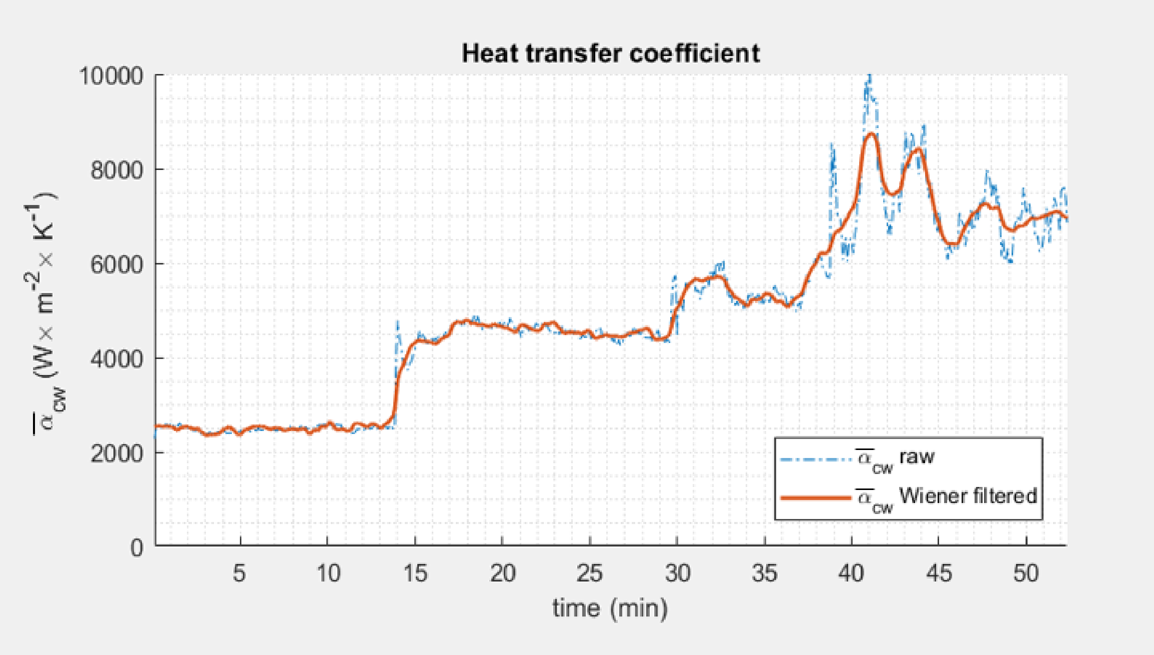

Figure 5.6: Plot of coolant side heat transfer coefficient for higher Reynolds numbers versus time

It can be noticed here as well, that $\bar{\alpha}_{cw}$ increases with the time, as the cooling water flow is increased. Overall plot of f(Nu-Pr) and the Reynolds number was plotted for all the ranges of Reynolds number, with the help of the Matlab code. This graph is displayed in figure 5.7.

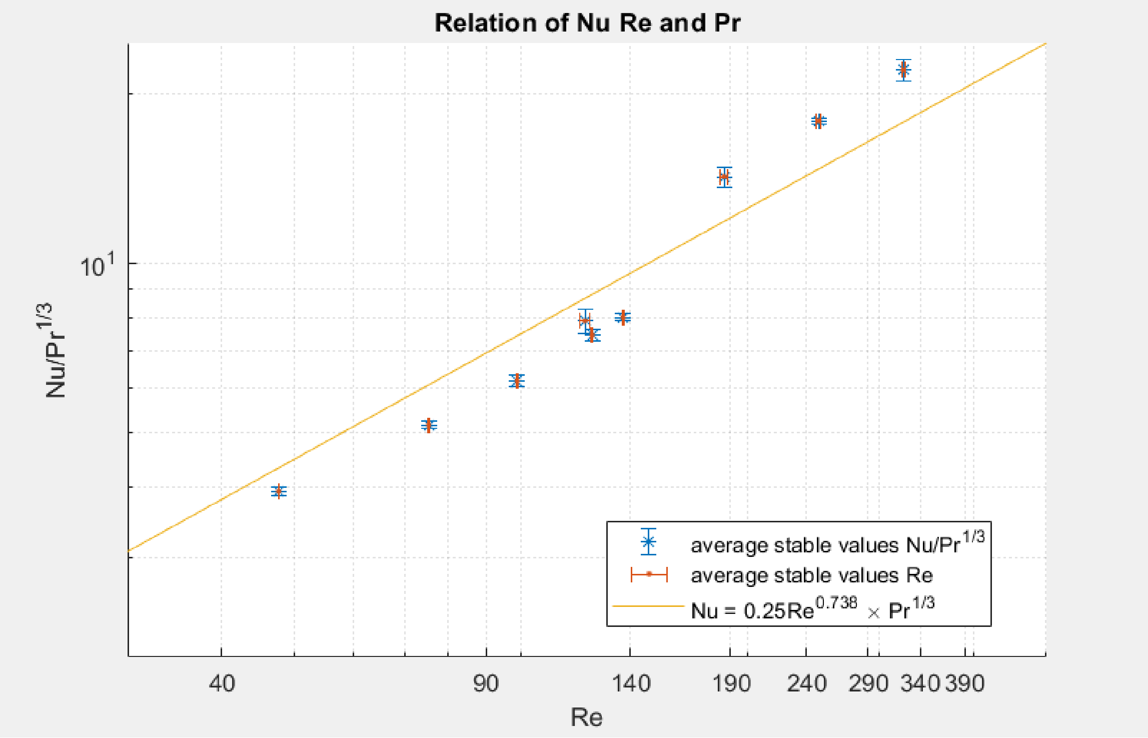

Figure 5.7: Overall convective heat transfer correlation obtained

The relation at the bottom right corner represents the overall f(Nu-Pr) and the Reynolds number empirical relation for water. It is listed as equation 5.1.

$$\text{Nu} = 0.25\text{Re}^{0.738}\text{Pr}^{0.333} \tag{5.1}$$

In the numerical modelling of the absorption process, these derived correlations will be used to get the temperature outputs, as the correlation that governs convective heat transfer between the cooling water and the [emim][SCN] solution. As equation 5.1 yields reasonably close outputs from the experimental data, it can be safely said, that it is acceptable.

5.2. Ammonia- ionic liquid experiments

5.2.1. Stage 1

As explained in section 4.6.1, the flow rate of the cooling water is maintained constant and that of the solution going into the absorber is gradually increased. Four such data points, or cases, were obtained. The values of various properties obtained at these data points are shown in tables 5.1, 5.2 and 5.3.

Table 5.1: Steady state readings for ammonia- ionic liquid stage 1 experiments

Case	$P_{\text{abs,in}}$ (kPa)	$\dot{m}_{\text{abs}}$ (kg/hr)	$\dot{m}_{\text{cw}}$ (l/hr)
1	487.4	58.4	59.7
2	480.1	78.7	58.1
3	511.8	103.9	60.0
4	490.60	131.1	61.9

Table 5.2: Steady state temperature readings for ammonia- ionic liquid stage 1 experiments

Case	$T_{\text{gen,out}}$ (°C)	$T_{\text{abs,in}}$ (°C)	$T_{\text{abs,out}}$ (°C)	$T_{\text{cw,out}}$ (°C)	$T_{\text{cw,in}}$ (°C)
1	96.1	60.0	42.9	50.4	42.8
2	96.4	60.2	43.6	53.3	42.7
3	95.9	60.4	44.7	55.0	42.8
4	91.9	60.8	45.6	56.8	42.7

Table 5.3: Steady state heat transfer parameters for ammonia- ionic liquid stage 1 experiments

Case	$\dot{Q}$ (W)	$\bar{\alpha}_{\text{abs}}$ (W/m^{2}K)	*LMTD* (°C)	*U* (W/m^2 K)
1	524.7	406.1	2.4	306.2
2	688.1	449.3	2.9	330.4
3	854.0	505.6	3.3	362.8
4	1029.0	645.7	3.3	433.7

However, during these stage 1 experiments, the gas flow meter on the generator side was found to be faulty. Thus, the gas flow rate readings are not shown here. Also, it was noticed that the pressure sensor that measures the pressure drop across the absorber (PI-1) was placed before the throttling valve, thus not recording the correct value for the pressure drop across the absorber. It was also seen that the pressure sensor measuring the generator pressure (PI-3) was not functioning as expected.

So, a decision was made to replace the faulty gas flow mater, and the generator side pressure sensor (PI-3) and repeat the ammonia - [emim][SCN] experiments in order to improve the accuracy of the calculations. In addition to this, some mechanical changes were made in the system connections that placed the pressure sensor measuring the pressure drop across the absorber (PI-1), after the throttling valve, so as to get accurate pressure drop readings.

5.2.2. Stage 2

During the experimentation, the ammonia gas flow from the generator and going back into the absorber was measured separately in a different software, and the rest of the data was recorded separately in the same data logger as used for stage 1 experiments. All the other readings other than the gas flow, were updated after every 10 seconds. However, the gas flow rate readings were recorded with the time interval of 1 second. Thus, these readings are averaged every 10 seconds to correspond them with the rest of the readings. For recording the gas flow rate, a Bronkhorst gas flow meter was used. This flow meter was originally calibrated for hydrogen. So, a correction factor had to be applied to the recorded values of the gas flow rate for the working fluid (ammonia). Using the online calculator by the company, the conversion factor of 1/1.39 was calculated for ammonia, and applied to the readings obtained from the gas flow meter. Solution and gas flow rates, originally measured in different units into the software are converted to kg/h for the ease of the calculations.

The pump has a limit on the highest value of the speed it can attain, which in turn, puts a restriction on the maximum solution velocity that can be set. Solution flow into the absorber was gradually increased from a low value to the highest possible one. Data points were recorded when a steady state was seen to be attained by the system for every flow rate of the solution into the absorber, ie, when absorber pressure attains a steady value. 19 such data points at different flow rates were obtained. Gas flow rate values were correlated with these data points.

Table 5.4 shows the calculations performed to obtain the pressure of the solution going into the absorber, as the absorber side pressure sensor is placed after the absorber (PI-2). The pressure loss in the absorber as recorded by the sensor PI-1 is to be added to the value of pressure of the solution coming out of the absorber.

Table 5.4: Calculation for the Pressure of the solution going into the absorber

Case	$P_{\text{abs,out}}$ (kPa)	ΔP_{abs} (KPa)	$P_{\text{abs,in}}$ (kPa)
1	239.6	2.81	242.4
2	506.5	5.36	511.9
3	496.4	5.80	502.2
4	501.4	5.81	507.3
5	386.2	5.39	391.6
6	365.3	5.35	370.7
7	294.4	4.97	299.4
8	283.9	5.12	289.0
9	260.7	7.33	268.0
10	222.5	7.17	229.7
11	216.3	7.18	223.5
12	265.2	10.04	275.2
13	263.0	10.03	273.0
14	342.9	15.22	358.1
15	330.1	10.72	340.9
16	239.5	19.06	258.6
17	235.5	18.64	254.2
18	340.0	15.20	355.2
19	335.9	15.16	351.1

Table 5.5 below shows the shortlisted experimental readings from stage 2 experiments. The values represented in this table are the ones that are given as inputs to the numerical model developed for the absorption process. Complete experimental data for stage 2 experiments is displayed in figure 32, Appendix A. In figure 32, the first five data points have a different background color than the rest, which is a representation of the lower mass flow rates of the cooling water (FI -3) that were set for these first five data points.

Table 5.5: Steady state readings for ammonia- ionic liquid stage 2 experiments

Case	$\dot{m}_{\text{abs}}$ (kg/hr)	$T_{\text{abs,in}}$ (°C)	$T_{\text{abs,out}}$ (°C)	$w_{\text{NH}_3\text{,weak}}$ (kg/kg)	$\dot{m}_{\text{v}}$ (kg/hr)	$P_{\text{abs,out}}$ (kPa)	$P_{\text{abs,in}}$ (kPa)	$\dot{m}_{\text{cw}}$ (kg/hr)	$T_{\text{cw,in}}$ (°C)	$T_{\text{cw,out}}$ (°C)	$\dot{Q}/A$ (W/m^2)	U ($\text{W/m}^2 - \text{K}$)
1	35.2	54.9	44.8	0.023	4.91 E-02	239.6	242.4	53.9	44.8	47.8	239	180.4
2	57.7	55.4	44.8	0.023	2.18 E-02	506.5	511.9	53.7	44.8	49.2	401	412.6
3	61.1	55.4	44.8	0.023	2.26 E-02	496.4	502.2	54.1	44.8	49.7	431	381.8
4	61.2	55.3	44.8	0.023	2.34 E-02	501.4	507.3	53.3	44.8	49.8	434	415.8
5	58.0	55.5	44.8	0.023	3.71 E-02	386.2	391.6	53.5	44.8	49.8	436	424.7
6	57.6	55.8	44.9	0.022	5.98 E-02	365.3	370.7	103.7	45.0	47.4	410	327.4
7	54.6	55.4	45.0	0.023	5.77 E-02	294.4	299.4	103.3	45.0	47.2	373	237.9
8	55.1	55.4	45.0	0.023	5.83 E-02	283.9	289.0	103.9	45.0	47.2	376	239.5
9	72.3	55.6	45.0	0.023	9.12 E-02	260.7	268.0	103.5	44.9	48.0	506	399.5
10	67.6	55.5	45.0	0.023	9.68 E-02	222.5	229.7	103.5	44.9	47.8	473	358.6
11	65.4	55.5	45.0	0.023	5.38 E-02	216.3	223.5	103.2	44.9	47.7	458	320.2
12	90.3	55.7	45.1	0.022	1.35 E-01	265.2	275.2	103.3	44.9	48.7	630	336.9
13	90.2	55.7	45.1	0.023	5.38 E-02	263.0	273.0	104.2	44.9	48.7	633	344.6
14	118.4	56.0	45.0	0.022	5.73 E-02	342.9	358.1	103.0	45.0	49.7	800	349.4
15	94.5	55.7	45.1	0.022	1.71 E-01	330.1	340.9	104.3	45.0	48.8	654	354.7
16	137.3	56.1	45.8	0.022	2.49 E-02	239.5	258.6	103.3	44.9	50.4	926	359.8
17	136.5	56.0	45.8	0.022	3.20 E-02	235.5	254.2	103.6	44.9	50.4	919	363.6
18	118.4	56.0	45.4	0.022	3.66 E-02	340.0	355.2	103.0	44.9	49.8	818	359.6
19	118.3	56.0	45.4	0.022	3.03 E-02	335.9	351.1	103.3	44.9	49.8	816	358.9

Following observations could be made from the experimental results.

1. First five readings were taken with the cooling water flow rate of about 55 kg/h, and the rest were taken with the flow rate of about 100 kg/h. It can be seen that the overall heat transfer coefficient is larger for a lower flow rate of the cooling water. This results from the fact that the logarithmic mean temperature difference is larger for the higher flow rate of the cooling water. Also, the fact that the readings that were taken with the higher flow rate of the cooling water were also taken with the higher absorber side solution flow rate, contributes to this observation.

2. It comes to the notice, that the concentration of ammonia in ammonia + [emim][SCN] solution going into the absorber is very low in all the 19 cases (around 2.5 %), considering that originally about 6.1% of ammonia was filled in the system. It could have been due to one of the following reasons, or a combination of these reasons.

    (a) During the execution of the experiments, ammonia vapor accumulates in the separator, owing to a low level of the solution in the separator. So, the vapor flow was also low and the weight percent of ammonia in the solution recorded before entering the absorber, was low. This would mean that the assumption of the vapor - liquid equilibrium at the outlet of the generator, is not valid.

    (b) $w_{\mathrm{NH_3,weak}}$ is calculated with the value of the density as displayed by the density meter, as per equation 4.11. This density meter is placed before one of the precoolers, in which ammonia + [emim][SCN] solution gets cooled down. The temperature sensor (TI-4) is placed after the precooler. Thus, the temperature displayed by this sensor is the temperature of the solution just before entering the absorber. However, the density meter shows the density of the solution before it enters the second precooler. Thus, there is a discrepancy in the temperature and density readings recorded. The densities of the individual fluids to be used in equation 4.11 are calculated at the temperature displayed by TI-4. Thus, the actual density of the solution entering the absorber would be lower than the one displayed by the density meter. So, the concentration of ammonia in that solution would be slightly higher than the one calculated from the current density readings obtained from the density meter. However, this would contribute in a very small amount to the total error in the calculated value of the concentration of ammonia in the solution.

    (c) the ionic liquid ([emim][SCN]) that was used for the experimentation is about 98% pure. The impurities present in the ionic liquid may introduce an error in the equation used to calculate the density of the pure ionic liquid (see table 3.2), thus leading to an increased prediction of the value of concentration of ammonia in ammonia + [emim][SCN] solution going into the absorber. This can be quite a large contributing factor to the error in the calculation of $w_{\mathrm{NH_3,weak}}$.

    (d) Another possible reason for the low vapor flow, and hence, low concentration of ammonia can be the fact that the generator side thermostatic bath has a lower limit on the temperature that it can attain, thus putting a restriction on the generator equilibrium temperature, and inevitably, equilibrium pressure. It is possible that a temperature higher than 95 °C is required for all of the ammonia in the solution to vaporize (see figure 2.11).

    A study made to find the reason behind the low concentration of ammonia and the results obtained from this study are reported in chapter 7 of the present work.

3. It can be seen from the obtained readings shown in table 5.5, that the equilibrium pressure of the solution corresponds to the operating temperature in the generator.

4. It is also clear that after a particular flow rate of the solution into the absorber, the generator side pressure suddenly starts to drop. This suggests that the system has a highest flow rate of the absorber it can endure without failing to attain steady state.

5. The values for the vapor flow obtained in this set of experimentation are quite low. This suggests that quite a low amount of ammonia gets vaporized in the generator, despite the high temperature at which the generator side thermostatic bath is operating (95 °C). This fact suggests that not a lot of ammonia vapor is getting absorbed into the solution. So, it

can be predicted that a large amount of the total heat transferred to the cooling water is just due to the sensible heat transfer.

6

Numerical model for the absorption process

6.1. Numerical model of the absorption process

The numerical model developed by Wang (2019) is used as a basis to build a numerical model for the present work. Block diagram of this model is given in figure 2.6 in chapter 2 of this work, where the model by Wang (2019) has been introduced.

Assumptions made while modelling the absorption process (Wang, 2019) are listed in section 2.3. Experimental readings taken by Amaris Castilla et al. (2014) are used by Wang (2019) for numerical modelling of the absorption process. These experimental readings were taken for the working pair of ammonia- $\mathrm{LiNO_3}$. Fourteen such data points with different absorber side flow rates were used. During the numerical modelling, the length of the plate heat exchanger (PHX) is divided into control volumes as per equation 6.1.

$$L_{\mathrm{cv}} = \frac{L_{\mathrm{p}}}{n_{\mathrm{cv}}} \tag{6.1}$$

Where n_{cv} represents the number of control volumes and L_{cv} represents the length of a single control volume.

6.1.1. Modelling of an individual control volume

A control volume is designed as described in section 2.3, in figure 2.5. A single control volume contains half the flow of the cooling water in a single channel, and half of the flow of the solution and the vapor in a single channel, both adjacent to a plate of the absorber. Heat and mass transfer take place across the vapor-liquid interface and only heat transfer takes place across the wall of the PHX. The heat and mass transfer is modelled for each individual control volume. The algorithm represented in figure 2.6 is the structure of the central simulation code designed for the absorption process in Matlab. All the aspects of the absorption process are modelled in separate Matlab functions. Matlab functions for the heat and mass balances, calculation of the thermodynamic properties at the vapor- liquid temperature, calculation of the interface temperature are embedded into the central Matlab code designed for a single control volume.

Input conditions to the central code represented in figure 2.6 are the operating conditions at the bottom of the heat exchanger, ie, outlet of the cooling water and the inlet of the absorbent solution and ammonia vapour. These input conditions to the first control volume include the temperature, pressure and the mass flow of the solution going into the absorber, the temperature, pressure and the mass flow of the cooling water coming out of the absorber, and the temperature, pressure and the mass flow of the vapour going into the absorber. Mass concentration of ammonia in the solution stream going into the absorber is also inputted.

Film thickness is calculated using the void fraction and the gap between the plates of the heat exchanger as per equation 6.2.

$$\delta = \frac{(1-\epsilon)L_{\mathrm{g}}}{2} \tag{6.2}$$

Void fraction is calculated as per equation 6.3.

$$\epsilon = 1 + \frac{(1-q)}{q}\left(\frac{\rho_{\mathrm{V}}}{\rho_{\mathrm{L}}}\right)^{2/3} \tag{6.3}$$

Where q is the vapor quality.

Equilibrium is assumed at the interface of the solution of [emim][SCN]+ammonia and the ammonia vapor. Matlab functions are designed to calculate the pressure, temperature and the concentration at the equilibrium according to the PTw correlation developed using NRTL model (Wang, 2019).

Heat and mass transfer equations representing the absorption + convective heat transfer process for a single control volume are determined. An initial guess at the vapor - liquid interface temperature is put into the heat and mass transfer equations, in order to satisfy the overall energy balance.The actual value of the interface temperature is calculated iteratively. That value which satisfies the heat and mass balance of the cell, is chosen to be the actual value of the temperature of the interface. In order to calculate the accurate heat transfer coefficient and the mass transfer coefficient, two Nusselt numbers are taken into account, one between the bulk liquid and the wall of the PHX ($\mathrm{Nu}_{\mathrm{L,W}}$), and the other between the bulk liquid and the liquid-vapour interface ($\mathrm{Nu}_{\mathrm{L,int}}$) (Grossman, 1983, Wang, 2019). The coefficients of these Nusselt number correlation with the Reynolds number and the Prandtl number of the bulk liquid are optimized using equation 6.4. The objective function of the optimization is the minimization of the following function.

$$F = \sqrt{\left(\left(\frac{(\frac{\dot{Q}}{A})_{\mathrm{exp}} - (\frac{\dot{Q}}{A})_{\mathrm{sim}}}{(\frac{\dot{Q}}{A})_{\mathrm{exp}}}\right)^2\right)}\sqrt{\left(\left(\frac{U_{\mathrm{exp}} - U_{\mathrm{sim}}}{U_{\mathrm{exp}}}\right)^2\right)} \tag{6.4}$$

$\frac{\dot{Q}}{A}$ is used as an indicator of the energy balance and U is used as an indicator of the heat transfer performance. A broader framework of this numerical analysis that contains the optimization process of the Nusselt numbers as well is shown in figure 6.1.

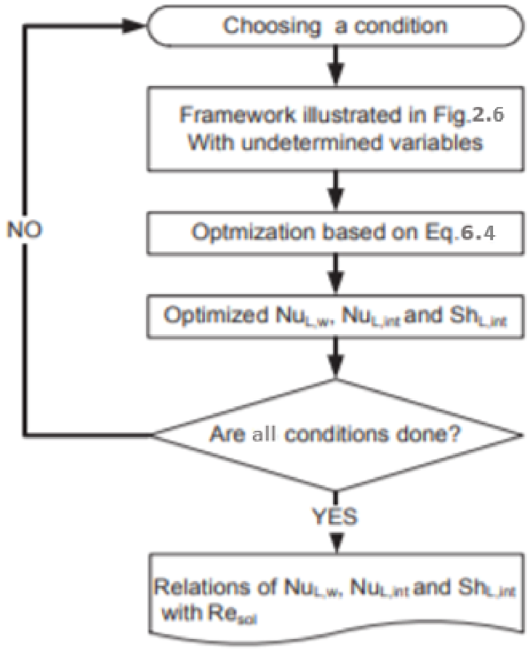

Figure 6.1: Broader framework for the numerical analysis (Wang, 2019)

The optimized correlations are in the form of equation 6.5.

$$\mathrm{Nu} = a\mathrm{Re}^{b}\mathrm{Pr}^{\frac{1}{3}} \tag{6.5}$$

In equation 6.5, a and b are the optimized coefficients. This process is repeated for each control volume of each of the fourteen experimental data points (Amaris Castilla et al., 2014), having different flow rates on the absorber side, and the values of the Nusselt number as a function of the bulk liquid Prandtl number are plotted against the values of the Reynolds numbers of the bulk liquid for each of the data points. This is done for both the Nusselt numbers- the one between the bulk liquid the wall of the PHX ($Nu_{L,W}$), and the other between the bulk liquid and the liquid-vapour interface ($Nu_{L,int}$). These plots provide the estimated empirical correlations between these Nusselt numbers, the bulk liquid Prandtl numbers and the bulk liquid Reynolds numbers for this absorption process. These correlations obtained by Wang (2019) are displayed in figure 6.2, and have also been assumed to apply for the absorption with NH_3 - [emim][SCN] working pair.

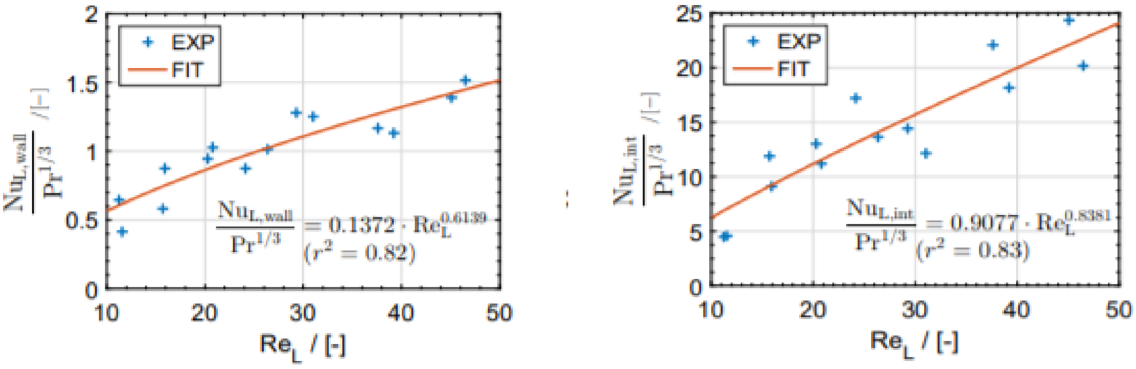

Figure 6.2: Bulk liquid-wall and bulk liquid-interface correlations (Wang, 2019)

Equations 6.6 and 6.7 show the correlations obtained by Wang (2019).

$$Nu_{L,W} = 0.1372Re^{0.6139}Pr^{\frac{1}{3}} \tag{6.6}$$

$$Nu_{L,int} = 0.9077Re^{0.8381}Pr^{\frac{1}{3}} \tag{6.7}$$

6.2. Modelling of the absorption process in the present work

The process of the numerical modelling used by Wang (2019) as described in section 6.1 is used as a basis to design a numerical model for the absorption of ammonia in ammonia + [emim][SCN] solution in the present work.

Assumptions made during the modelling of the absorption process are as follows

1. The setup operates in steady state.
2. Uniform distribution is assumed along the width of the plate of the absorber.
3. Any thermal losses in the piping, from the equipment and from the thermostatic baths are neglected.
4. Thin film assumption is made at the interface. The liquid film is thin and symmetrical with the plates.
5. Interface between vapor and the solution is assumed to be at equilibrium. Vapor liquid equilibrium modelled by Wang (2019) is used to calculate the thermodynamic properties at the interface.
6. Thermal boundary layers between the single phase and two phase regions show a smooth transition.
7. Transverse and longitudinal heat conduction at the plates of heat exchanger are neglected.
8. Considering negligible vapor pressure of [emim][SCN], it is assumed that it does not evaporate and the vapor stream is pure ammonia.
9. Ammonia already present in the solution at the inlet of the absorber is in liquid state.

In order to validate the experimental results in this work, a similar Matlab code to the one explained in section 6.1 is designed for the working pair of [emim][SCN]+ammonia. The length of the plate heat exchanger is divided into 600 control volumes. The nature of a control volume is selected as suggested by Wang (2019) (figure 2.5). This control volume consists of half the total space in each channel on either side of the wall of the PHX.

6.2.1. Modelling of an individual control volume

An individual cell or a control volume is modelled using a similar framework as displayed in figure 2.6. The input conditions are at the bottom of the heat exchanger, ie, inlet of the solution and the vapor streams into the absorber, and the outlet of the cooling water from the absorber. The input conditions used for the numerical model, as given to the first control volume at the bottom of the PHX are shown in table 6.1.

Table 6.1: Input conditions to be given to the numerical modelling

Serial Number	Input condition	Description
1	$\dot{m}_{\mathrm{abs,in}}$	Mass flow rate of the absorbent solution going into ABS
2	$P_{\mathrm{abs,in}}$	Pressure of the absorbent solution going into ABS
3	$T_{\mathrm{abs,in}}$	Temperature of the absorbent solution going into ABS
4	$w_{\mathrm{NH_3,weak}}$	Mass concentration of ammonia in the absorbent solution going into ABS
4	$\dot{m}_{\mathrm{cw,out}}$	Mass flow rate of the cooling water stream coming out of ABS
5	$P_{\mathrm{cw,out}}$	Pressure of the cooling water stream coming out of ABS
6	$T_{\mathrm{cw,out}}$	Temperature of the cooling water stream coming out of ABS
7	$\dot{m}_{\mathrm{v,in}}$	Mass flow rate of the vapor stream going into ABS
8	$P_{\mathrm{v,in}}$	Pressure of the vapor stream going into ABS
9	$T_{\mathrm{v,in}}$	Temperature of the vapor stream going into ABS

Experimental data obtained from the stage 2 ammonia - [emim]SCN] experiments (table 5.5) is used for the values of the input operating conditions.

The thermophysical properties of the cooling water, solution of [emim][SCN]+ammonia and the ammonia vapour are calculated from these input conditions. For the calculation of the values of thermophysical and the transport properties of the cooling water and the ammonia vapour Refprop (Lemmon et al., 2010) is used. For the solution, correlations of the thermophysical properties of the individual fluids as explained in chapter 3 are used. These correlations relate a solution property to the same property of the individual components of the solution of ammonia + [emim][SCN].

After the extraction of these properties, film thickness is calculated using the void fraction and the gap between the plates of the heat exchanger, as per equation 6.2. Void fraction is calculated as per equation 6.3.

A guess is made at the interface temperature and the one that satisfies the heat and mass balances of the entire cell is chosen. An iterative process is opted for this purpose. For establishing the heat and mass balance, the heat and mass transfer equations used are listed below.

1. Energy balance of the cooling water stream :

$$\dot{Q}_{\mathrm{W,cw}} + \dot{m}_{\mathrm{cw,out}} h_{\mathrm{cw,out}} - \dot{m}_{\mathrm{cw,in}} h_{\mathrm{cw,in}} = 0 \tag{6.8}$$

2. Energy balance of the solution (absorber side fluid) :

$$\dot{G}_{\mathrm{int}} \hat{h}_{\mathrm{L,NH_3}} + \dot{Q}_{\mathrm{int,abs}} - \dot{Q}_{\mathrm{abs,W}} + \dot{m}_{\mathrm{abs,in}} h_{\mathrm{abs,in}} - \dot{m}_{\mathrm{abs,out}} h_{\mathrm{abs,out}} = 0 \tag{6.9}$$

3. Energy balance of the vapor :

$$\dot{G}_{\mathrm{int}} \hat{h}_{\mathrm{v,NH_3}} + \dot{Q}_{\mathrm{v,int}} + \dot{m}_{\mathrm{v,in}} h_{\mathrm{v,in}} - \dot{m}_{\mathrm{v,out}} h_{\mathrm{v,out}} = 0 \tag{6.10}$$

4. Energy balance across the wall of the HEX :

    (a) Equation regarding the conduction of heat across the wall :

$$\dot{Q}_{\mathrm{abs,W}} = \dot{Q}_{\mathrm{W,cw}} \tag{6.11}$$

(b) Amount of energy passed from the wall to the cooling water :

$$\dot{Q}_{\mathrm{W,cw}} = \bar{\alpha}_{\mathrm{W,cw}}(T_{\mathrm{W}} - T_{\mathrm{cw,in}})A_{\mathrm{int}} \tag{6.12}$$

(c) Amount of energy passed from the solution to the wall :

$$\dot{Q}_{\mathrm{abs,W}} = \bar{\alpha}_{\mathrm{abs,W}}(T_{\mathrm{abs,in}} - T_{\mathrm{W}})A_{\mathrm{int}} \tag{6.13}$$

5. Energy balance across the vapor - liquid interface :

   (a) Energy balance across the interface :

$$\dot{G}_{\mathrm{int}}\hat{h}_{\mathrm{v,NH_3}}A_{\mathrm{int}} + \dot{Q}_{\mathrm{v,int}} = \dot{G}_{\mathrm{int}}\hat{h}_{\mathrm{L,NH_3}}A_{\mathrm{int}} + \dot{Q}_{\mathrm{int,abs}} \tag{6.14}$$

   (b) Energy into the liquid across the interface :

$$\dot{Q}_{\mathrm{int,abs}} = \bar{\alpha}_{\mathrm{int,abs}}(T_{\mathrm{int}} - T_{\mathrm{abs,in}})A_{\mathrm{int}} \tag{6.15}$$

   (c) Energy into the vapor across the interface :

$$\dot{Q}_{\mathrm{int,v}} = \bar{\alpha}_{\mathrm{int,v}}(T_{\mathrm{v,in}} - T_{\mathrm{int}})A_{\mathrm{int}} \tag{6.16}$$

6. Mass balance of the solution stream :

   (a) Mass balance in the solution stream :

$$\dot{G}_{\mathrm{int}}A_{\mathrm{int}} + \dot{m}_{\mathrm{abs,in}} - \dot{m}_{\mathrm{abs,out}} = 0 \tag{6.17}$$

   (b) Calculation of the mass flux :

$$\dot{G}_{\mathrm{int}} = M_w\bar{\beta}(c_{\mathrm{int}} - c_{\mathrm{abs}}) \tag{6.18}$$

7. Mass balance of the vapor stream :

$$\dot{G}_{\mathrm{int}}A_{\mathrm{int}} + \dot{m}_{\mathrm{v,in}} - \dot{m}_{\mathrm{v,out}} = 0 \tag{6.19}$$

8. NH_3 species balance :

$$\dot{G}_{\mathrm{int}}A_{\mathrm{int}} + \dot{m}_{\mathrm{abs,in}}w_{\mathrm{NH_3,weak}} - \dot{m}_{\mathrm{L,out}}w_{\mathrm{NH_3,strong}} = 0 \tag{6.20}$$

It is important to note here, that the solution side is denoted as 'abs', vapor side is denoted as 'v' and the cooling water side is denoted as 'cw'. It should also be noted here that the use of the inlet temperatures of the vapor and the solution ($T_{\mathrm{abs,in}}$ and $T_{\mathrm{v,in}}$) to calculate the heat duty instead of the bulk temperatures is justified, owing to the fact that the size of an individual control volume is small. Also, in the convective heat transfer region, instead of A_{int}, A_{cv} is to be used, because of the lack of the vapor - liquid interface in this region.

For the calculation of the heat duties across the wall of the heat exchanger and across the interface, Nusselt-Reynolds-Prandtl correlations estimated by Wang (2019) are used. This correlations are shown in figure 6.2. For calculating the heat transferred to the cooling water, the empirical correlation linking Nusselt - Prandtl - Reynolds numbers derived from the low Reynolds number water water experiments (equation 4.8) is used. As this correlation was derived for the convective heat transfer in a PHX between two fluids, it is assumed that the same correlation is valid for the convective heat transfer between ammonia + [emim][SCN] solution and the cooling water. Using these correlations, the calculated interface temperature, and the heat and mass transfer equations, a heat and mass balance for a single control volume is established. The output of this balance are the enthalpies of the solution and the vapor coming out of the cell, the enthalpy of the cooling water, and the pressures of the solution, cooling water and the vapor at the other end of the control volume. From these enthalpies the temperatures of the solution, vapour and the cooling water can be calculated. Similarly, mass flows at the other end of the control volume are calculated. These calculated temperatures, pressures, concentrations and mass flows are given as an input to the next control volume.

This process is performed on each of the control volumes and the temperatures, pressures, concentrations and the mass flows at the top of the plate heat exchanger are obtained.

Table 6.2 lists the outputs obtained at the top of the plate heat exchanger, ie, at the outlet of the solution and the vapor streams, and at the inlet of the cooling water stream.

Table 6.2: Outputs obtained from the numerical model

Serial Number	output obtained	Description
1	$\dot{m}_{\text{abs,out}}$	Mass flow rate of the absorbent solution coming out of ABS
2	$P_{\text{abs,out}}$	Pressure of the absorbent solution coming out of ABS
3	$T_{\text{abs,out}}$	Temperature of the absorbent solution coming out of ABS
4	$w_{\text{NH}_3\text{,strong}}$	Mass concentration of ammonia in the absorbent solution coming out of ABS
4	$\dot{m}_{\text{cw,in}}$	Mass flow rate of the cooling water stream going into ABS
5	$P_{\text{cw,in}}$	Pressure of the cooling water stream going into ABS
6	$T_{\text{cw,in}}$	Temperature of the cooling water stream going into ABS
7	$\dot{m}_{\text{v,out}}$	Mass flow rate of the vapor stream coming out of ABS
8	$P_{\text{v,out}}$	Pressure of the vapor stream coming out of ABS
9	$T_{\text{v,out}}$	Temperature of the vapor stream coming out of ABS

$w_{\text{NH}_3\text{,strong}} - w_{\text{NH}_3\text{,weak}}$, as obtained from the numerical modelling, shows how much ammonia has been absorbed into the solution stream at the top of the PHX.

These obtained results are to be compared with the experimental readings for each of the 19 data points (cases) from stage 2 ammonia - ionic liquid experiments, and the accuracy of the Nusselt- Prandtl- Reynolds correlations derived by Wang (2019) is to be estimated (equations 6.6 and 6.7). The temperature outputs obtained from this model are also an indicator of the accuracy of the convective heat transfer correlation derived from the water - water experiments (equation 4.8) and used in this model for the convective heat transfer between the cooling water and the solution.

6.3. Results of the numerical analysis

6.3.1. End results

The results obtained for each of the 19 data points from the numerical modelling are shown in table 6.3. These results include the outlet temperature of ammonia + [emim][SCN] solution, outlet concentration of ammonia in the absorbent solution stream, outlet pressure of the solution stream, and the temperature of the cooling water being sent into the absorber.

Table 6.3: Results of the numerical modelling for stage 2 ammonia+ionic liquid experiments

Case	$T_{\text{abs,out}}$ (°C)	$w_{\text{NH}_3\text{,strong}}$ -	$P_{\text{abs,out}}$ (KPa)	$T_{\text{cw,in}}$ (°C)	ΔT_{abs} (°C)	ΔT_{cw} (°C)
1	44.51	0.0252	241.3	44.39	10.43	3.19
2	-	-	-	-	-	-
3	-	-	-	-	-	-
4	-	-	-	-	-	-
5	45.51	0.0237	388.6	44.99	10.00	4.83
6	44.86	0.0237	367.6	44.66	10.99	2.77
7	44.81	0.0241	296.7	44.64	10.66	2.59
8	44.81	0.0242	286.3	44.64	10.66	2.59
9	44.84	0.0243	263.2	44.52	10.76	3.48
10	44.77	0.0246	225.5	44.52	10.74	3.28
11	44.91	0.0240	219.6	44.67	10.61	3.05
12	44.86	0.0243	267.8	44.28	10.87	4.46
13	45.20	0.0235	265.6	44.65	10.52	4.08
14	45.42	0.0230	345.3	44.35	10.65	5.43
15	44.78	0.0246	332.7	44.12	11.01	4.74
16	-	-	-	-	-	-
17	45.93	0.0228	237.3	44.59	10.11	5.83
18	45.66	0.0228	342.4	44.63	10.38	5.23
19	45.66	0.0228	338.3	44.63	10.35	5.20

It seemed that steady state had not been attained for data points 2,3,4 and 16, when the experimental readings were taken. So, the results could not be obtained numerically for these data points, as the absorber pressure recorded is too high for the recorded concentration and the temperature. So, these data points cannot be taken into account for the study of the absorption process.

Temperature and concentration profiles obtained for some of the data points are shown below. Figures 6.3 and 6.4 show the temperature and the concentration profiles obtained as results of the numerical modelling, for data case 8 (from tables 5.5 and 6.3).

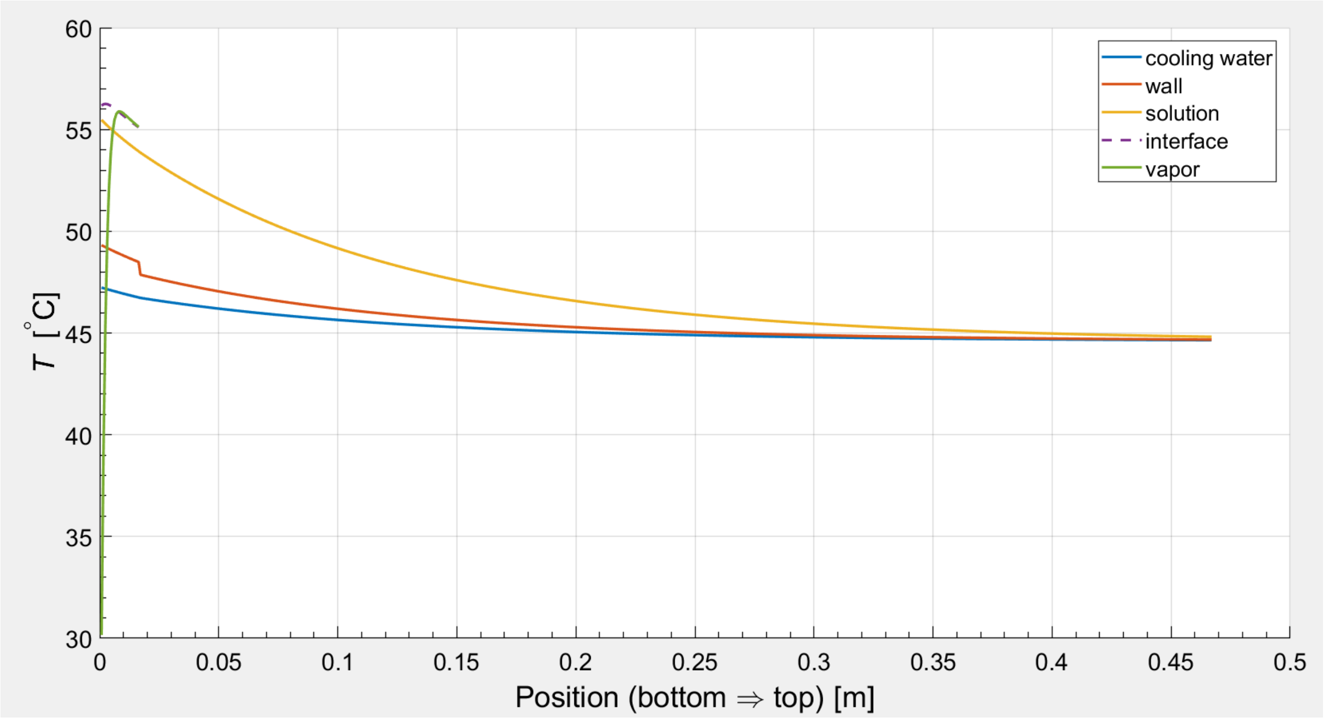

Figure 6.3: Temperature profile obtained for case 8

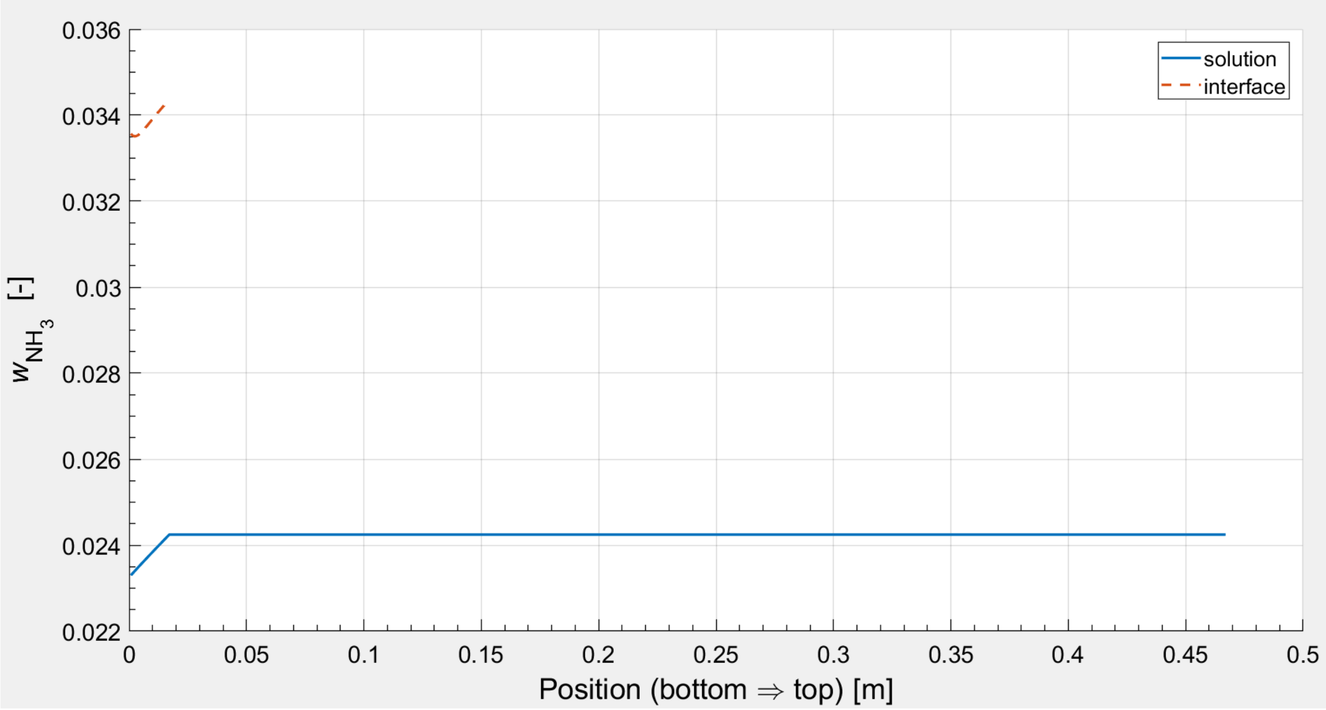

Figure 6.4: concentration profile obtained for case 8

Figures 6.5 and 6.6 show the temperature and the concentration profiles obtained as the results of the numerical modelling, for data case 10 (from tables 5.5 and 6.3).

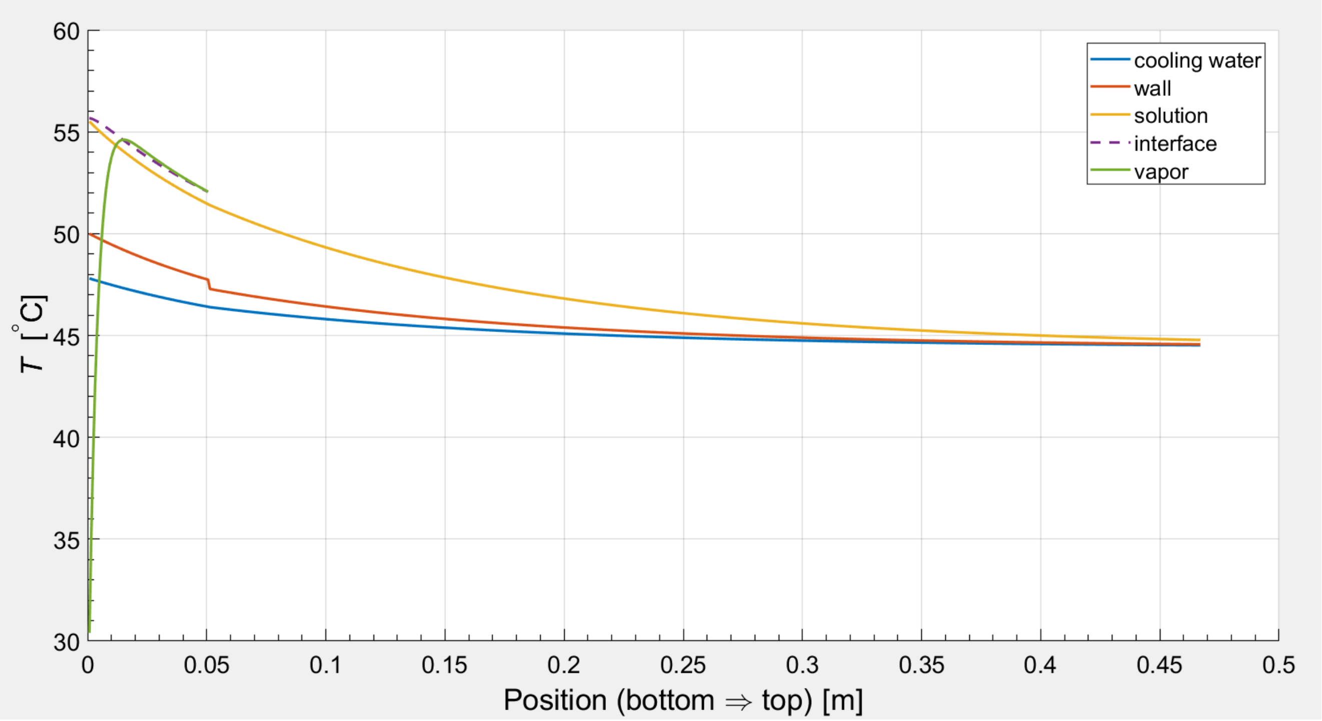

Figure 6.5: Temperature profile obtained for case 10

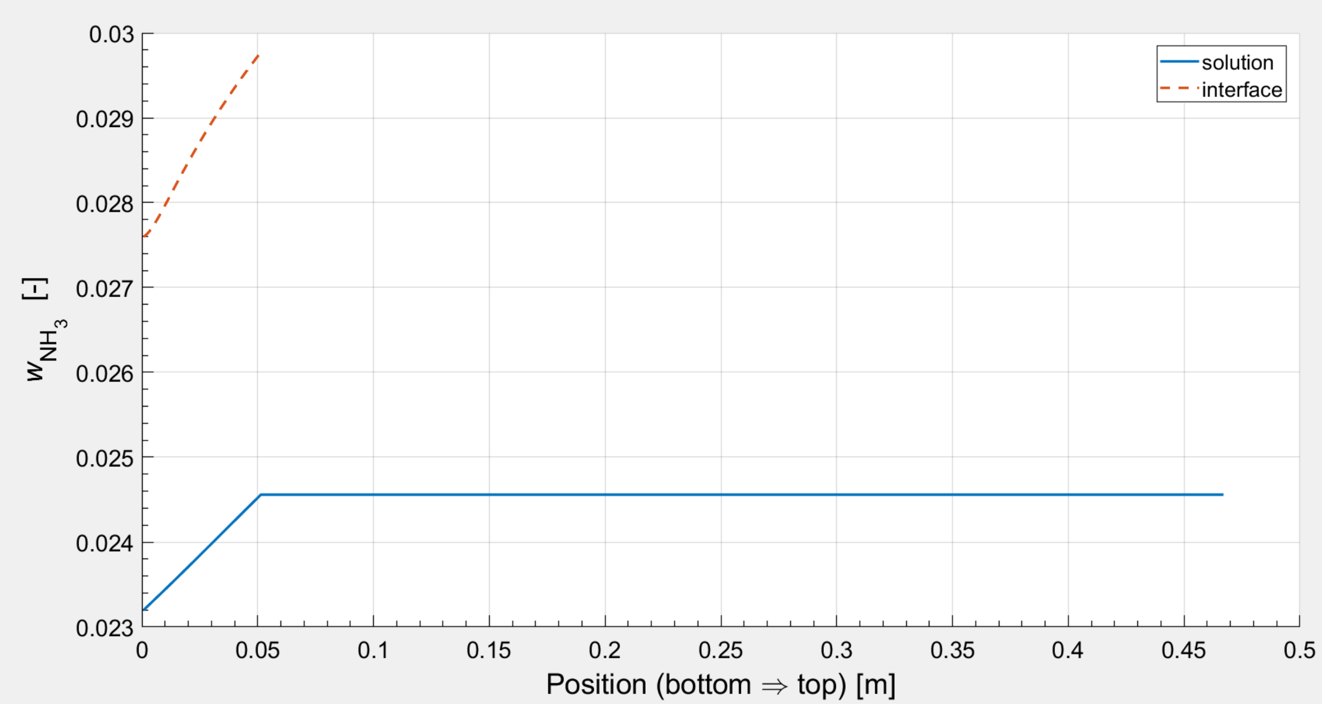

Figure 6.6: concentration profile obtained for case 10

Figures 6.7 and 6.8 show the temperature and the concentration profiles obtained as the results of the numerical modelling, for data case 17 (from tables 5.5 and 6.3).

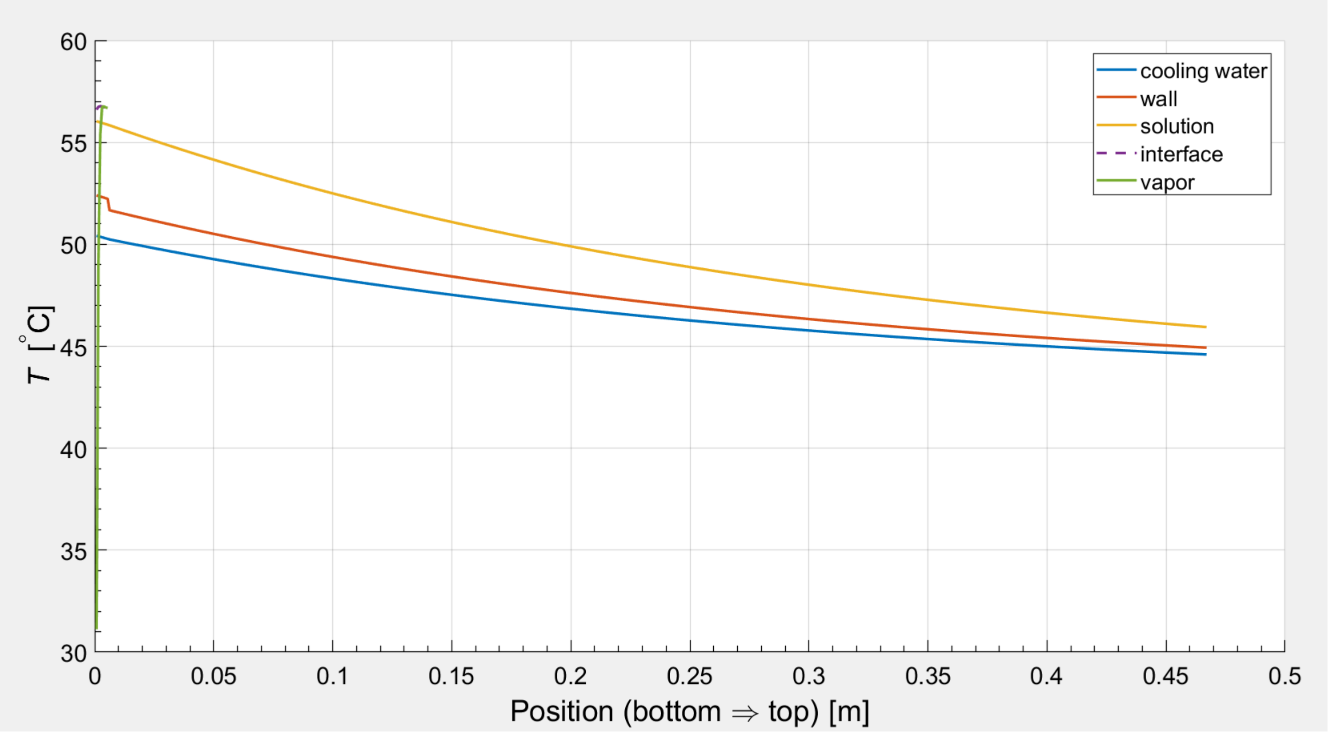

Figure 6.7: Temperature profile obtained for case 17

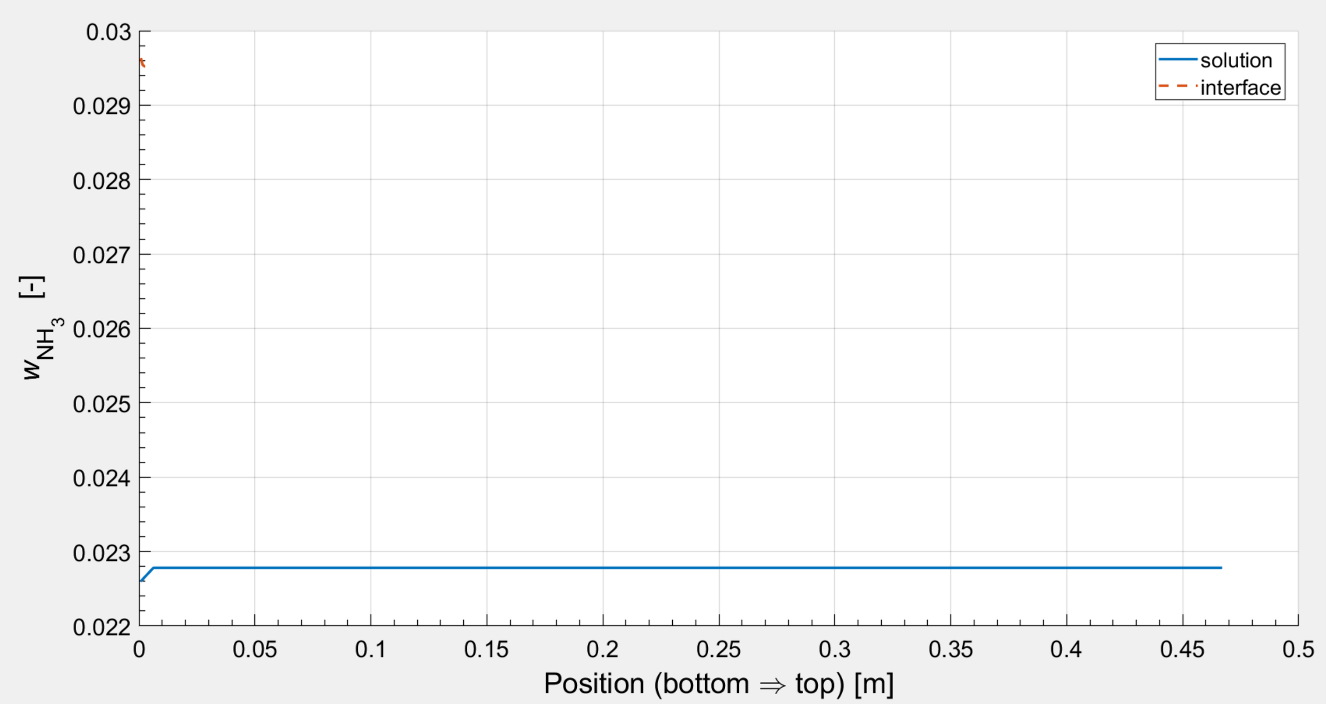

Figure 6.8: concentration profile obtained for case 17

Temperature and concentration profiles for all the data points are not displayed in this chapter. The resultant profiles for all of the experimental data points can be found in Appendix A.

6.3.2. Values of the heat and mass transfer parameters

Values of several heat and mass transfer parameters were numerically calculated both during the absorption region and during the convective heat transfer region of the process for all the data points for reference. Table 6.4 displays the values of the heat and mass transfer parameters for the absorption region. These values were calculated at about half the length of the absorption region.

Table 6.4: Values of the heat and mass transfer parameters for the middle of the absorption region

Case	Re	Pr	Sc	Sh	$Nu_{L,W}$	$\bar{\alpha}_{L,W}$	$Nu_{L,int}$	$\bar{\alpha}_{L,int}$	$\bar{\beta}$
	(-)	(-)	(-)	(-)	(-)	(W/m^2-K)	(-)	(W/m^2-K)	(m/s)
1	6.7	36.0	439.7	88.8	1.4	365.9	1.7	443.4	$4.2E^{-5}$
2	-	-	-	-	-	-	-	-	-
3	-	-	-	-	-	-	-	-	-
4	-	-	-	-	-	-	-	-	-
5	11.2	35.6	423.4	129.7	1.9	480.1	2.6	540.6	$6.3E^{-5}$
6	11.0	35.8	426.1	128.3	1.9	484.6	2.6	658.4	$6.4E^{-5}$
7	10.5	35.8	428.9	123.9	1.8	471.1	2.5	632.5	$6.1E^{-5}$
8	10.5	35.9	428.7	124.9	1.9	473.1	2.5	637.0	$6.1E^{-5}$
9	13.8	35.9	431.3	153.5	2.2	561.8	3.2	803.2	$7.7E^{-5}$
10	12.6	36.6	445.5	144.6	2.1	543.3	3.0	761.3	$7.3E^{-5}$
11	12.3	36.5	441.5	140.8	2.1	521.3	2.9	725.6	$6.9E^{-5}$
12	17.3	35.8	428.9	182.3	2.5	648.8	3.8	976.5	$9.4E^{-5}$
13	17.3	35.9	427.2	181.5	2.5	630.0	3.8	948.0	$9.2E^{-5}$
14	22.6	36.0	425.9	222.4	3.0	736.9	4.8	1179.0	$1.1E^{-4}$
15	18.4	35.4	421.2	190.5	2.6	673.6	4.0	1028.0	$9.9E^{-5}$
16	-	-	-	-	-	-	-	-	-
17	25.9	36.1	428.2	247.1	3.3	797.7	5.4	1316.7	$1.2E^{-4}$
18	22.5	36.1	427.6	221.6	3.0	732.0	4.8	1173.0	$1.1E^{-4}$
19	22.5	36.1	428.0	221.5	3.0	731.8	4.8	1169.0	$1.1E^{-4}$

Table 6.5 displays the values of various heat and mass transfer parameters during the convective heat transfer region for all the data points. These values are numerically calculated at about half the length of the absorber in the convective heat transfer region.

Table 6.5: Values of the heat and mass transfer parameters for the middle of the convective heat transfer region

Case	Re	Pr	Sc	$Nu_{L,W}$	$\bar{\alpha}_{L,W}$
	(-)	(-)	(-)	(-)	(W/m^2-K)
1	5.8	40.6	545.8	3.1	189.8
2	-	-	-	-	-
3	-	-	-	-	-
4	-	-	-	-	-
5	9.6	40.6	526.7	4.4	266.5
6	9.2	41.9	556.1	4.3	262.0
7	8.9	41.5	552.3	4.2	254.0
8	8.8	41.3	550.7	4.2	255.5
9	11.9	40.9	541.6	5.1	309.3
10	11.1	40.9	545.4	4.9	295.4
11	10.6	41.5	551.9	4.8	287.1
12	15.0	40.5	531.9	6.0	361.6
13	14.8	41.2	537.6	6.1	359.1
14	19.5	41.0	528.0	7.2	356.8
15	15.9	40.0	524.0	6.2	372.2
16	-	-	-	-	-
17	22.7	40.7	519.5	8.0	478.2
18	19.5	41.1	528.2	7.2	432.3
19	19.5	41.2	528.6	7.2	432.4

6.3.3. Observations made from the results of the numerical analysis

After the execution of the central Matlab code, following facts come to the notice :

1. Reflection on the temperature profiles :
    (a) The temperature profiles obtained from the numerical modelling in the present work follow the trend of the temperature curves as predicted by Wang (2019) (See Figure 27, Appendix A).
    (b) It can be seen that, as predicted, only a small amount of the total heat gained by the cooling water was because of the absorption of ammonia in ammonia + [emim][SCN] solution, for most of the experimental data points. This can be seen from the short temperature curves of the interface (dotted blue) and the vapour (green).
    (c) These short temperature curves represent the length of the absorber (PHX) from the bottom, upto which the absorption of ammonia into the solution took place. It can be seen that, owing to a very low amount of ammonia vapor flow in most of the cases, all the gas gets absorbed within a small distance from the bottom of PHX. The maximum distance to which the absorption takes place is upto 10.5% of the length of the PHX starting from the bottom.
    (d) Very large amount of the total heat transferred was just due to sensible heat transfer from the solution to the cooling water. This phenomenon can be observed from the solution curve (yellow), the wall curve (orange), and the cooling water curve (blue), after the absorption range, ie, for the remaining length of the PHX after the absorption ends.
    (e) From the dip in the curve of the wall temperature (orange), at the end of the absorption zone, and from the heat and mass parameters listed in tables 6.4 and 6.5, it is clear that the heat transfer coefficient between the solution and the wall of the PHX ($\bar{\alpha}_{\mathrm{L,W}}$) for the absorption is higher than that for the convective heat transfer. This, in turn, means that the resistance to the heat transfer is lesser during absorption than during the convective heat transfer. This, indeed corroborates the fact that the numerical model takes the effect of the mass transfer on the overall energy balance during the absorption process into account.
    (f) It can be seen from the temperature profiles obtained, that for lower flow rates of the solution, more heat is transferred because of the absorption of ammonia in ammonia + [emim][SCN] solution (eg, case 1, 10, 11 etc.) as compared to that transferred for higher flow rates (eg. case 15, 17 etc.). This observation follows from the fact, that the amount of vapor flow for lower flow rates is higher than that for the higher flow rates, as recorded from the stage 2 experiments.

    The remaining temperature profiles obtained as a result of this central Matlab code for each of the cases are displayed in the appendix A of this work.

2. Reflection on the concentration profiles :
    (a) Owing to a low vapor flow, the concentration of ammonia in ammonia + [emim][SCN] solution increases very slightly. As can be seen from table 6.3, the mass concentration of ammonia in the solution that comes out of the absorber ($w_{\mathrm{NH_3,strong}}$) is very slightly higher than the mass concentration of ammonia in the solution going into the absorber, reported in table 5.5 ($w_{\mathrm{NH_3,weak}}$). Also, the values of the mass transfer coefficients ($\bar{\beta}$) reported in table 6.4 are quite low (Wang, 2019), owing to a low vapor flow. The trend of the concentration profiles obtained is similar to that predicted by Wang (2019) (see figure 28, Appendix A).

    The remaining concentration profiles obtained as a result of this central Matlab code for each of the cases are displayed in the appendix A of this work.

3. Pressure of the solution coming out of the absorber ($P_{\mathrm{abs,out}}$), is certainly lower than the pressure at which the solution enters the absorber ($P_{\mathrm{abs,in}}$). This fact confirms that there is some pressure drop in the absorber, although it is a small value. Also, the value of ($P_{\mathrm{abs,out}}$) as calculated numerically (see table 6.3) comes close to that recorded experimentally (see table 5.5).

These results obtained are to be compared with the experimental values of the parameters, in order to validate the numerical model used.

6.4. Validation of the numerical model and comparison

For the validation of the numerical model of the absorption process, the results obtained from the model for each of the 19 data points obtained (as shown in table 6.3), are compared with the experimental data.

The temperature difference between the inlet and outlet temperatures of the solution and the cooling water is used as a parameter for the comparison between the experimental and numerical results. The deviation of the values obtained from the model from the experimental ones, is an indicator of the accuracy of the Nusselt-Prandtl-Reynolds correlations used in this work. Table 6.6 displays the values of ΔT_{abs} and ΔT_{cw} obtained from the numerical model, the experimental values of the parameters and the deviation of the calculated results from the experimental results.

Table 6.6: Comparison of the numerical results with the experimental results

Case	ΔT_{abs} (°C)		Deviation (%)	ΔT_{cw} (°C)		Deviation (%)
	Experimental	Numerical		Experimental	Numerical	
1	10.06	10.43	-3.68	2.72	3.19	-16.92
2	10.60	-	-	4.59	-	-
3	10.55	-	-	4.90	-	-
4	10.44	-	-	5.00	-	-
5	10.66	10.00	6.22	5.01	4.83	3.54
6	10.89	10.99	-0.92	2.43	2.77	-14.02
7	10.42	10.66	-2.30	2.22	2.59	-16.35
8	10.41	10.66	-2.34	2.22	2.59	-16.50
9	10.58	10.76	-1.72	3.00	3.48	-15.80
10	10.49	10.74	-2.43	2.81	3.28	-16.88
11	10.48	10.61	-1.18	2.73	3.05	-11.89
12	10.57	10.87	-2.90	3.75	4.46	-18.71
13	10.56	10.52	0.34	3.74	4.08	-9.10
14	10.57	10.65	-0.80	4.78	5.43	-13.66
15	10.61	11.01	-3.79	3.85	4.74	-22.90
16	10.26	-	-	5.5	-	-
17	10.22	10.11	1.11	5.46	5.83	-6.80
18	10.56	10.38	1.70	4.89	5.23	-6.91
19	10.53	10.35	1.69	4.89	5.20	-6.99
Mean	-	-	-0.73	-	-	-12.65

From the comparison of the data in table 6.6, the following facts can be reflected.

1. The values of ΔT_{abs} calculated numerically with the use of the model are in a reasonable accordance with the experimental values obtained (with an average error of -0.73%). Also, since the temperature profiles obtained in the present work follow the trend of the temperature curves as predicted by Wang (2019) (See Figure 27, Appendix A), it can be said that the empirical correlations governing the absorption process derived by Wang (2019) (equations 6.6 and 6.7) work satisfactorily for the present cases of absorption, where the solution is subcooled before entering the absorber. Also, considering the fact that most of the heat transfer is because of the convection, it follows that the Nusselt- Prandtl- Reynolds correlation governing the convective heat transfer derived from the water - water experiments for low Reynolds numbers in the present work (equation 4.8), functions satisfactorily for this absorption process.

2. The values of ΔT_{cw} calculated numerically with the use of the model are somewhat in accordance with the values recorded experimentally, with an average error margin of 12.65%. This confirms the fact that there are indeed heat losses in the system.

3. It is clear, that it is crucial for the correct balances of the heat and mass transfer in this absorption process, that the thermodynamic properties of ammonia + [emim][SCN] solution calculated using the NRTL model, are correct. The close resemblance between the experimental and the numerically calculated values of ΔT_{abs}, is a further validation that the NRTL model works reasonably well for this absorption process. It follows, that, the NRTL coefficients suggested by Wang (2019) for the working pair of ammonia + [emim][SCN] (table 3.2), work well for this absorption process.

6.5. Energy balance of the experimental results

Aside from the actual modelling of the absorption process, a separate Matlab code is designed, wherein the outlet temperature of ammonia + [emim][SCN] solution is estimated making use of a simple energy balance across the absorber. Thermodynamic properties of the solution are calculated by establishing a vapor - liquid equilibrium using the NRTL model. For the NRTL model, NRTL coefficients suggested by Wang (2019) for the working pair of ammonia + [emim][SCN] (table 3.3) are used. The results of this Matlab code are compared with the experimental ones.

It is of crucial importance here to note that this Matlab code does not follow an iterative procedure, so the absorber is not divided into control volumes in this case. This code simply establishes an energy balance across the absorber; using the Equation of State (EOS) method to calculate the total enthalpy of the solution.

6.5.1. Functioning of the Matlab code

The experimental data obtained from stage 2 ammonia + ionic liquid experiments are used in this case as well.

The heat duty of the absorber is calculated from the cooling water properties as per equation 6.21.

$$\dot{Q}_{\text{abs}} = \dot{m}_{\text{cw}} c_{p,\text{cw}} \Delta T_{\text{cw}} \tag{6.21}$$

The thermodynamic properties of the cooling water needed to calculate the heat duty, such as the specific heat capacity are calculated at the average cooling water temperature as per equation 6.22.

$$T_{\text{cw}} = \frac{T_{\text{cw,in}} + T_{\text{cw,out}}}{2} \tag{6.22}$$

In the Matlab code, input values, such as available temperatures, pressures, concentrations and mass flows at the bottom of the plate heat exchanger as obtained from the experimental data are provided. Concentration of ammonia in [emim][SCN] + ammonia solution going into the absorber and coming out of the absorber are calculated using the species balance for ammonia across the absorber (equation 4.11, 4.12). Thermophysical and transport properties of [emim][SCN] + ammonia solution, such as viscosity, density and the specific heat are calculated the same way as for the numerical model. Detailed explanation of how these properties are calculated for the solution is given in chapter 3. Refprop (Lemmon et al., 2010) is used to obtain the thermophysical properties of pure ammonia, and the cooling water. Enthalpies of the cooling water and the vapour are also calculated using Refprop (Lemmon et al., 2010). Similar to the numerical model, this heat balance code contains separate Matlab functions for calculating the thermodynamic properties of the solution by establishing the vapor - liquid equilibrium using the NRTL coefficients suggested by Wang (2019).

Separate Matlab functions are also created to calculate total enthalpies at various stages of [emim][SCN]+ammonia solution. It is important to note here, that in this work, the excess enthalpy of the solution is considered to be negligible, and so is not included to calculate the total solution enthalpy. Using these calculated solution enthalpies, enthalpies of the cooling water and the vapour, and the heat duty calculated as shown in equation 6.21, an overall energy balance is established as per equation 6.23.

$$h_{\text{abs,in}} \dot{m}_{\text{abs,in}} + h_{\text{v,in}} \dot{m}_{\text{v,in}} - (\dot{Q}_{\text{abs}} + \dot{Q}_{\text{losses}}) = h_{\text{abs,out}} \dot{m}_{\text{abs,out}} \tag{6.23}$$

Wherein $\dot{Q}_{\text{losses}}$ is taken as the deviation in the energy balance obtained from the numerical model for each of the data points. The result of this code is the enthalpy of the solution outlet at the top of the plate heat exchanger, from which it's temperature can be estimated.

The results obtained from this code are tallied with the experimental ones. The temperature difference between the inlet and outlet temperatures of the solution is used as a parameter for the comparison between the experimental results and the results of the energy balance here, too. Table 6.7 shows the experimental values of the outlet temperature of the solution, calculated values for the outlet temperature of the solution from the heat balance as mentioned above, the temperature difference of the solution in both the cases, and the deviation of the calculated values from those obtained by the experimentation.

Table 6.7: Comparison between experimental and calculated temperature values of the solution

Case	$T_{\text{abs,out}}$ (°C)		ΔT_{abs} (°C)		Deviation (%)
	Experimental	Calculated	Experimental	Calculated	
1	44.8	44.53	10.06	10.40	-3.39
2	44.8	-	10.60	-	-
3	44.8	-	10.55	-	-
4	44.8	-	10.44	-	-
5	44.8	44.88	10.66	10.62	0.35
6	44.9	44.89	10.89	10.96	-0.63
7	45.0	44.74	10.42	10.73	-2.91
8	45.0	44.74	10.41	10.72	-2.94
9	45.0	44.75	10.58	10.85	-2.55
10	45.0	44.64	10.49	10.87	-3.58
11	45.0	44.85	10.48	10.66	-1.67
12	45.1	44.72	10.57	11.01	-4.17
13	45.1	45.01	10.56	10.71	-1.45
14	45.0	45.47	10.57	10.60	-0.30
15	45.1	44.70	10.61	11.09	-4.46
16	45.8	-	10.26	-	-
17	45.8	46.00	10.22	10.04	1.84
18	45.4	45.75	10.56	10.28	2.62
19	45.4	45.71	10.53	10.29	2.25
Mean	-	-	-	-	-1.39

It should be noted here, that the deviation for the data points 2,3,4 and 16 could not be obtained, as the numerical results are not available for these data points.

It can be seen from the values displayed in the table 6.7, that the values of ΔT_{abs} calculated by the energy balance for the data points are in accordance with the ones that are recorded from the stage 2 experiments, when the energy losses predicted by the numerical model for each of the data points are included in the energy balance.

Limitations of this energy balance code are as listed below :

1. While making use of this energy balance, it should be noted that the excess enthalpy of ammonia + [emim][SCN] solution was neglected while calculating the heat balance. Including this excess enthalpy while calculating total solution enthalpy would impact the overall energy balance, thus bringing the calculated values of $T_{\text{abs,out}}$ closer to the reality.

2. Like the numerical model, this energy balance also assumes that the ammonia already present in the solution going into the absorber is in liquid state. So, it does not account for the fact that the solution is flashed in an expansion valve before going into the absorber. This flashing of the solution ensures that there is ammonia both in vapor and in liquid states in the solution going into the absorber. Since this is not included in the energy balance, it might have contributed to the slight imbalance in the overall energy balance.

So, this Matlab code can be used to get an estimate of the values of the outlet temperature of the solution, but using the numerical model yields more accurate values of the solution outlet temperature.

7

Viscosity check

The viscosity check experiments were performed at the experimental setup at TU Delft to determine the viscosity of the solution of [emim][SCN] + ammonia, as explained in section 4.5. The experimental values of the viscosity of the solution were compared with those predicted by Wang (2019) with a logarithmic correlation (equation 3.4).

It was observed during the experimental data of stage 2 experiments, and also during the viscosity check, that the value of w_{weak} calculated based on the reading of the density meter placed before the absorber in the setup was very low (about 2.50%) even though about 6.10% of ammonia was filled initially into the system. It was known that [emim][SCN] used in the system had impurities. So, a decision was made to derive a correlation that links the density of this [emim][SCN] with its temperature, in order to calculate the correct value of w_{weak}, and indeed, to estimate experimentally the accurate value for the viscosity of the solution.

7.1. Measurement of density

Two samples of the [emim][SCN] were used in order to derive the density correlation. One of the samples was taken from the used [emim][SCN] taken out of the experimental setup after stage 1 experiments, whereas the second sample was taken from a can of fresh [emim][SCN] as it was filled into the system before stage 2 experiments were performed.

Figure 7.1 shows these two samples.

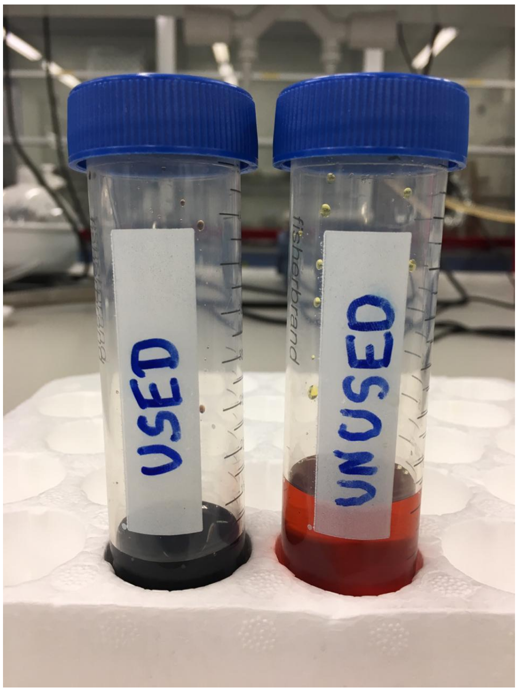

Figure 7.1: The samples of [emim][SCN] used

7.1.1. Procedure

Following procedure was followed :

1. Each of the samples was placed into the density meter.
2. Temperature of the sample was set for the average temperature of the solution as measured during each of the 5 experimental data points (see table 4.8).
3. A density meter at the chemical laboratory in the TU Delft was used to measure the density of the samples. The value of the density as given by the density meter for each of the temperatures was recorded.
4. A graph of the density values versus the temperature values is plotted in Excel, and a correlation is obtained for each of the samples.

Table 7.1 displays the average temperatures and the density readings obtained for each of the two samples of [emim][SCN].

Table 7.1: Density values for [emim][SCN], wherein, sample 1 = unused sample; sample 2 = used sample

[emim][SCN]			
Case	$T_{\text{abs,avg}}$ (°C)	ρ_{IL} (kg/m^3)	
		Sample 1	Sample 2
1	29.84	1134.42	1130.72
2	35.59	1130.90	1127.23
3	45.44	1124.91	1121.29
4	50.08	1122.11	1118.51
5	57.20	1117.84	1114.28

Figures 7.2 and 7.3 display these correlations as obtained for each of the samples.

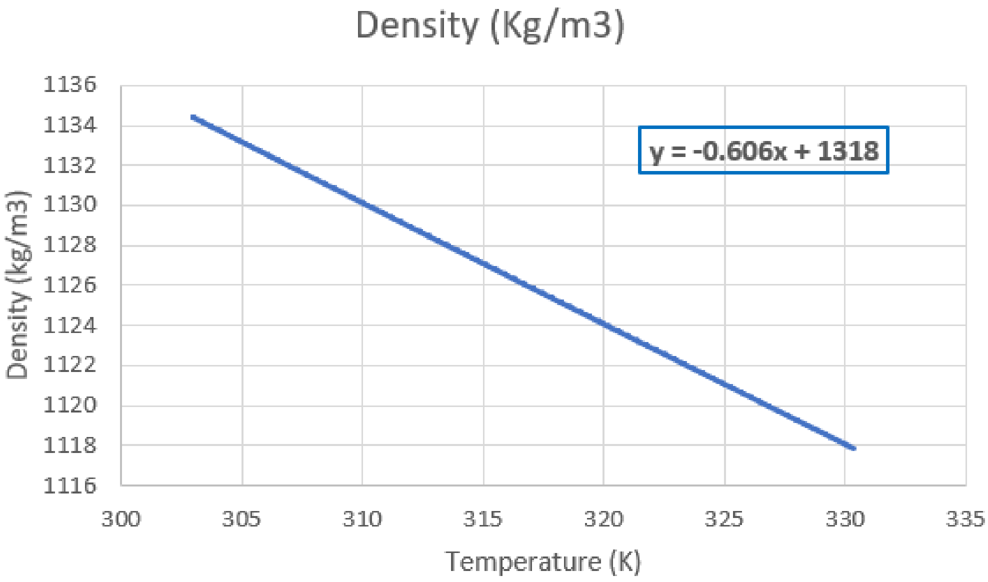

Figure 7.2: Density correlation obtained for sample 1 (unused [emim][SCN])

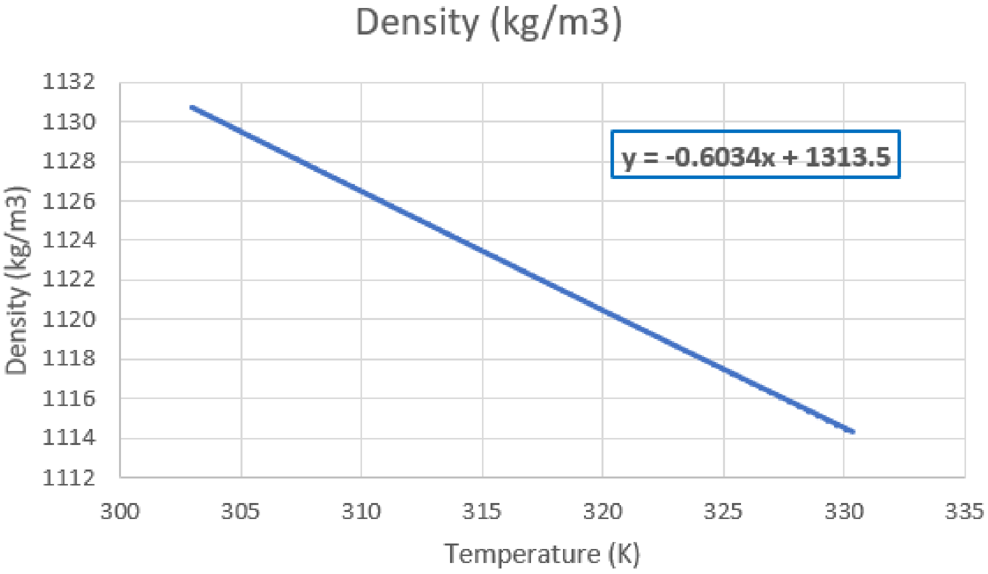

Figure 7.3: Density correlation obtained for sample 2 (used [emim][SCN])

It can be seen from figures 7.2 and 7.3, that the correlation of the density and the temperature for an impure [emim][SCN] is indeed different from the one for the pure [emim][SCN]. These obtained correlations for each of the sample are listed in equations 7.1 and 7.2.

$$\rho_{\mathrm{IL}} = 1318 - 0.606T \tag{7.1}$$

$$\rho_{\mathrm{IL}} = 1313.5 - 0.6034T \tag{7.2}$$

Where T is in Kelvin.

The correlation obtained for sample 2 (equation 7.2) was used to analyze the results of the viscosity check, keeping in mind that stage 2 experiments were performed before the viscosity check, and so the ionic liquid was reused in the viscosity check experiments.

7.2. Viscosity analysis

For this analysis, 5 experimental data points were taken (see table 4.8). The mass concentration of ammonia in ammonia+[emim][SCN] solution, during each of these five experimental data points, as determined from the density of the solution displayed by the density meter in the setup, is displayed in table 7.2. In order to calculate this concentration, the derived equation for sample 2 (equation 7.2) was used to calculate the density of [emim][SCN]. Also, the thermophysical and transport properties of ammonia+[emim][SCN] solution used to calculate the experimental values of the solution viscosity are shown in table 7.2.

Table 7.2: Properties of ammonia+[emim][SCN] solution during the viscosity check

Case	$T_{\mathrm{abs,avg}}$ °C	ρ_{sol} (kg/m^3)	w_{weak} (-)	$c_{p,\mathrm{sol}}$ (J/kg-K)	λ_{sol} (W/m-K)
1	29.84	1094.5	0.0617	1853.3	0.2261
2	35.59	1092.2	0.0540	1849.2	0.2233
3	45.44	1088.4	0.0506	1874.2	0.2211
4	50.08	1085.2	0.0522	1896.9	0.2207
5	57.20	1082.5	0.0525	1925.9	0.2198

First five minutes of each of the five data cases are displayed in figures 33 to 37 in Appendix A.

7.3. Results for the viscosity check

Using the values of the thermophysical properties as described in table 7.2, along with equation 4.9, experimental values of the solution viscosities were calculated for each of the five data points. These values of the experimental viscosity of ammonia + [emim][SCN] solution obtained from the convective heat transfer experiments and those predicted by the logarithmic viscosity relation (Wang, 2019) (equation 3.4) for the same operating conditions are shown in table 7.3. Also, the viscosity values as predicted if a linear correlation (equation 4.10) is used, are also displayed for comparison purposes.

Table 7.3: Comparison of the values of the viscosity of [emim][SCN]+ammonia solution

Case	Experimental (Pa-s)	Logarithmic correlation (Pa-s)	Linear correlation (Pa-s)
1	0.0041	0.0027	0.0190
2	0.0044	0.0028	0.0161
3	0.0034	0.0025	0.0124
4	0.0069	0.0022	0.0110
5	0.0086	0.0019	0.0094

It is important to note that during the last two experimental data points, the solution flow was varying quite a lot, thus the system was not stabilized. As a result, the average viscosity values calculated for each of these two individual data points are inaccurate, and hence cannot be considered for the analysis.

Table 7.4 shows the deviation of the values of the viscosity calculated both by the logarithmic correlation and with the linear correlation with the experimental values, for the first three experimental data points.

Table 7.4: Deviation of the values of the viscosity of [emim][SCN]+ammonia solution

Case	Deviation of the logarithmic correlation (%)	Deviation of the linear correlation
1	-33.06	368.03
2	-35.42	267.82
3	-27.68	260.85
Mean	-32.05	298.9

7.4. Validation of the logarithmic correlation

Following observations were made from the results of these experiments :

1. It can be seen from the obtained values shown in tables 7.3 and 7.4 for the first three data points, that for the given sample of [emim][SCN], the logarithmic correlation underestimates the value of the solution viscosity by a small and acceptable margin (about 32.05%), as predicted by Wang (2019).

2. The linear correlation for the viscosity overestimates the viscosity of the given sample of the ionic liquid by a large margin.

It is concluded that the logarithmic correlation gives the values of the solution viscosity much closer to the real values, as compared to the values given by the linear correlation. So, overall, it can be said that the logarithmic correlation linking the viscosity of ammonia + [emim][SCN] solution to the mass fractions of the individual fluids, as suggested by Wang (2019), and Gao and Wagner (2016) has been confirmed to predict the viscosity values with on an average 32.05% accuracy.

This experimental study done in order to check the viscosity of ammonia + [emim][SCN] solution justifies the use of the logarithmic correlation to calculate the solution viscosity (equation 3.4) for this and the future studies involving the use of [emim][SCN] as an absorbent.

8

Conclusions

Following facts can be concluded after studying the process of absorption both experimentally and numerically.

1. NRTL coefficients suggested by Wang (2019) for the working pair of ammonia - [emim][SCN] lead to the calculation of the correct values of the VLE of ammonia + [emim][SCN] solution. It can be concluded from comparing the VLE established by Wang (2019) to the experimental data by Yokozeki and Shiflett (2007) that the equilibrium properties calculated are in a reasonable accordance with the experimental data. Thus, it can be said that in this work, the VLE established by Wang (2019) for the working pair of ammonia +[emim][SCN], is validated with an acceptable value of deviation.

2. In this work, an attempt was made to predict the behaviour of the viscosity of ammonia + [emim][SCN] solution with changes in the operating conditions in the process of absorption. This study concludes following facts:

   (a) A logarithmic correlation linking the solution viscosity with the individual viscosities (Wang, 2019, Gao and Wagner, 2016) underestimates the value of the solution viscosity by about 32.05%, as predicted by Wang (2019).

   (b) A linear correlation linking the solution viscosity with the individual viscosities overestimates the value of the solution viscosity by a very large margin (about 298.9%).

   From these facts, it is indeed clear that the logarithmic correlation for the solution viscosity (equation 3.4) works satisfactorily for ammonia + [emim][SCN] solution, thus justifying its use in the present and potential future works. It underestimates the real values by a small margin, nevertheless, it gives much more accurate values of the solution viscosity than the linear correlation (equation 4.10).

3. When the results of the numerical model of the absorption process are compared with the experimental results (table 6.6), following conclusions can be drawn.

   (a) The results obtained from the water - water experiments performed at the setup at the Delft University of Technology yield an empirical correlation for the convective heat transfer coefficient.

   This correlation for the low range of Reynolds number (equation 4.8), was used in the numerical model, which yielded reasonable end results from the model, with a moderate error margin owing to the heat losses, and uncertainty in the value of $w_{NH_3,weak}$. Considering the fact that a large amount of heat was transferred because of the convective heat transfer to the cooling water, it is clear that this empirical correlation obtained from the water - water experiments for the low range of Reynolds number (equation 4.8) is acceptable, thus leading to the numerical results close to the reality.

   It also indicates that the experimental setup is working correctly.

(b) Not much can be said regarding the exact accuracy of the empirical heat transfer correlations derived by Wang (2019) for the absorption process, as a very small amount of heat was transferred due to the absorption phenomenon in stage 2 experiments. But based on the values of $P_{\text{abs,out}}$, $T_{\text{abs,out}}$ and $w_{\text{NH}_3\text{,strong}}$ at the end of the absorption zone, it can be estimated that these equations governing the absorption process (equations 6.6 and 6.7) seem to work satisfactorily for the absorption process, for those cases where the solution enters the absorber in the subcooled state.

(c) As predicted from the low gas flow recorded during the stage 2 experiments, it was seen that of the total heat duty during this process, only a small amount is transferred due to the absorption of ammonia into ammonia + [emim][SCN] solution, and a large amount is transferred due to the sensible heat transfer between the solution and the cooling water, in case of most of the experimental data points.

(d) For lower flow rates of the solution, higher amount of heat is transferred because of the absorption phenomenon (eg, case 1, 10, 11 etc.), than that transferred for the higher flow rates (eg, case 15, 17 etc.). This in turn suggests that, for the lower flow rates, the ammonia vapor flow is higher than that for the higher flow rates, owing to the lower velocity of the solution.

(e) Owing to a low vapor flow, [emim][SCN] solution coming out of absorber is only slightly richer in ammonia than the solution going in, in case of the most of the experimental data points.

(f) The vapor flow was so low during these experiments, owing to the fact, that a temperature value higher than 95 °C is required at the generator thermostatic bath to vaporize sufficient ammonia out of the solution in the generator. The restriction on the equilibrium temperature in the generator (refer to section 5.2.2), might be a cause for a low vapor flow. For temperatures higher than 105 °C, higher vapor flow rates can be achieved (Wang, 2019), provided that the generator bath and its connections are properly insulated.

4. It was observed that the density of [emim][SCN] changes depending upon its use and the impurities present in it. Use of the density correlation for pure [emim][SCN] lead to an error in the calculation of the values of $w_{\text{NH}_3\text{,weak}}$. So, it is concluded that the density of [emim][SCN] has a considerable impact on the determination of the operating concentration making use of equation 4.11.

9

Future work and recommendations

In order to study the process of absorption even more thoroughly, and to get a completely sound understanding of the working of the setup, following recommendations are made. These recommendations include the shortcomings of the experimental setup, the shortcomings of the numerical model for the absorption process, and some general suggestions.

1. Future work to address the shortcomings of the experimental setup :
    (a) As has been mentioned in section 5.2.2, in the experimental setup at TU Delft, the density meter is placed before one of the precoolers through which ammonia + [emim][SCN] solution passes before entering the absorber. In order to get a more accurate measure of the density of the solution entering the absorber, it is recommended that the density meter be placed after the precooler and before the expansion valve, just before the absorber.
    (b) It is recommended that while performing a fresh set of absorption experiments at the setup, the temperature of the generator side TSB should be maintained higher than 105 °C, to get sufficient amount of vapor flow in the system (see figure 2.11). Also, a suggestion is made to properly insulate the generator side TSB in order to avoid large heat losses.
    (c) For the next stages of the absorption experiments on the experimental setup, it is suggested that the generator side thermostatic bath and its connections be insulated properly to avoid large heat losses.

2. Future work to address the shortcomings of the numerical model :
    (a) It is suggested that the excess enthalpy of ammonia + [emim][SCN] solution be included while calculating the total enthalpy of the solution. This would lead to a more accurate overall energy balance of the entire process and hence yield temperature outputs closer to the reality.
    (b) As mentioned in section 6.5.1, the amount of ammonia present in the vapor state in ammonia + [emim][SCN] solution due to flashing of the solution in an expansion valve from the generator pressure to the absorber pressure, should be considered while calculating the total vapor flow going into the absorber. This would help in reducing the error in the energy balance of the overall process.
    (c) For those cases where the value of $w_{\mathrm{NH_3,weak}}$ is more than the saturated value at the inlet conditions of the absorber, it is recommended that the correlations governing the absorption (equations 6.6 and 6.7) be optimized based on the desired outlet conditions. For this, a separate Matlab function can be added to the existing model to optimize coefficients (a and b in equation 6.5) as suggested by Wang (2019) (see figure 6.1 for the algorithm). This would simulate the whole process more clearly and give a clearer idea of the desorption, absorption and the sensible heat exchange lengths in the absorber.

3. It is strongly recommended that a small sample of [emim][SCN] in the system be subjected to the density measurement varying with temperature, in order to have an exact correlation of the variation in the density of the used [emim][SCN] with temperature, before performing the next stages of the absorption experiments. This is to be done in order to account for the impurities that are present in the ionic liquid, and to estimate the exact concentration of ammonia in the solution going into the absorber ($w_{\mathrm{NH_3,weak}}$). This would help understand the absorption process for a particular case thoroughly.

Bibliography

1. Almeida, H., Teles, A., Lopes-da-Silva, J., Freire, M. and Coutinho, J. (2012). Influence of the anion on the surface tension of 1-ethyl-3-methylimidazolium-based ionic liquids. The Journal of Chemical Thermodynamics, 54, pp.49-54.
2. Amaris Castilla, C. (2014). Intensification of NH3 bubble absorption process using advanced surfaces and carbon nanotubes for NH3/LINO3 absorption chillers. [Tarragona]: Universitat Rovira i Virgili.
3. Amaris Castilla, C., Bourouis, M. and Vallès, M. (2014). Passive intensification of the ammonia absorption process with NH3/LiNO3 using carbon nanotubes and advanced surfaces in a tubular bubble absorber. Energy, 68, pp.519-528.
4. Bedia, J., Palomar, J., Gonzalez-Miquel, M., Rodriguez, F. and Rodriguez, J. (2012). Screening ionic liquids as suitable ammonia absorbents on the basis of thermodynamic and kinetic analysis. Separation and Purification Technology, 95, pp.188-195.
5. Bell I. (2019). Plate heat exchangers geometry , http://achp.sourceforge.nel/ACHP Compone nts/PlateHeatExchanger.html.
6. Cera-Manjarres, A. (2015). Experimental determination and modelling of thermophysical properties of ammonia/ionic liquid mixtures for absorption refrigeration systems, Ph.D. thesis, Universitat Rovira i Virgili.
7. Cerezo, J., Bourouis, M., Vallès, M., Coronas, A. and Best, R. (2009). Experimental study of an ammonia–water bubble absorber using a plate heat exchanger for absorption refrigeration machines. Applied Thermal Engineering, 29(5-6), pp.1005-1011.
8. Domańska, U., Królikowska, M. and Królikowski, M. (2010). Phase behaviour and physicochemical properties of the binary systems 1-ethyl-3-methylimidazolium thiocyanate, or 1-ethyl-3-methylimidazolium tosylate+water, or+an alcohol. Fluid Phase Equilibria, 294(1-2), pp.72-83.
9. Donowski V. and Kandlikar S. (1999). Correlating evaporation heat transfer coefficient of refrigerant r-134a in a plate heat exchanger, ASME Journal of Heat Transfer, vol. 121(1), pp. 118-127.
10. Ficke, L., Novak, R. and Brennecke, J. (2010). Thermodynamic and Thermophysical Properties of Ionic Liquid + Water Systems. Journal of Chemical Engineering Data, 55(11), pp.4946-4950.
11. Fröba, A., Rausch, M., Krzeminski, K., Assenbaum, D., Wasserscheid, P. and Leipertz, A. (2010). Thermal Conductivity of Ionic Liquids: Measurement and Prediction. International Journal of Thermophysics, 31(11-12), pp.2059-2077.
12. Gao, J. and Wagner, N. (2016). Non-ideal viscosity and excess molar volume of mixtures of 1-butyl-3-methylimidazolium tetrafluoroborate ([C 4 mim][BF 4]) with water. Journal of Molecular Liquids, 223, pp.678-686.
13. Grossman, G. (1983). Simultaneous heat and mass transfer in film absorption under laminar flow. International Journal of Heat and Mass Transfer, 26(3), pp.357-371.
14. Hofmann, A., Migeot, M. and Hanemann, T. (2015). Investigation of Binary Mixtures Containing 1-Ethyl-3-methylimidazolium Bis(trifluoromethanesulfonyl)azanide and Ethylene Carbonate. Journal of Chemical Engineering Data, 61(1), pp.114-123.
15. Images.google.com. (2019). Google Images. [online] Available at: https://images.google.com/.

16. Kang, Y. T., Akisawa, A., Kashiwagi, T. (2000). Analytical Investigation of Two Different Absorption Modes: Falling Film and Bubble Types. International Journal of Refrigeration, 23(6), p.430-443.
17. Khan, T., Khan, M., Chyu, M. and Ayub, Z. (2010). Experimental investigation of single phase convective heat transfer coefficient in a corrugated plate heat exchanger for multiple plate configurations. Applied Thermal Engineering, 30(8-9), pp.1058-1065.
18. Kim, S., Kim, Y., Joshi, Y., Fedorov, A. and Kohl, P. (2012). Absorption Heat Pump/Refrigeration System Utilizing Ionic Liquid and Hydrofluorocarbon Refrigerants. Journal of Electronic Packaging, 134(3).
19. Kuikhoven, L. (2019). The influence of the ammonia concentration on the performance of OTEC power cycles. [online] Repository.tudelft.nl. Available at: https://repository.tudelft.nl/islandora/object/uuid
20. Lemmon E. W., Bell I., Huber M. L., and McLinden M. O. (2010). NIST Standard Reference Database 23: Reference Fluid Thermodynamic and Transport Properties-REFPROP, Version 9.0, National Institute of Standards and Technology, [Online]. Available: https://www.nist.gov/srd/refprop.
21. Mills, A. (2015). Basic heat and mass transfer. San Diego, California: Prentice Hall.
22. Paulechka, Y. (2010). Heat Capacity of Room-Temperature Ionic Liquids: A Critical Review. Journal of Physical and Chemical Reference Data, 39(3), p.033108.
23. Salgado, J., Regueira, T., Lugo, L., Vijande, J., Fernández, J. and García, J. (2014). Density and viscosity of three (2,2,2-trifluoroethanol+1-butyl-3-methylimidazolium) ionic liquid binary systems. The Journal of Chemical Thermodynamics, 70, pp.101-110.
24. Schilperoort, F., Oude Aarninkhof, B. J., Rahro, S., Klifman B. R., Franco Pinto, N. (2019). A study in the heat transfer of absorption heat pump systems based on an Ammonia/Ionic liquid pair.
25. Tenney, C., Massel, M., Mayes, J., Sen, M., Brennecke, J. and Maginn, E. (2014). A Computational and Experimental Study of the Heat Transfer Properties of Nine Different Ionic Liquids. Journal of Chemical Engineering Data, 59(2), pp.391-399.
26. Towler, G. and Sinnott, R. (2013). Chemical engineering design. Oxford, UK: Butterworth-Heinemann.
27. Triché, D., Bonnot, S., Perier-Muzet, M., Boudéhenn, F., Demasles, H. and Caney, N. (2017). Experimental and numerical study of a falling film absorber in an ammonia-water absorption chiller. International Journal of Heat and Mass Transfer, 111, pp.374-385.
28. Valkenburg, M., Vaughn, R., Williams, M. and Wilkes, J. (2005). Thermochemistry of ionic liquid heat-transfer fluids. Thermochimica Acta, 425(1-2), pp.181-188.
29. Vataščin, E. and Dohnal, V. (2017). Thermodynamic properties of aqueous solutions of [EMIM] thiocyanate and [EMIM] dicyanamide. The Journal of Chemical Thermodynamics, 106, pp.262-275.
30. Wang, M.(2019) Highly efficient absorption heat pump and refrigeration systems based on ionic liquids. PhD thesis, Delft University of Technology.
31. Wang, M., He, L. and Infante Ferreira, C. (2019). Ammonia absorption in ionic liquids-based mixtures in plate heat exchangers studied by a semi-empirical heat and mass transfer framework. International Journal of Heat and Mass Transfer, 134, pp.1302-1317.
32. Wang, M. and Infante Ferreira, C. (2017). Absorption heat pump cycles with NH3 – ionic liquid working pairs. Applied Energy, 204, pp.819-830.
33. Winkelmann, D. (2010). Condensation of pure refrigerants and their zeotropic mixtures in plate heat exchangers. Hannover: DKV.

34. Yan, Y. and Lin, T. (1999). Evaporation Heat Transfer and Pressure Drop of Refrigerant R-134a in a Plate Heat Exchanger. Journal of Heat Transfer, 121(1), pp.118-127.

35. Yokozeki, A. and Shiflett, M. (2007). Vapor–liquid equilibria of ammonia+ionic liquid mixtures. Applied Energy, 84(12), pp.1258-1273.

Appendices

.1. Appendix A : Figures

1. Results of the numerical modelling

   (a) Temperature and concentration profiles for case 1

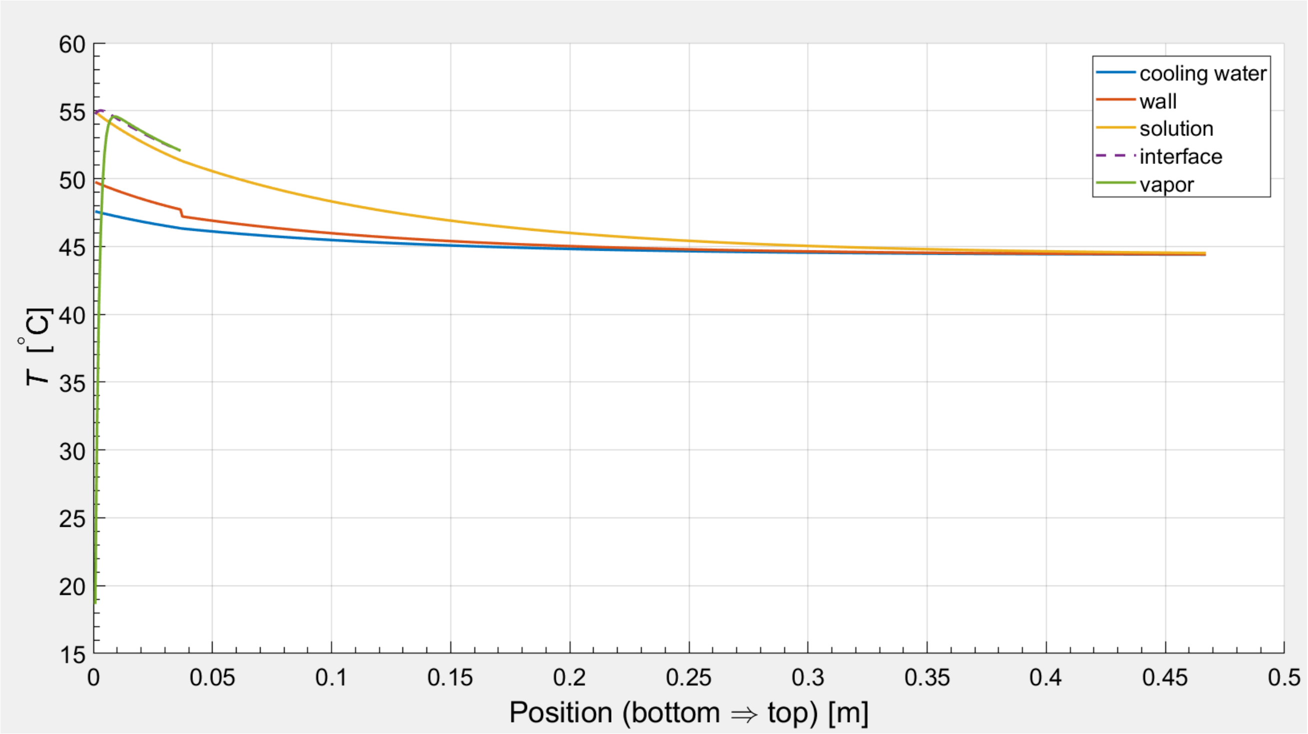

Figure 1: Temperature profile obtained from numerical modelling for case 1

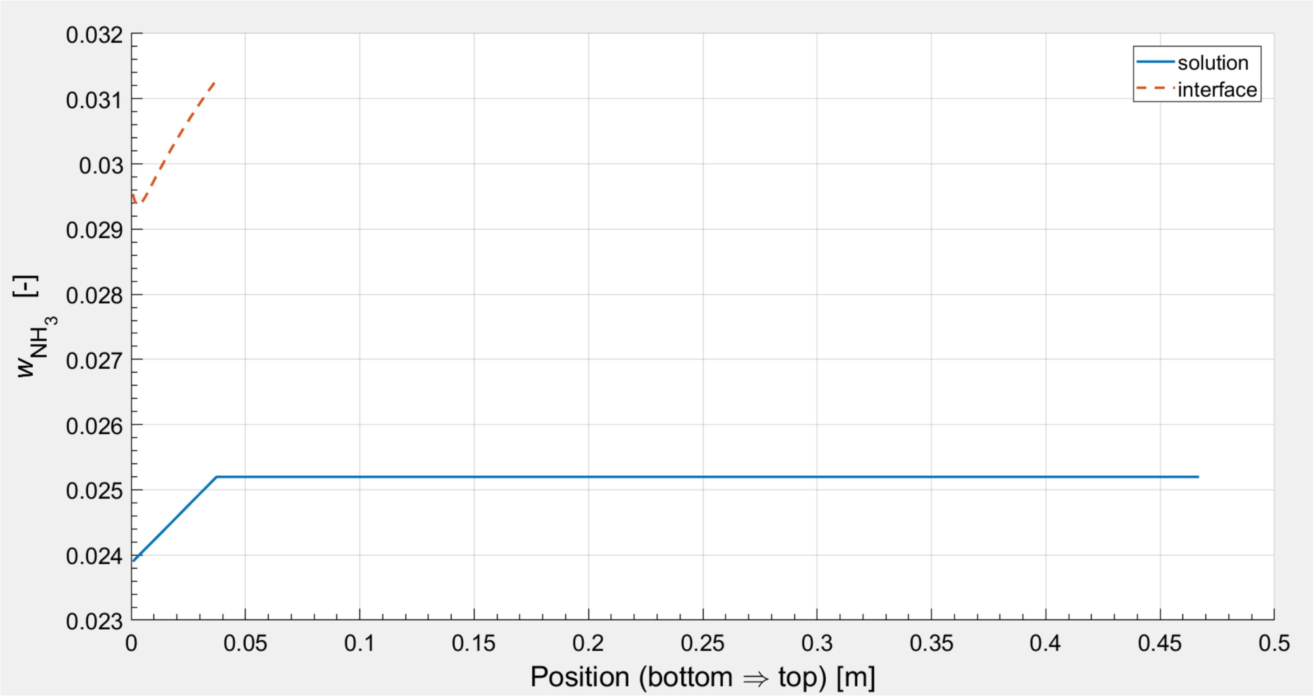

Figure 2: Concentration profile obtained from numerical modelling for case 1

(b) Temperature and concentration profiles for case 5

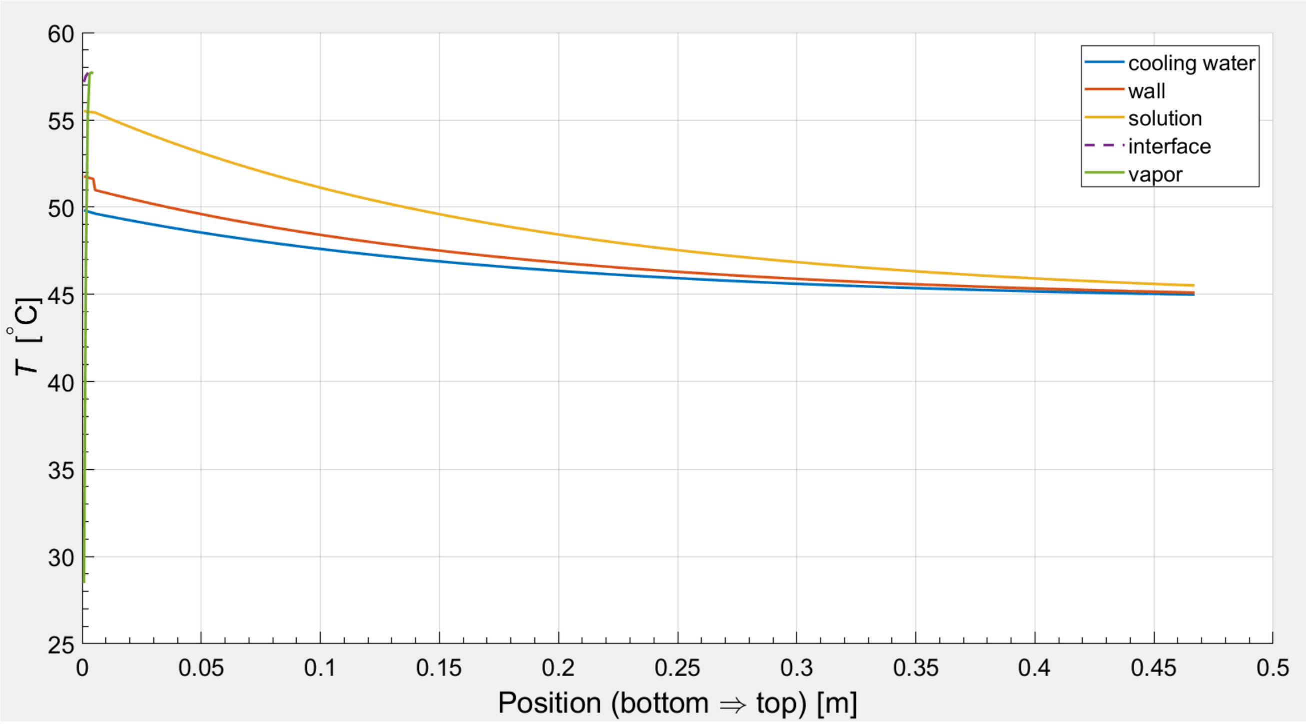

Figure 3: Temperature profile obtained from numerical modelling for case 5

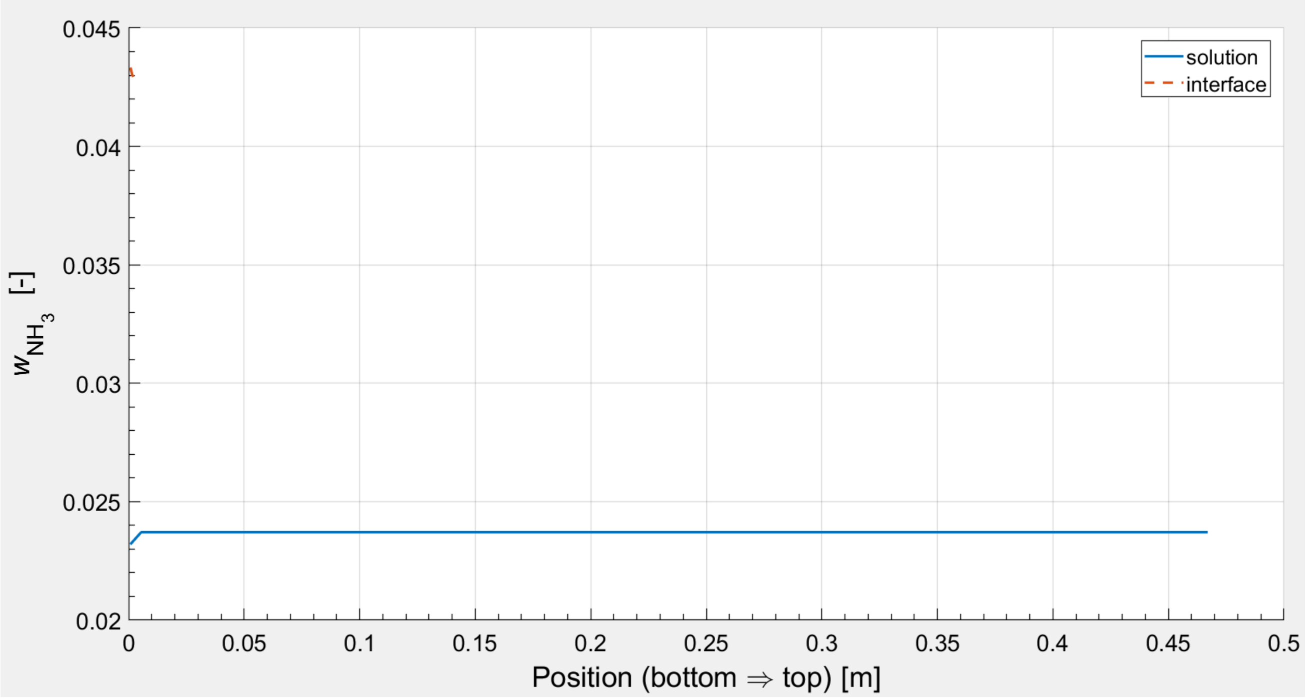

Figure 4: Concentration profile obtained from numerical modelling for case 5

(c) Temperature and concentration profiles for case 6

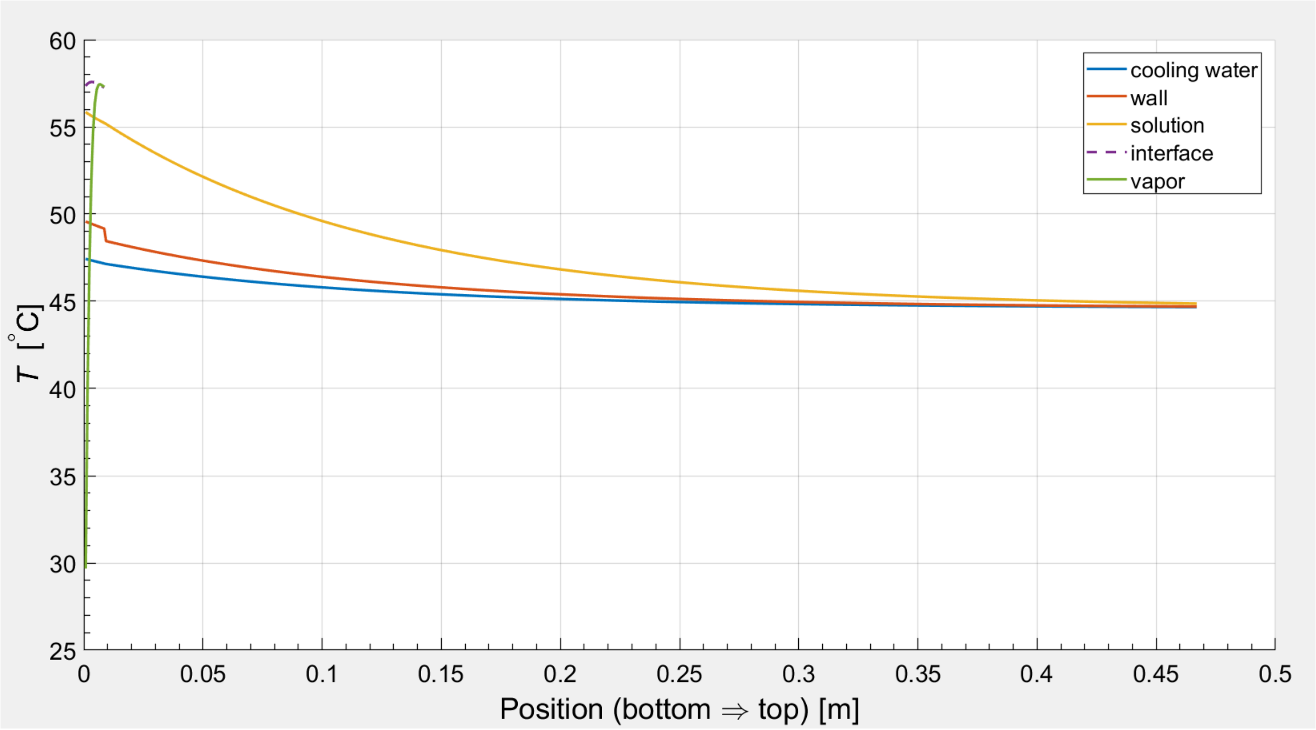

Figure 5: Temperature profile obtained from numerical modelling for case 6

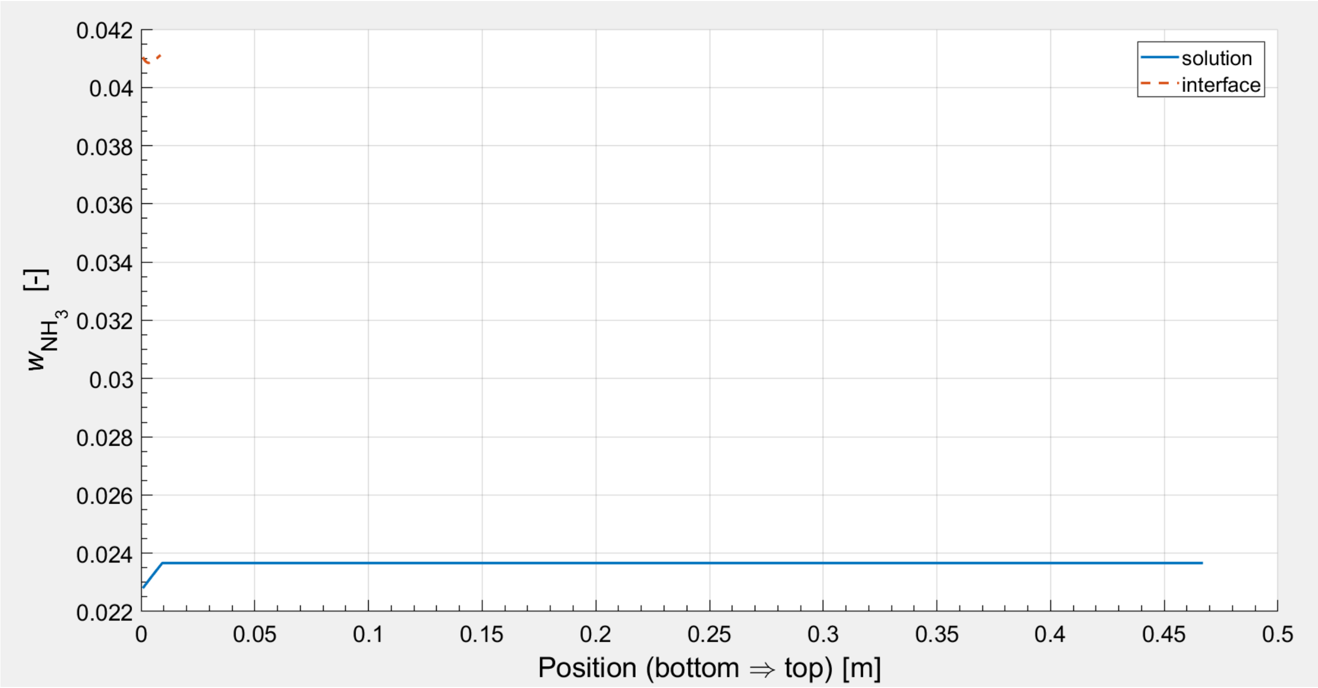

Figure 6: Concentration profile obtained from numerical modelling for case 6

(d) Temperature and concentration profiles for case 7

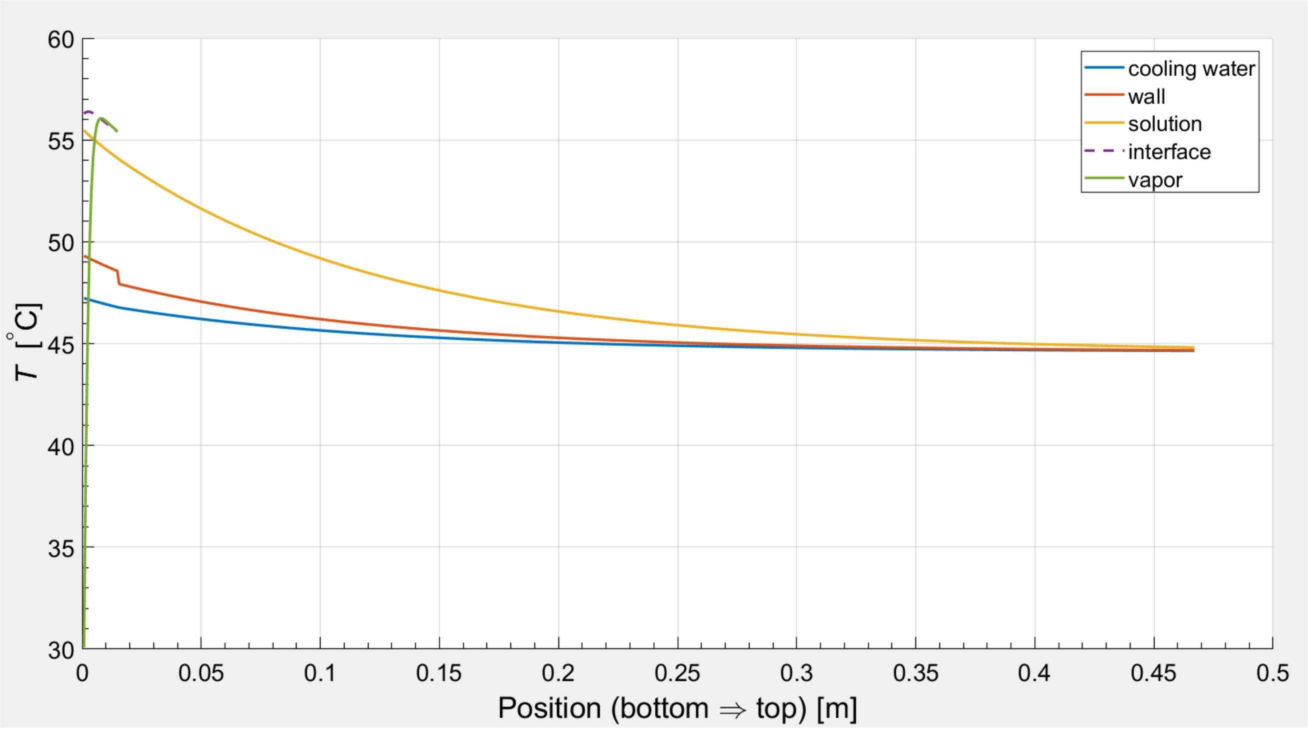

Figure 7: Temperature profile obtained from numerical modelling for case 7

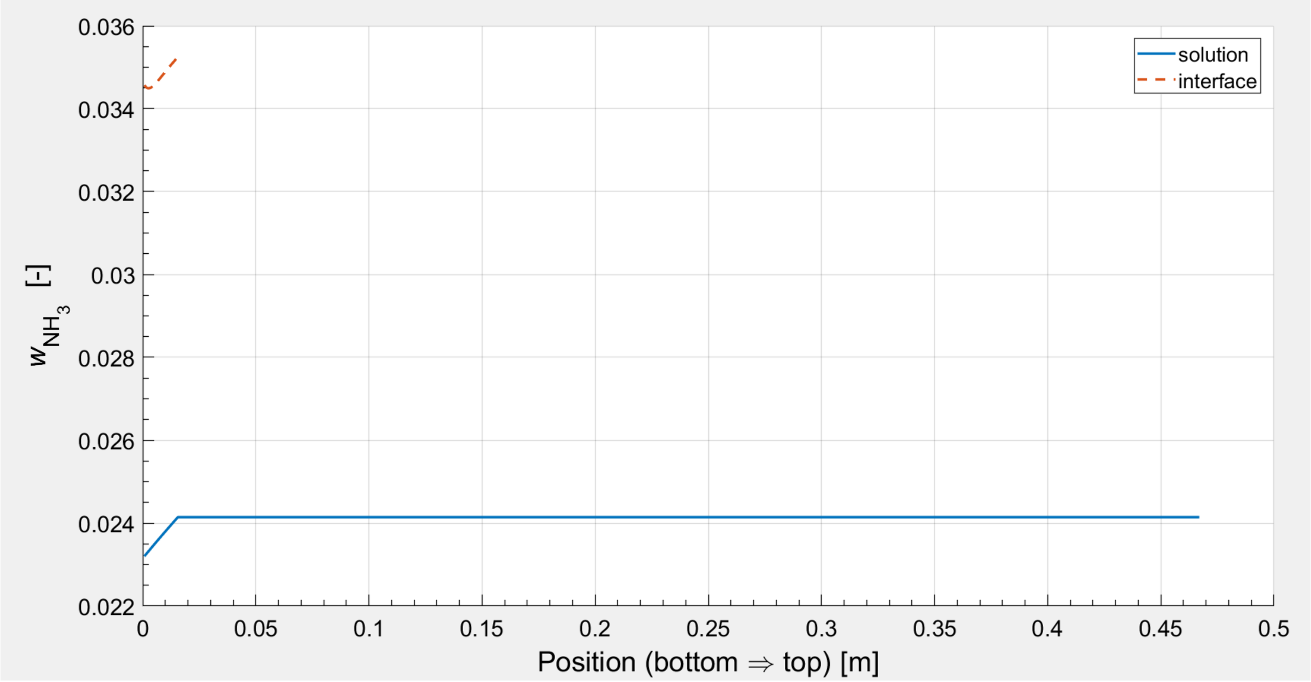

Figure 8: Concentration profile obtained from numerical modelling for case 7

(e) Temperature and concentration profiles for case 9

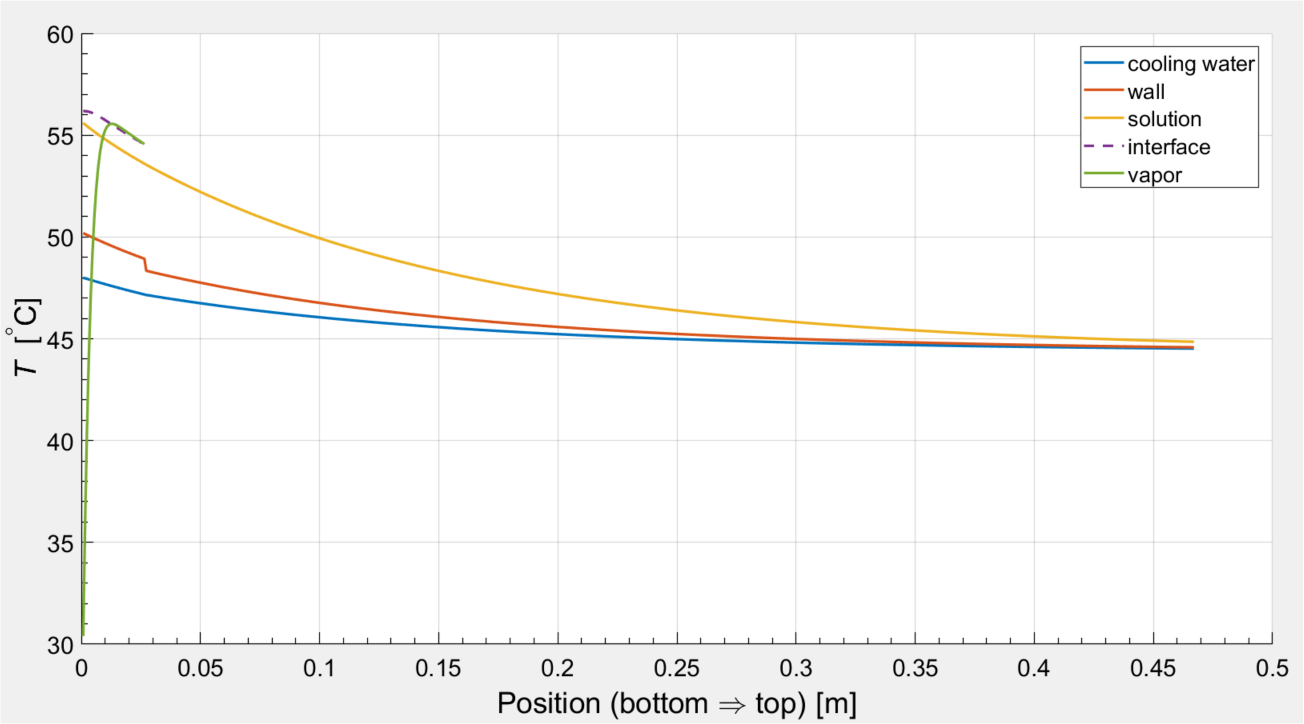

Figure 9: Temperature profile obtained from numerical modelling for case 9

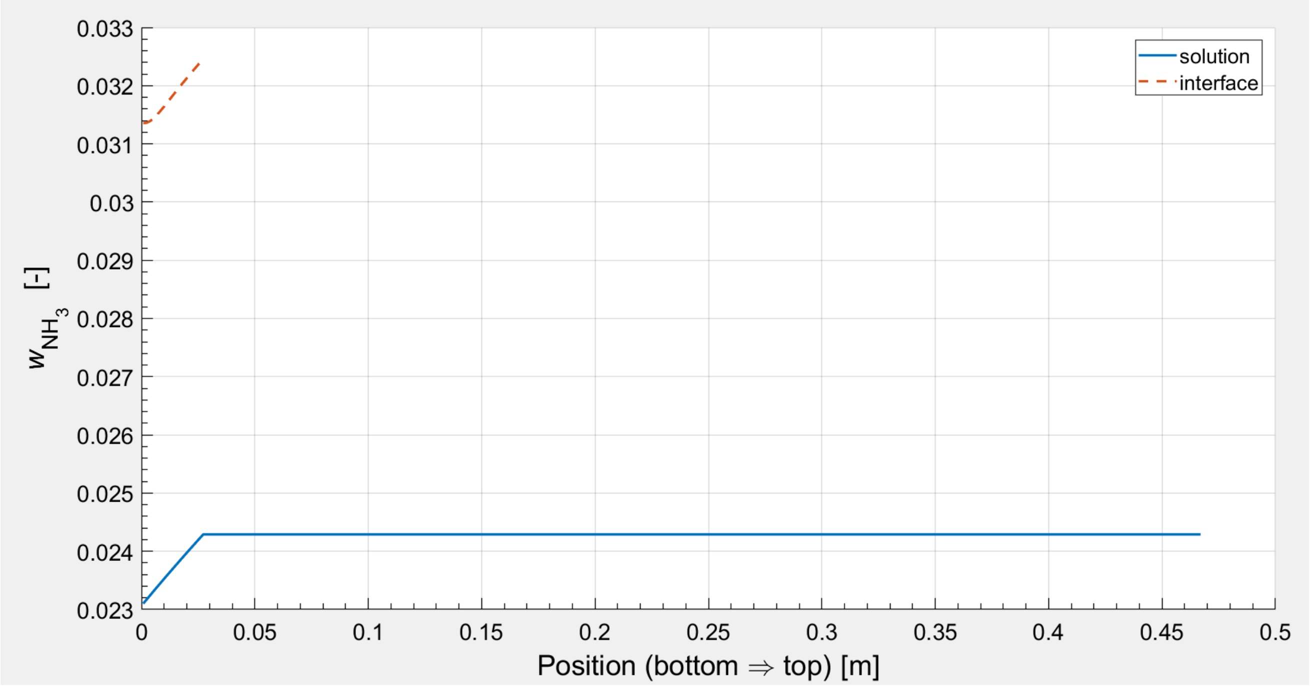

Figure 10: Concentration profile obtained from numerical modelling for case 9

(f) Temperature and concentration profiles for case 11

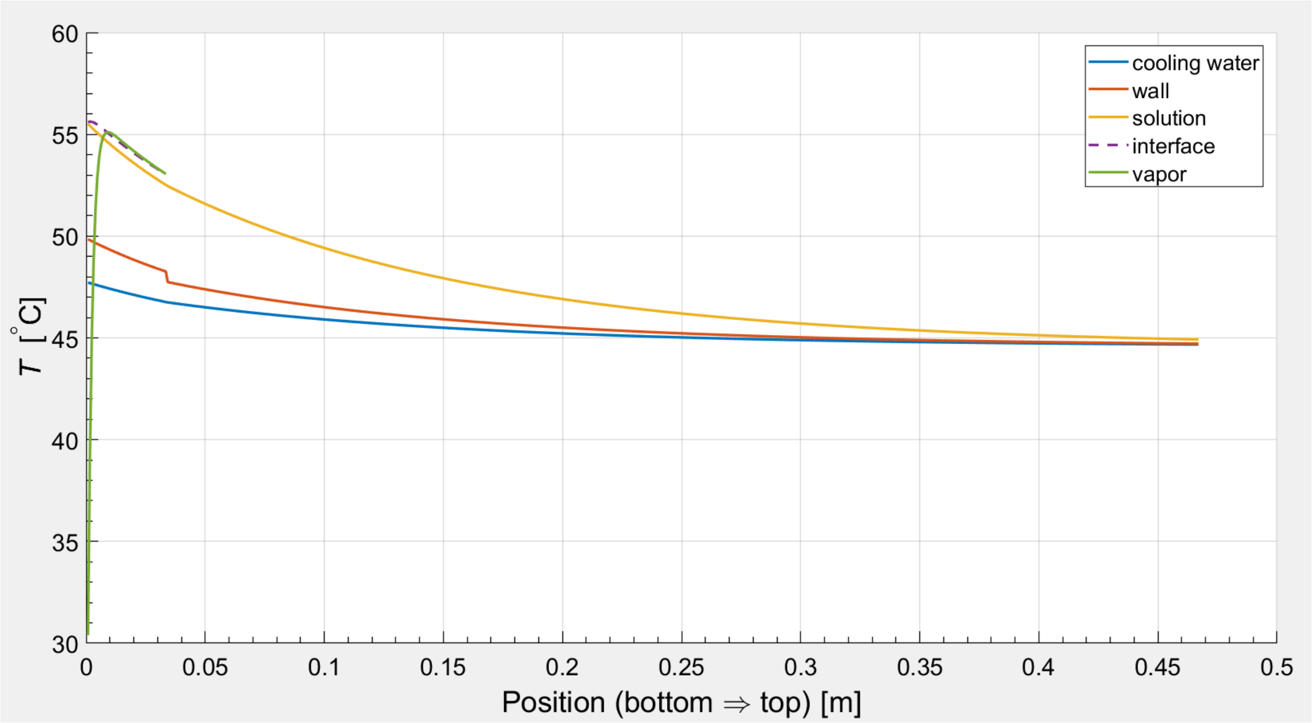

Figure 11: Temperature profile obtained from numerical modelling for case 11

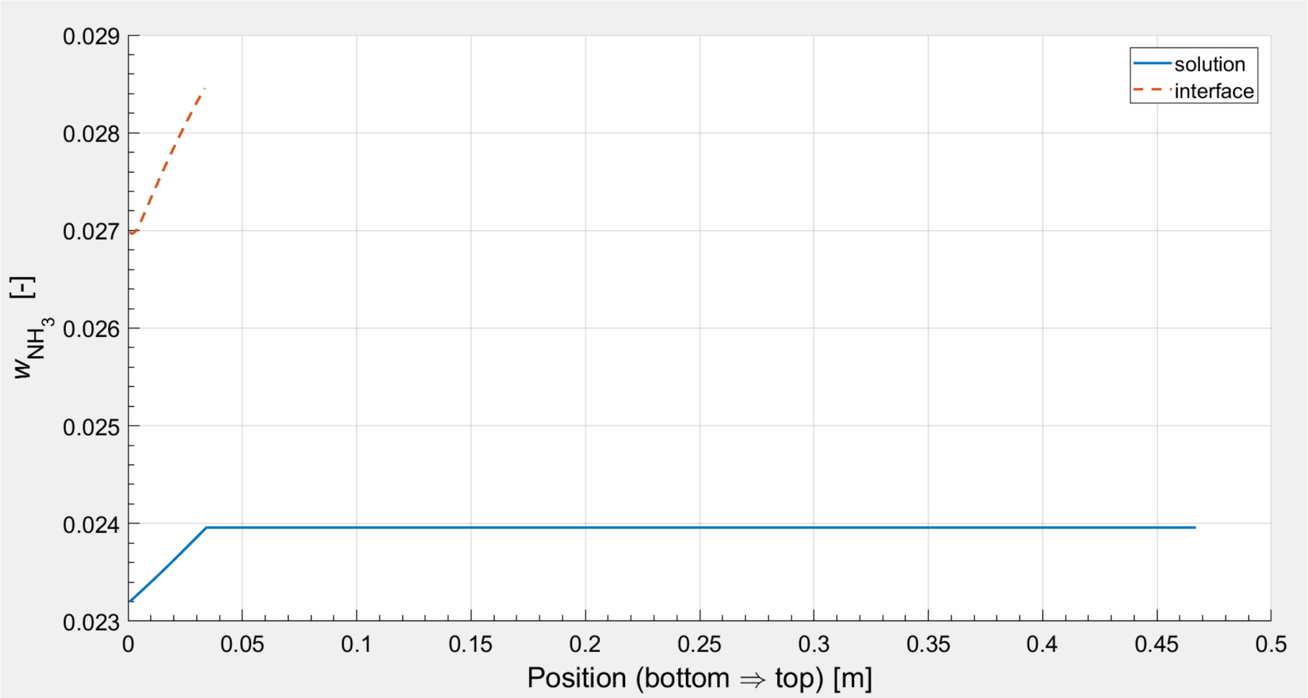

Figure 12: Concentration profile obtained from numerical modelling for case 11

(g) Temperature and concentration profiles for case 12

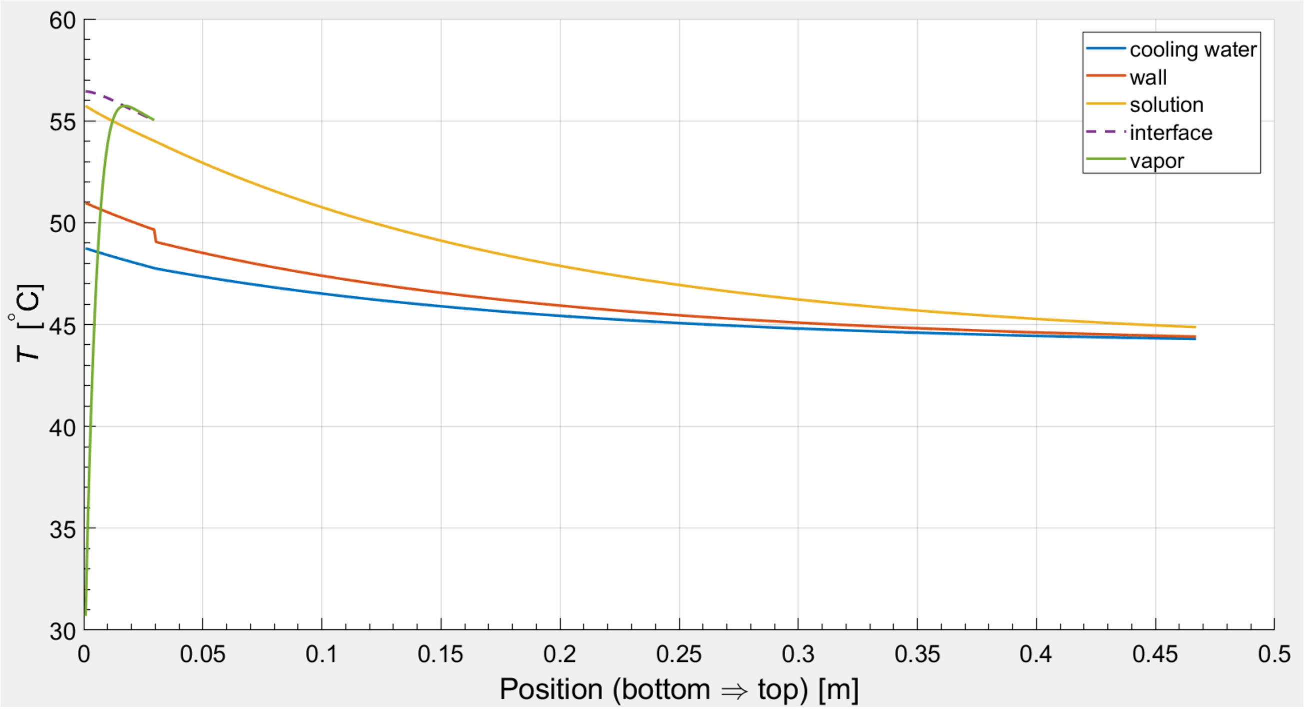

Figure 13: Temperature profile obtained from numerical modelling for case 12

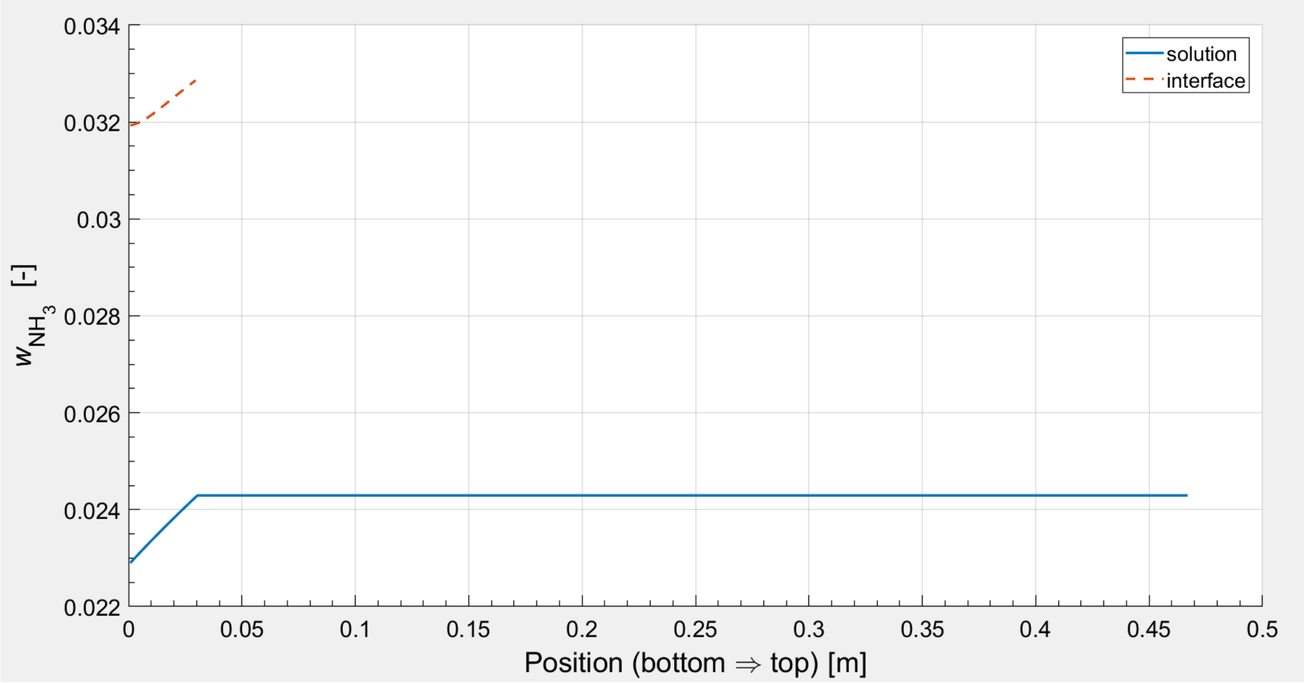

Figure 14: Concentration profile obtained from numerical modelling for case 12

(h) Temperature and concentration profiles for case 13

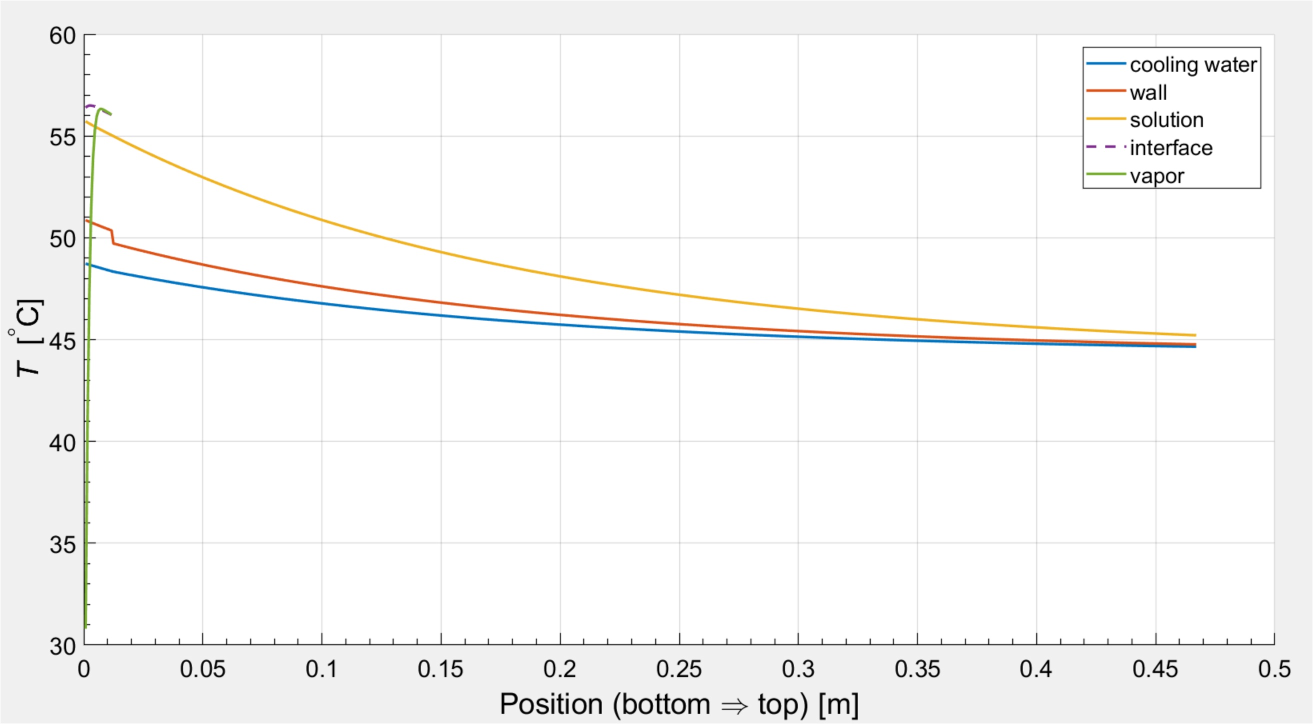

Figure 15: Temperature profile obtained from numerical modelling for case 13

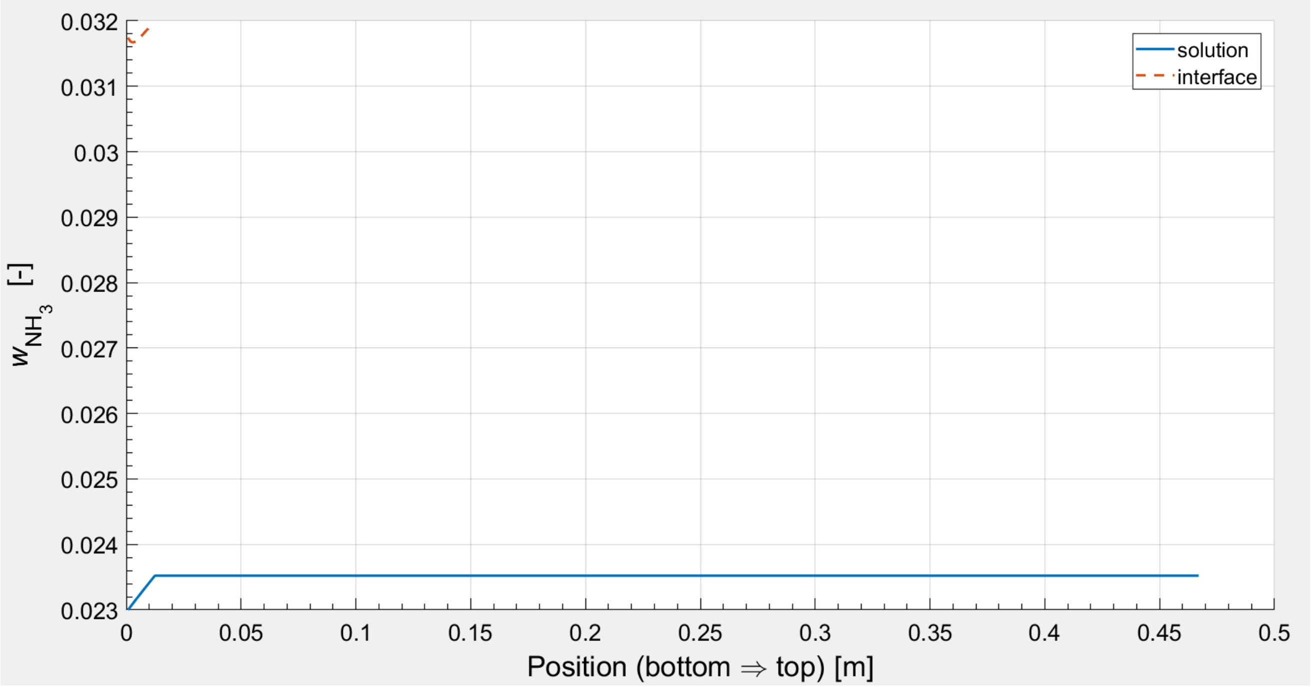

Figure 16: Concentration profile obtained from numerical modelling for case 13

(i) Temperature and concentration profiles for case 14

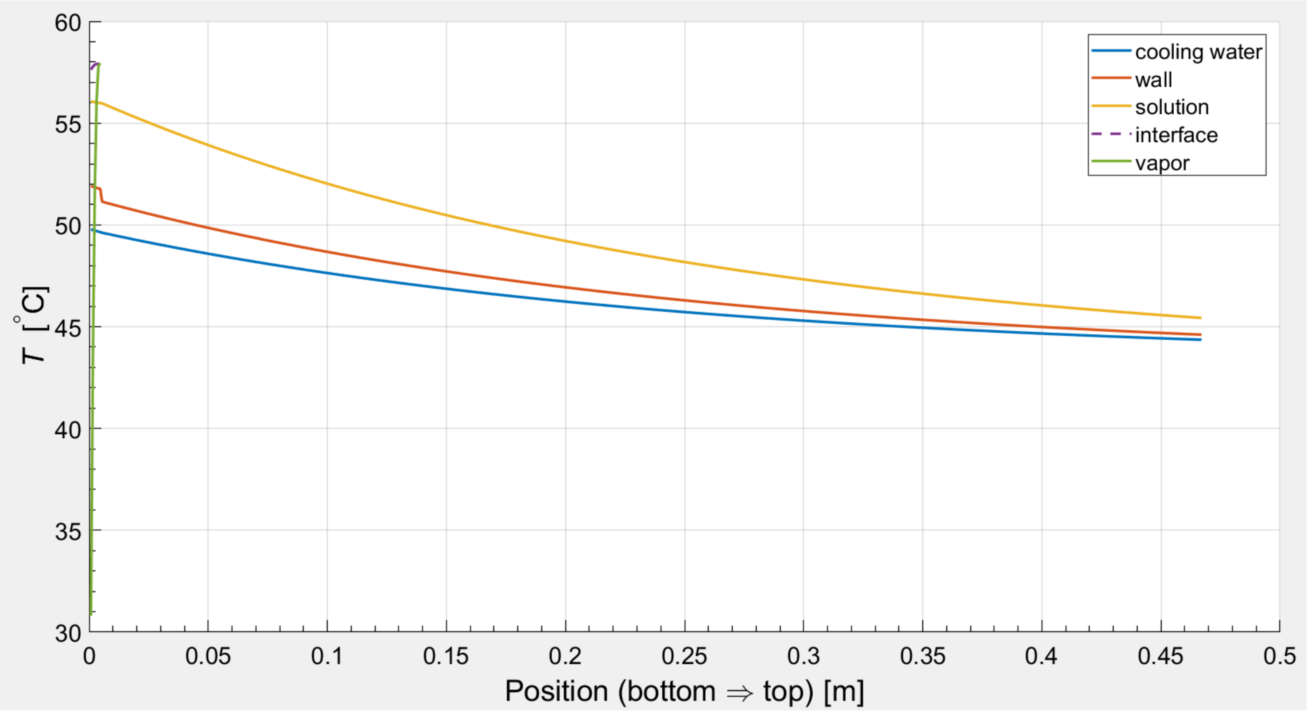

Figure 17: Temperature profile obtained from numerical modelling for case 14

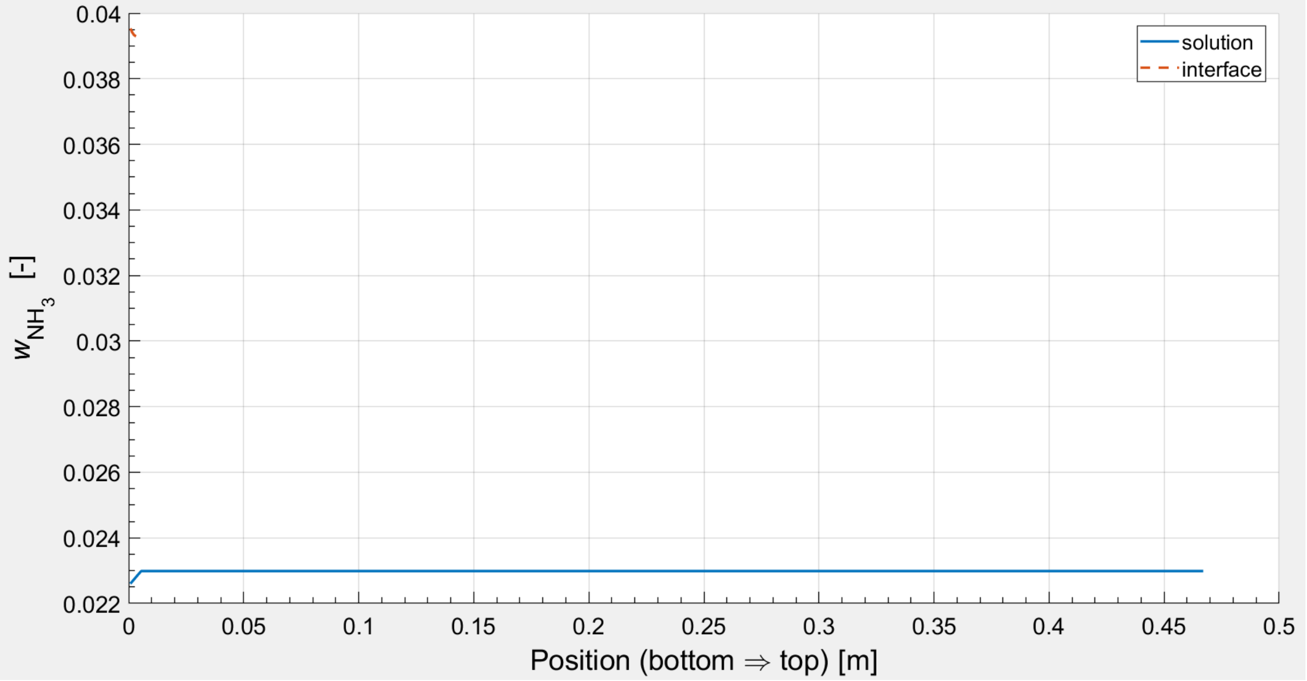

Figure 18: Concentration profile obtained from numerical modelling for case 14

(j) Temperature and concentration profiles for case 15

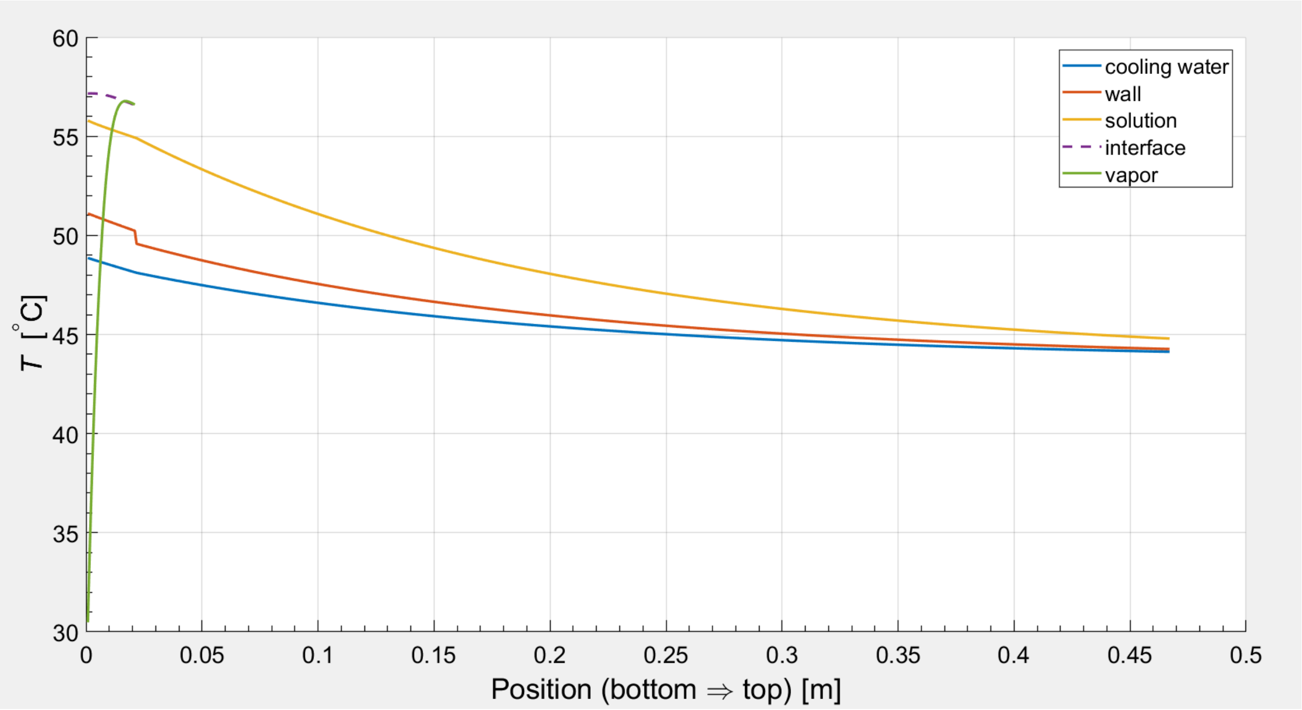

Figure 19: Temperature profile obtained from numerical modelling for case 15

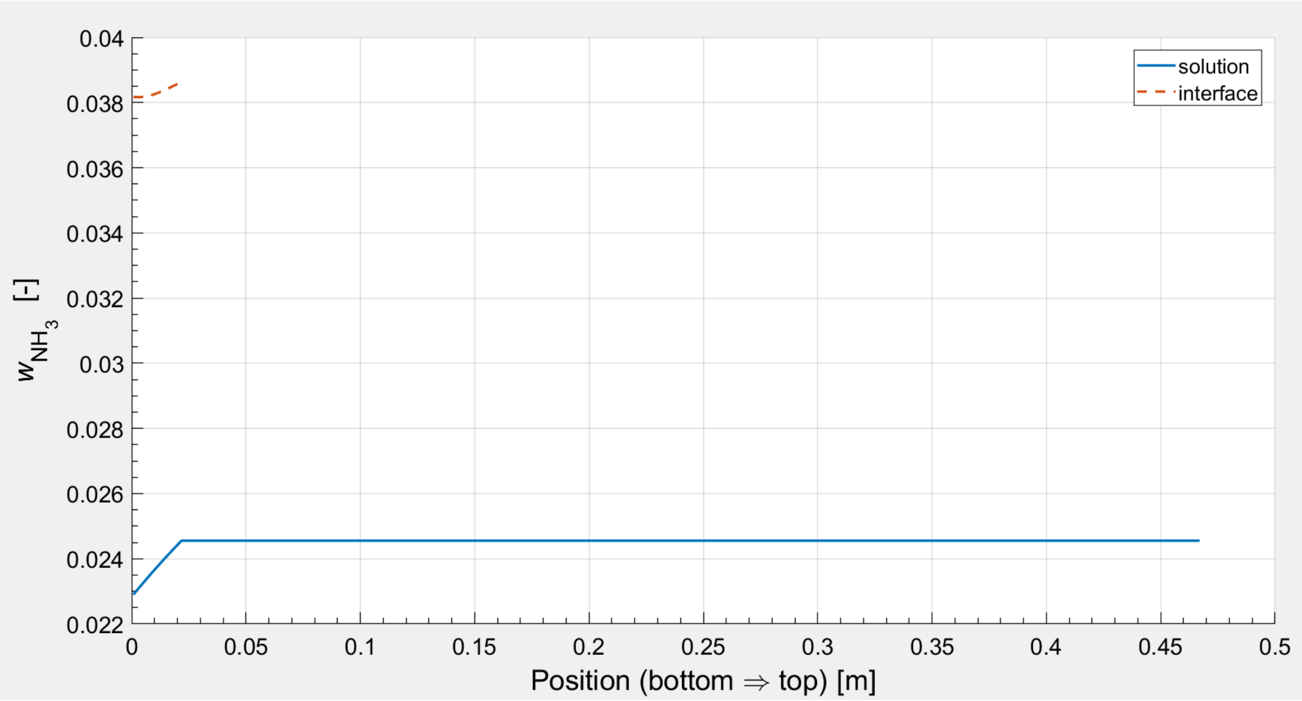

Figure 20: Concentration profile obtained from numerical modelling for case 15

(k) Temperature and concentration profiles for case 18

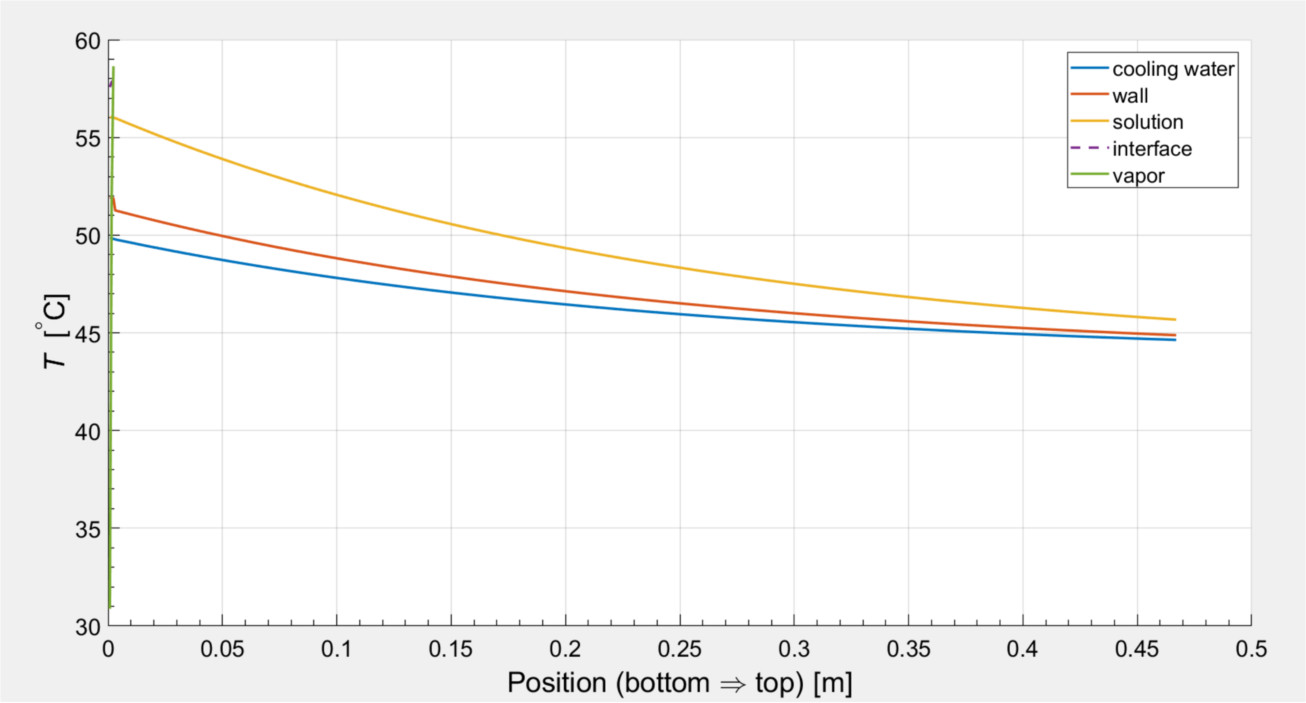

Figure 21: Temperature profile obtained from numerical modelling for case 18

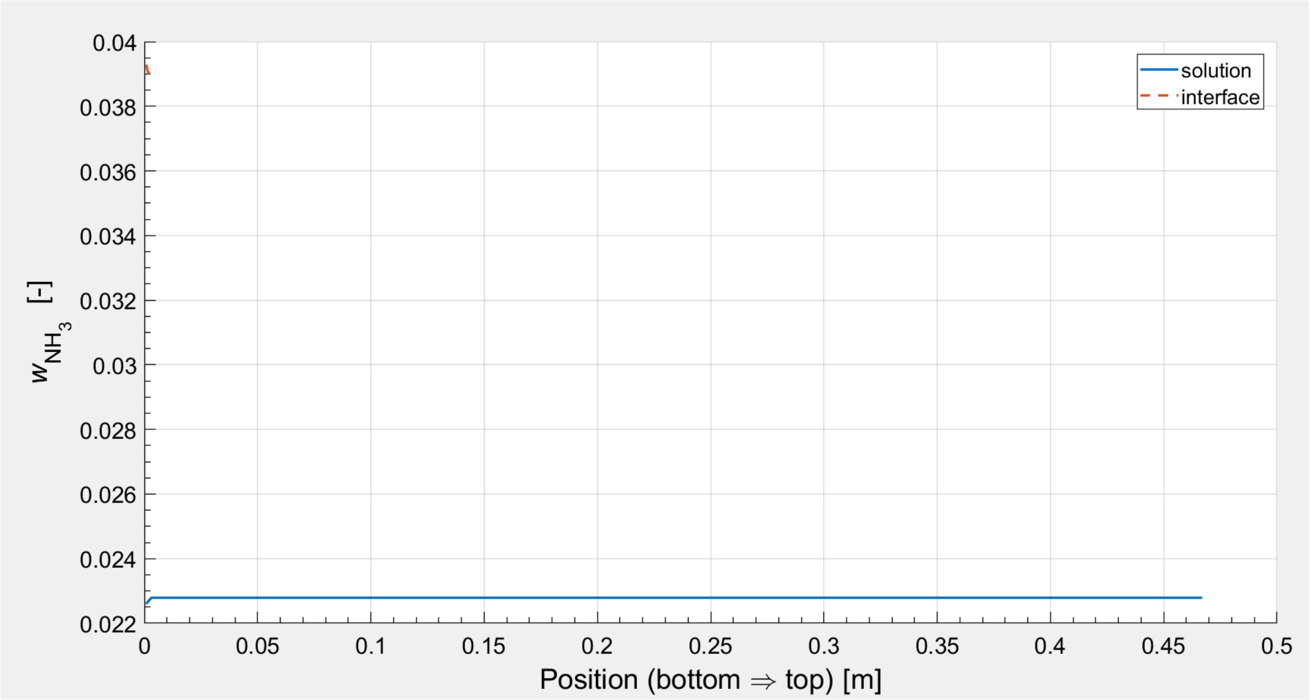

Figure 22: Concentration profile obtained from numerical modelling for case 18

(l) Temperature and concentration profiles for case 19

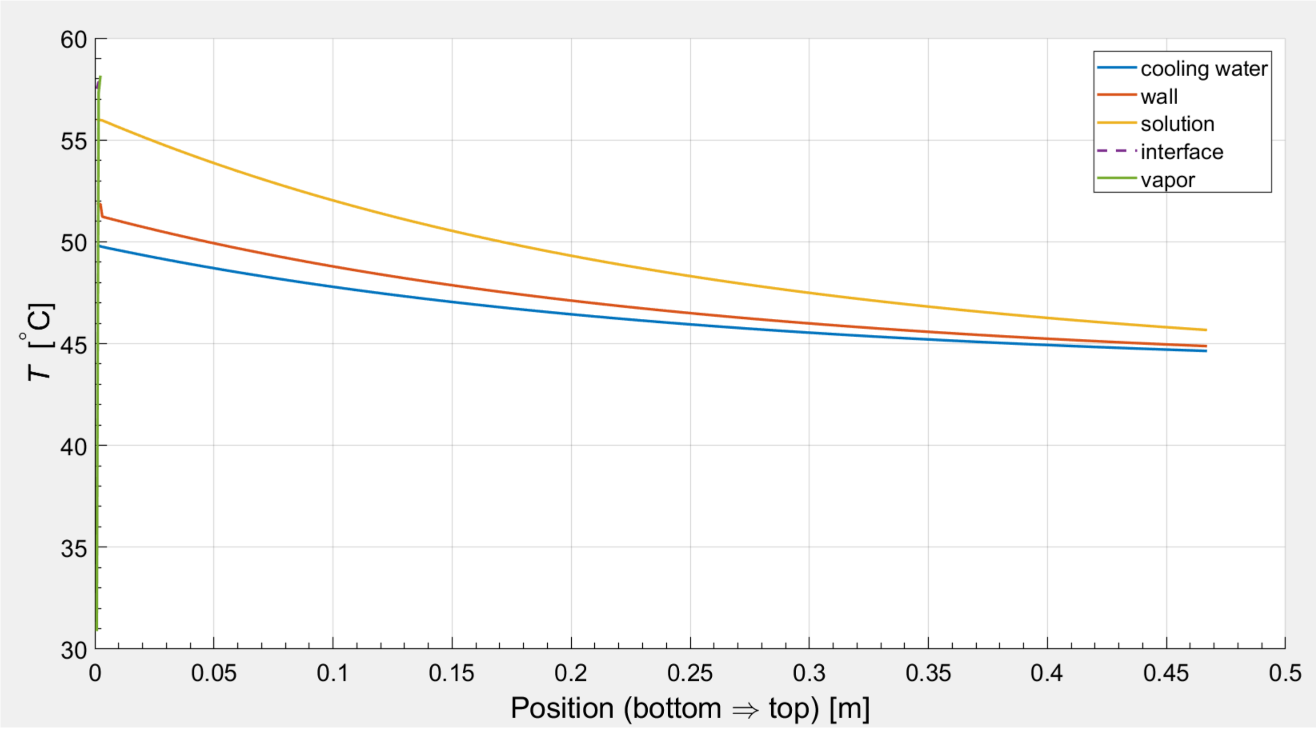

Figure 23: Temperature profile obtained from numerical modelling for case 19

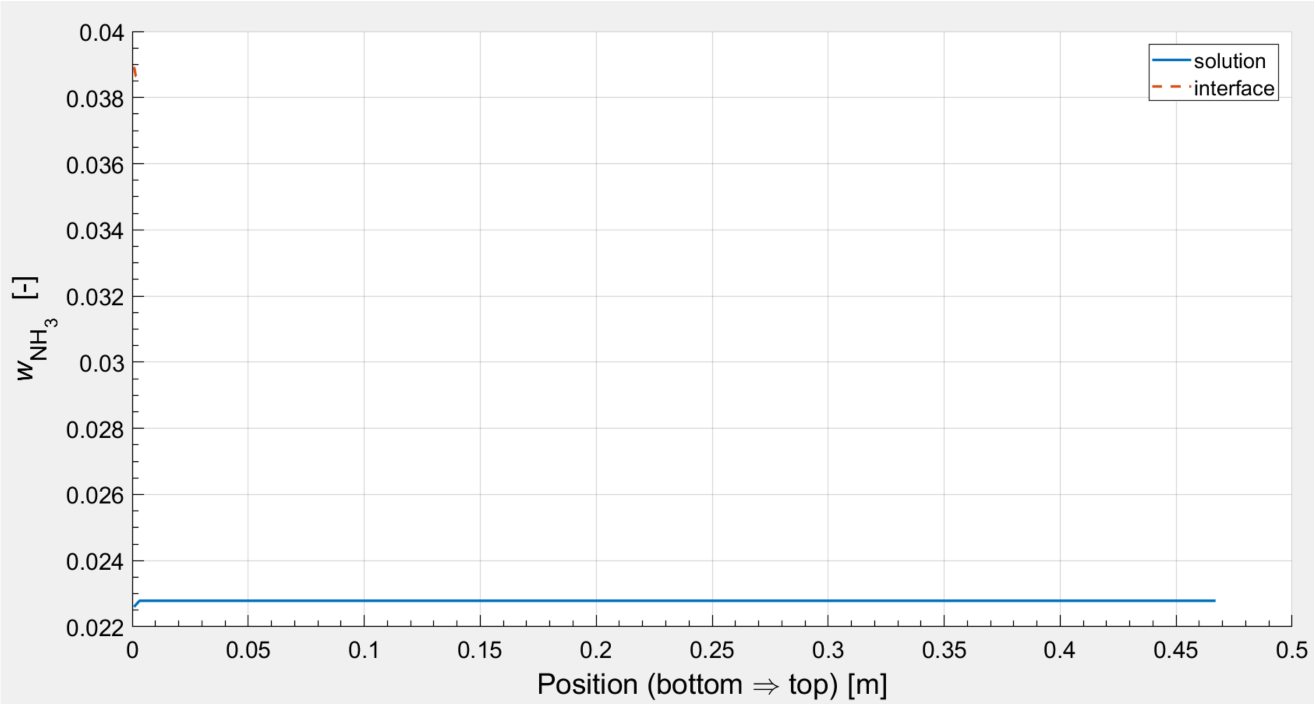

Figure 24: Concentration profile obtained from numerical modelling for case 19

2. PTw diagram for the solution of [emim][SCN]+ammonia

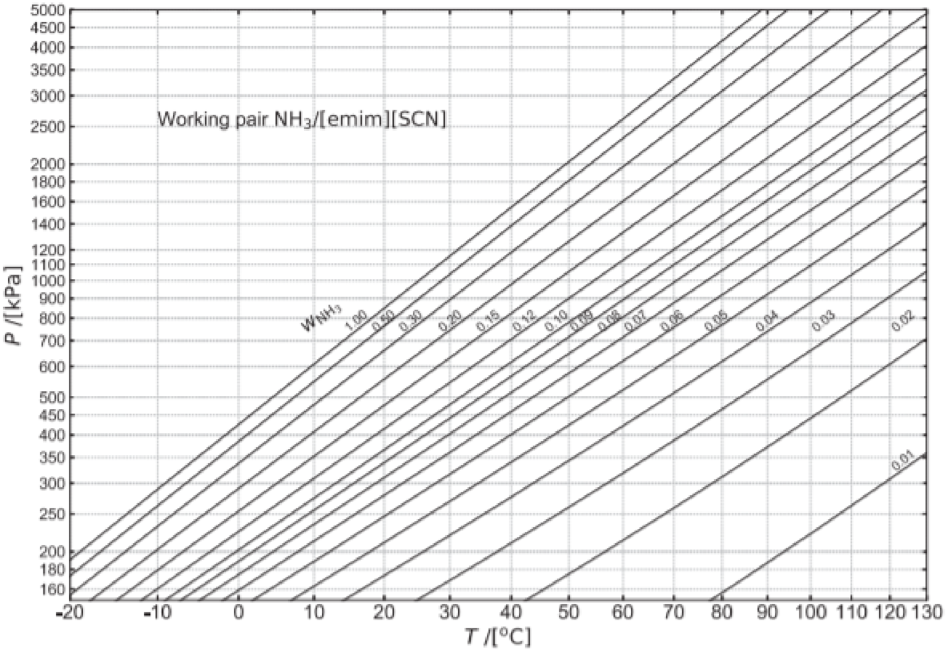

Figure 25: PTw diagram of the solution of [emim][SCN]+ammonia (Wang, 2019)

3. hw diagram for the solution of [emim][SCN]+ammonia

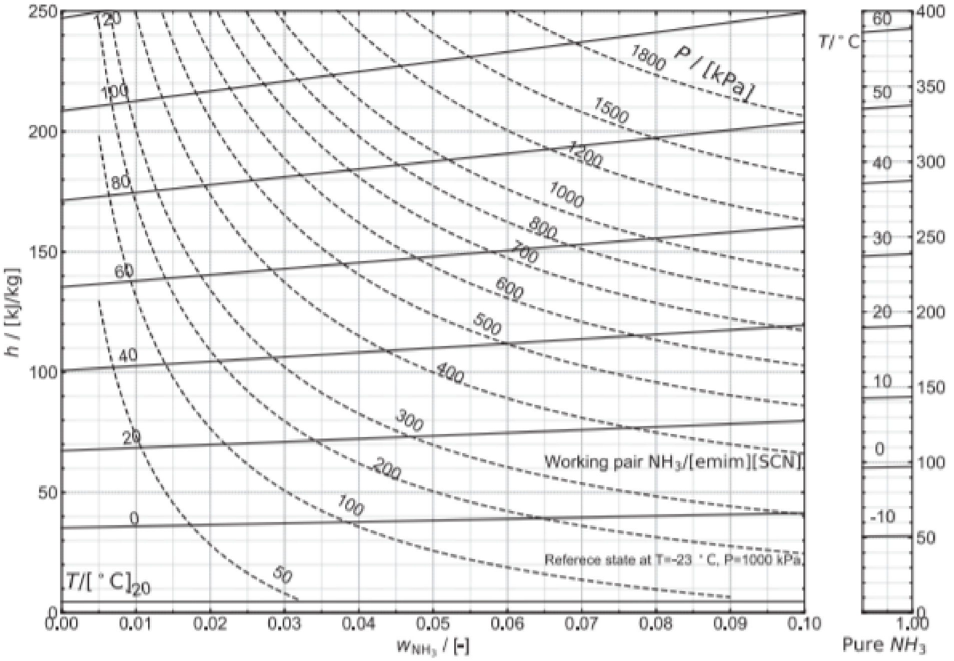

Figure 26: hw diagram for the solution of [emim][SCN]+ammonia (Wang, 2019)

4. Temperature distribution for ammonia - [emim][SCN] working pair as predicted by Wang (2019) :

   Figure 27 displays the temperature of the solution coming out of the absorber ($T_{\text{abs,out}}$), from the bottom of the PHX to the top.

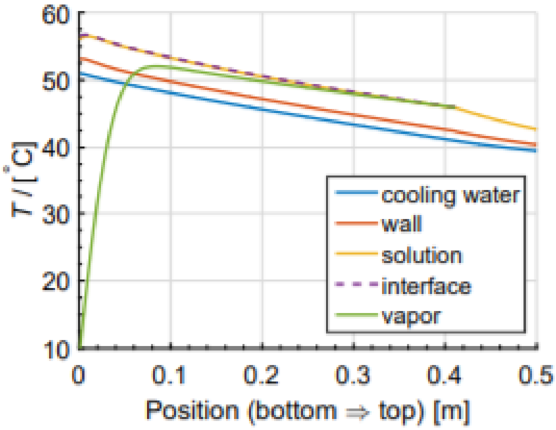

Figure 27: Temperature distribution for ammonia - [emim][SCN] (Wang, 2019)

5. Concentration distribution for ammonia - IL working pair as predicted by Wang (2019) :

   Figure 28 displays the mass concentration of ammonia both in the bulk solution and at the interface, starting from the bottom of the PHX to the top.

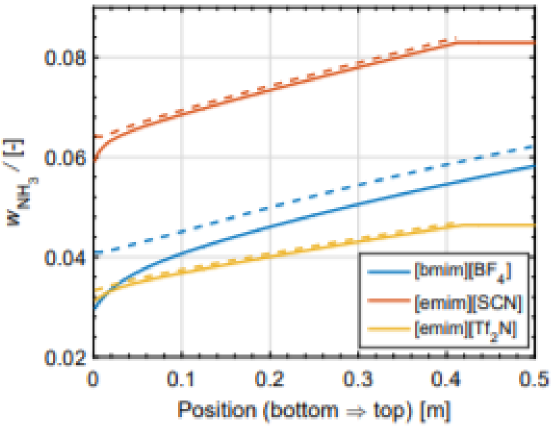

Figure 28: Concentration distribution for ammonia - IL working pair (Wang, 2019)

6. Critical conditions for several different ionic liquids, and the molecular weights of these ionic liquids.

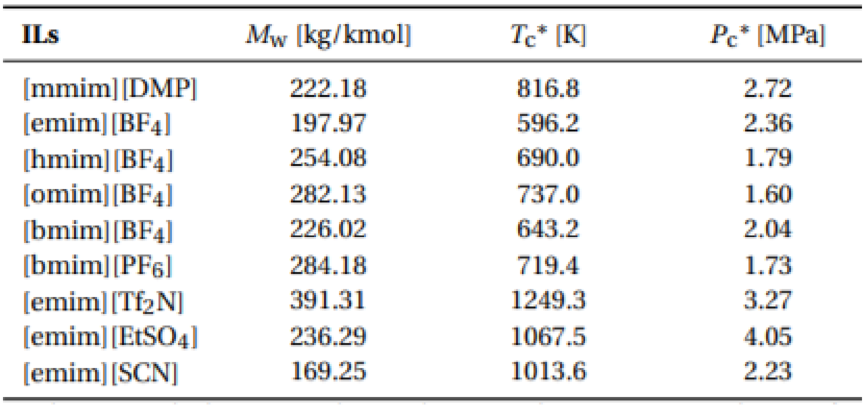

ILs	M_W [kg/kmol]	T_c* [K]	P_c* [MPa]
[mmim][DMP]	222.18	816.8	2.72
[emim][BF_4]	197.97	596.2	2.36
[hmim][BF_4]	254.08	690.0	1.79
[omim][BF_4]	282.13	737.0	1.60
[bmim][BF_4]	226.02	643.2	2.04
[bmim][PF_6]	284.18	719.4	1.73
[emim][Tf_2N]	391.31	1249.3	3.27
[emim][$EtSO_4$]	236.29	1067.5	4.05
[emim][SCN]	169.25	1013.6	2.23

Figure 29: Critical conditions and molecular weight data for several ionic liquids (Wang, 2019)

The data of [emim][SCN] as displayed in figure 29 is used in the Matlab model in the present work.

7. NRTL coefficients correlated by Wang (2019) for different ammonia- ionic liquid working pairs

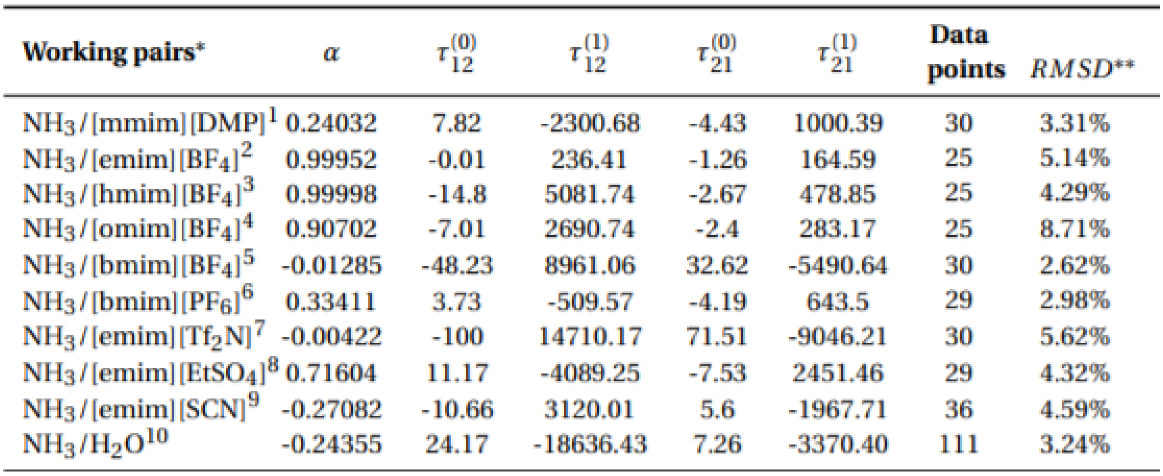

Working pairs*	α	$\tau_{12}^{(0)}$	$\tau_{12}^{(1)}$	$\tau_{21}^{(0)}$	$\tau_{21}^{(1)}$	Data points	$RMSD$**
NH_3/[mmim][DMP][1]	0.24032	7.82	-2300.68	-4.43	1000.39	30	3.31%
NH_3/[emim][BF_4][2]	0.99952	-0.01	236.41	-1.26	164.59	25	5.14%
NH_3/[hmim][BF_4][3]	0.99998	-14.8	5081.74	-2.67	478.85	25	4.29%
NH_3/[omim][BF_4][4]	0.90702	-7.01	2690.74	-2.4	283.17	25	8.71%
NH_3/[bmim][BF_4][5]	-0.01285	-48.23	8961.06	32.62	-5490.64	30	2.62%
NH_3/[bmim][PF_6][6]	0.33411	3.73	-509.57	-4.19	643.5	29	2.98%
NH_3/[emim][Tf_2N][7]	-0.00422	-100	14710.17	71.51	-9046.21	30	5.62%
NH_3/[emim][$EtSO_4$][8]	0.71604	11.17	-4089.25	-7.53	2451.46	29	4.32%
NH_3/[emim][SCN][9]	-0.27082	-10.66	3120.01	5.6	-1967.71	36	4.59%
NH_3/H_2O[10]	-0.24355	24.17	-18636.43	7.26	-3370.40	111	3.24%

Figure 30: Correlated NRTL coefficients for different ammonia - ionic liquid working pairs (Wang, 2019)

The data for [emim][SCN] displayed in figure 30 is used in the Matlab model designed in the present work.

8. *PTx* data for [emim][SCN] - ammonia working pair (Yokozeki and Shiflett, 2007)

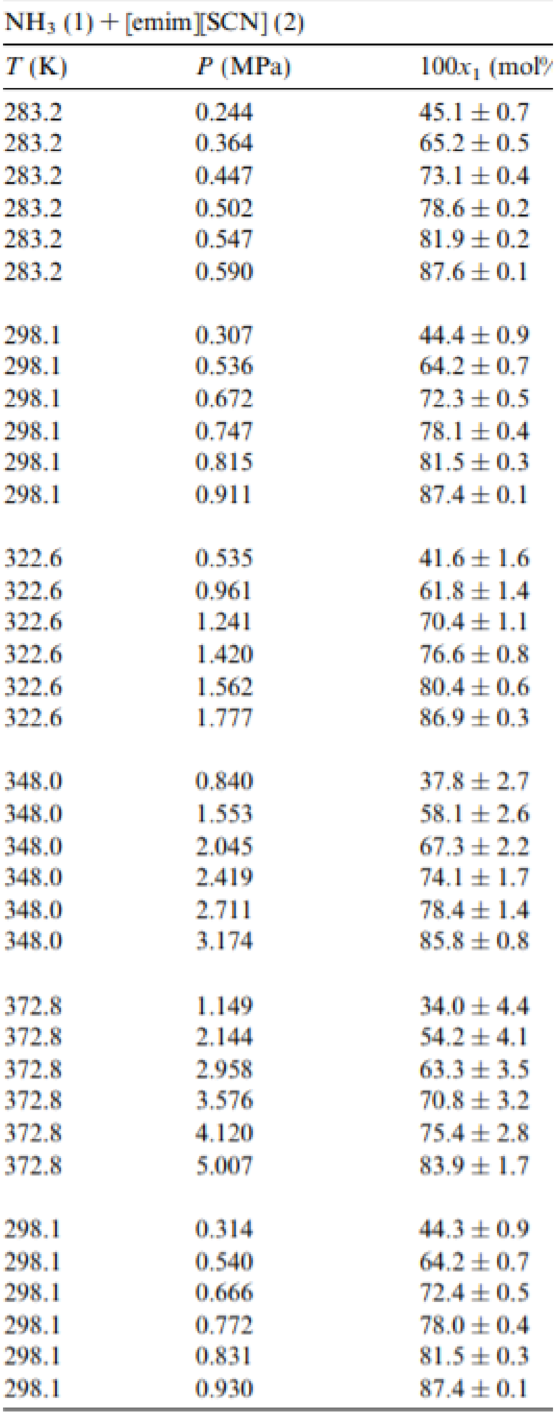

NH_3 (1) + [emim][SCN] (2)

T (K)	P (MPa)	$100x_1$ (mol%
283.2	0.244	45.1 ± 0.7
283.2	0.364	65.2 ± 0.5
283.2	0.447	73.1 ± 0.4
283.2	0.502	78.6 ± 0.2
283.2	0.547	81.9 ± 0.2
283.2	0.590	87.6 ± 0.1
298.1	0.307	44.4 ± 0.9
298.1	0.536	64.2 ± 0.7
298.1	0.672	72.3 ± 0.5
298.1	0.747	78.1 ± 0.4
298.1	0.815	81.5 ± 0.3
298.1	0.911	87.4 ± 0.1
322.6	0.535	41.6 ± 1.6
322.6	0.961	61.8 ± 1.4
322.6	1.241	70.4 ± 1.1
322.6	1.420	76.6 ± 0.8
322.6	1.562	80.4 ± 0.6
322.6	1.777	86.9 ± 0.3
348.0	0.840	37.8 ± 2.7
348.0	1.553	58.1 ± 2.6
348.0	2.045	67.3 ± 2.2
348.0	2.419	74.1 ± 1.7
348.0	2.711	78.4 ± 1.4
348.0	3.174	85.8 ± 0.8
372.8	1.149	34.0 ± 4.4
372.8	2.144	54.2 ± 4.1
372.8	2.958	63.3 ± 3.5
372.8	3.576	70.8 ± 3.2
372.8	4.120	75.4 ± 2.8
372.8	5.007	83.9 ± 1.7
298.1	0.314	44.3 ± 0.9
298.1	0.540	64.2 ± 0.7
298.1	0.666	72.4 ± 0.5
298.1	0.772	78.0 ± 0.4
298.1	0.831	81.5 ± 0.3
298.1	0.930	87.4 ± 0.1

Figure 31: *PTx* data for [emim][SCN] - ammonia working pair (Yokozeki and Shiflett, 2007)

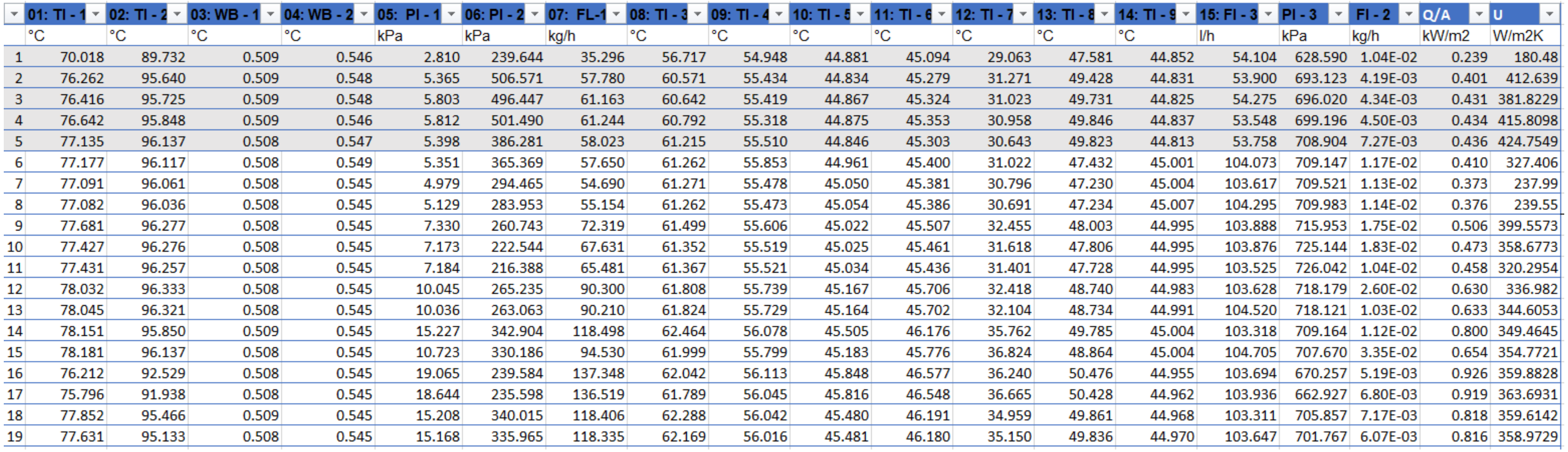

	01: TI - 1	02: TI - 2	03: WB - 1	04: WB - 2	05: PI - 1	06: PI - 2	07: FL-1	08: TI - 3	09: TI - 4	10: TI - 5	11: TI - 6	12: TI - 7	13: TI - 8	14: TI - 9	15: FI - 3	PI - 3	FI - 2	Q/A	U
	°C	°C	°C	°C	kPa	kPa	kg/h	°C	°C	°C	°C	°C	°C	°C	l/h	kPa	kg/h	kW/m2	W/m2K
1	70.018	89.732	0.509	0.546	2.810	239.644	35.296	56.717	54.948	44.881	45.094	29.063	47.581	44.852	54.104	628.590	1.04E-02	0.239	180.48
2	76.262	95.640	0.509	0.548	5.365	506.571	57.780	60.571	55.434	44.834	45.279	31.271	49.428	44.831	53.900	693.123	4.19E-03	0.401	412.639
3	76.416	95.725	0.509	0.548	5.803	496.447	61.163	60.642	55.419	44.867	45.324	31.023	49.731	44.825	54.275	696.020	4.34E-03	0.431	381.8229
4	76.642	95.848	0.509	0.546	5.812	501.490	61.244	60.792	55.318	44.875	45.353	30.958	49.846	44.837	53.548	699.196	4.50E-03	0.434	415.8098
5	77.135	96.137	0.508	0.547	5.398	386.281	58.023	61.215	55.510	44.846	45.303	30.643	49.823	44.813	53.758	708.904	7.27E-03	0.436	424.7549
6	77.177	96.117	0.508	0.549	5.351	365.369	57.650	61.262	55.853	44.961	45.400	31.022	47.432	45.001	104.073	709.147	1.17E-02	0.410	327.406
7	77.091	96.061	0.508	0.545	4.979	294.465	54.690	61.271	55.478	45.050	45.381	30.796	47.230	45.004	103.617	709.521	1.13E-02	0.373	237.99
8	77.082	96.036	0.508	0.545	5.129	283.953	55.154	61.262	55.473	45.054	45.386	30.691	47.234	45.007	104.295	709.983	1.14E-02	0.376	239.55
9	77.681	96.277	0.508	0.545	7.330	260.743	72.319	61.499	55.606	45.022	45.507	32.455	48.003	44.995	103.888	715.953	1.75E-02	0.506	399.5573
10	77.427	96.276	0.508	0.545	7.173	222.544	67.631	61.352	55.519	45.025	45.461	31.618	47.806	44.995	103.876	725.144	1.83E-02	0.473	358.6773
11	77.431	96.257	0.508	0.545	7.184	216.388	65.481	61.367	55.521	45.034	45.436	31.401	47.728	44.995	103.525	726.042	1.04E-02	0.458	320.2954
12	78.032	96.333	0.508	0.545	10.045	265.235	90.300	61.808	55.739	45.167	45.706	32.418	48.740	44.983	103.628	718.179	2.60E-02	0.630	336.982
13	78.045	96.321	0.508	0.545	10.036	263.063	90.210	61.824	55.729	45.164	45.702	32.104	48.734	44.991	104.520	718.121	1.03E-02	0.633	344.6053
14	78.151	95.850	0.509	0.545	15.227	342.904	118.498	62.464	56.078	45.505	46.176	35.762	49.785	45.004	103.318	709.164	1.12E-02	0.800	349.4645
15	78.181	96.137	0.508	0.545	10.723	330.186	94.530	61.999	55.799	45.183	45.776	36.824	48.864	45.004	104.705	707.670	3.35E-02	0.654	354.7721
16	76.212	92.529	0.508	0.545	19.065	239.584	137.348	62.042	56.113	45.848	46.577	36.240	50.476	44.955	103.694	670.257	5.19E-03	0.926	359.8828
17	75.796	91.938	0.508	0.545	18.644	235.598	136.519	61.789	56.045	45.816	46.548	36.665	50.428	44.962	103.936	662.927	6.80E-03	0.919	363.6931
18	77.852	95.466	0.509	0.545	15.208	340.015	118.406	62.288	56.042	45.480	46.191	34.959	49.861	44.968	103.311	705.857	7.17E-03	0.818	359.6142
19	77.631	95.133	0.508	0.545	15.168	335.965	118.335	62.169	56.016	45.481	46.180	35.150	49.836	44.970	103.647	701.767	6.07E-03	0.816	358.9729

Figure 32: Stage 2 experimental data

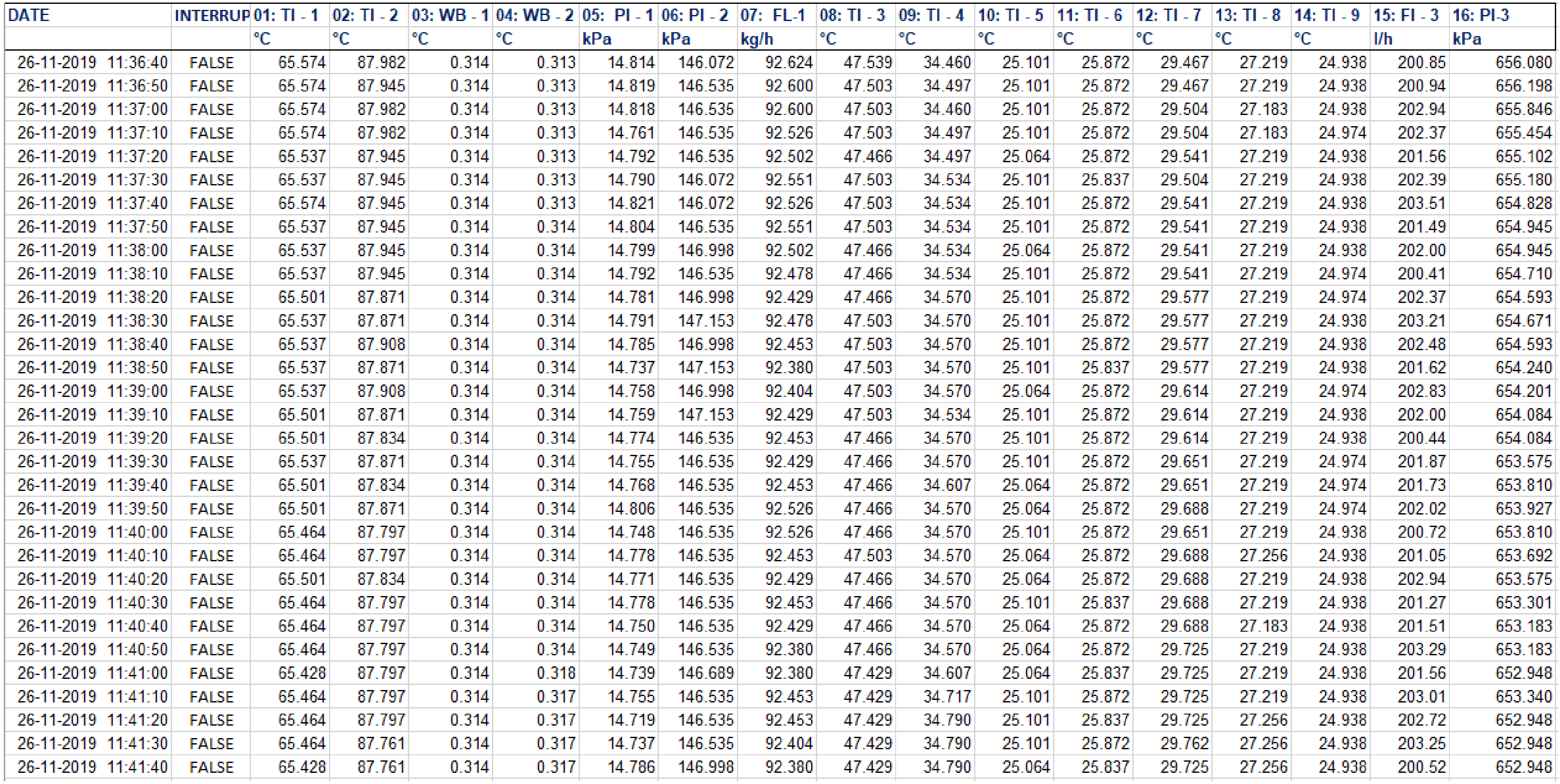

DATE	INTERRUP	01: TI - 1	02: TI - 2	03: WB - 1	04: WB - 2	05: PI - 1	06: PI - 2	07: FL-1	08: TI - 3	09: TI - 4	10: TI - 5	11: TI - 6	12: TI - 7	13: TI - 8	14: TI - 9	15: FI - 3	16: PI-3
		°C	°C	°C	°C	kPa	kPa	kg/h	°C	°C	°C	°C	°C	°C	°C	l/h	kPa
26-11-2019 11:36:40	FALSE	65.574	87.982	0.314	0.313	14.814	146.072	92.624	47.539	34.460	25.101	25.872	29.467	27.219	24.938	200.85	656.080
26-11-2019 11:36:50	FALSE	65.574	87.945	0.314	0.313	14.819	146.535	92.600	47.503	34.497	25.101	25.872	29.467	27.219	24.938	200.94	656.198
26-11-2019 11:37:00	FALSE	65.574	87.982	0.314	0.313	14.818	146.535	92.600	47.503	34.460	25.101	25.872	29.504	27.183	24.938	202.94	655.846
26-11-2019 11:37:10	FALSE	65.574	87.982	0.314	0.313	14.761	146.535	92.526	47.503	34.497	25.101	25.872	29.504	27.183	24.974	202.37	655.454
26-11-2019 11:37:20	FALSE	65.537	87.945	0.314	0.313	14.792	146.535	92.502	47.466	34.497	25.064	25.872	29.541	27.219	24.938	201.56	655.102
26-11-2019 11:37:30	FALSE	65.537	87.945	0.314	0.313	14.790	146.072	92.551	47.503	34.534	25.101	25.837	29.504	27.219	24.938	202.39	655.180
26-11-2019 11:37:40	FALSE	65.574	87.945	0.314	0.313	14.821	146.072	92.526	47.503	34.534	25.101	25.872	29.541	27.219	24.938	203.51	654.828
26-11-2019 11:37:50	FALSE	65.537	87.945	0.314	0.314	14.804	146.535	92.551	47.503	34.534	25.101	25.872	29.541	27.219	24.938	201.49	654.945
26-11-2019 11:38:00	FALSE	65.537	87.945	0.314	0.314	14.799	146.998	92.502	47.466	34.534	25.064	25.872	29.541	27.219	24.938	202.00	654.945
26-11-2019 11:38:10	FALSE	65.537	87.945	0.314	0.314	14.792	146.535	92.478	47.466	34.534	25.101	25.872	29.541	27.219	24.974	200.41	654.710
26-11-2019 11:38:20	FALSE	65.501	87.871	0.314	0.314	14.781	146.998	92.429	47.466	34.570	25.101	25.872	29.577	27.219	24.974	202.37	654.593
26-11-2019 11:38:30	FALSE	65.537	87.871	0.314	0.314	14.791	147.153	92.478	47.503	34.570	25.101	25.872	29.577	27.219	24.938	203.21	654.671
26-11-2019 11:38:40	FALSE	65.537	87.908	0.314	0.314	14.785	146.998	92.453	47.503	34.570	25.101	25.872	29.577	27.219	24.938	202.48	654.593
26-11-2019 11:38:50	FALSE	65.537	87.871	0.314	0.314	14.737	147.153	92.380	47.503	34.570	25.101	25.837	29.577	27.219	24.938	201.62	654.240
26-11-2019 11:39:00	FALSE	65.537	87.908	0.314	0.314	14.758	146.998	92.404	47.503	34.570	25.064	25.872	29.614	27.219	24.974	202.83	654.201
26-11-2019 11:39:10	FALSE	65.501	87.871	0.314	0.314	14.759	147.153	92.429	47.503	34.534	25.101	25.872	29.614	27.219	24.938	202.00	654.084
26-11-2019 11:39:20	FALSE	65.501	87.834	0.314	0.314	14.774	146.535	92.453	47.466	34.570	25.101	25.872	29.614	27.219	24.938	200.44	654.084
26-11-2019 11:39:30	FALSE	65.537	87.871	0.314	0.314	14.755	146.535	92.429	47.466	34.570	25.101	25.872	29.651	27.219	24.974	201.87	653.575
26-11-2019 11:39:40	FALSE	65.501	87.834	0.314	0.314	14.768	146.535	92.453	47.466	34.607	25.064	25.872	29.651	27.219	24.974	201.73	653.810
26-11-2019 11:39:50	FALSE	65.501	87.871	0.314	0.314	14.806	146.535	92.526	47.466	34.570	25.064	25.872	29.688	27.219	24.974	202.02	653.927
26-11-2019 11:40:00	FALSE	65.464	87.797	0.314	0.314	14.748	146.535	92.526	47.466	34.570	25.101	25.872	29.651	27.219	24.938	200.72	653.810
26-11-2019 11:40:10	FALSE	65.464	87.797	0.314	0.314	14.778	146.535	92.453	47.503	34.570	25.064	25.872	29.688	27.256	24.938	201.05	653.692
26-11-2019 11:40:20	FALSE	65.501	87.834	0.314	0.314	14.771	146.535	92.429	47.466	34.570	25.064	25.872	29.688	27.219	24.938	202.94	653.575
26-11-2019 11:40:30	FALSE	65.464	87.797	0.314	0.314	14.778	146.535	92.453	47.466	34.570	25.101	25.837	29.688	27.219	24.938	201.27	653.301
26-11-2019 11:40:40	FALSE	65.464	87.797	0.314	0.314	14.750	146.535	92.429	47.466	34.570	25.064	25.872	29.688	27.183	24.938	201.51	653.183
26-11-2019 11:40:50	FALSE	65.464	87.797	0.314	0.314	14.749	146.535	92.380	47.466	34.570	25.064	25.872	29.725	27.219	24.938	203.29	653.183
26-11-2019 11:41:00	FALSE	65.428	87.797	0.314	0.318	14.739	146.689	92.380	47.429	34.607	25.064	25.837	29.725	27.219	24.938	201.56	652.948
26-11-2019 11:41:10	FALSE	65.464	87.797	0.314	0.317	14.755	146.535	92.453	47.429	34.717	25.101	25.872	29.725	27.219	24.938	203.01	653.340
26-11-2019 11:41:20	FALSE	65.464	87.797	0.314	0.317	14.719	146.535	92.453	47.429	34.790	25.101	25.837	29.725	27.256	24.938	202.72	652.948
26-11-2019 11:41:30	FALSE	65.464	87.761	0.314	0.317	14.737	146.535	92.404	47.429	34.790	25.101	25.872	29.762	27.256	24.938	203.25	652.948
26-11-2019 11:41:40	FALSE	65.428	87.761	0.314	0.317	14.786	146.998	92.380	47.429	34.790	25.064	25.837	29.725	27.256	24.938	200.52	652.948

Figure 33: First five minutes of the experimental data used in data case 1 for the viscosity check

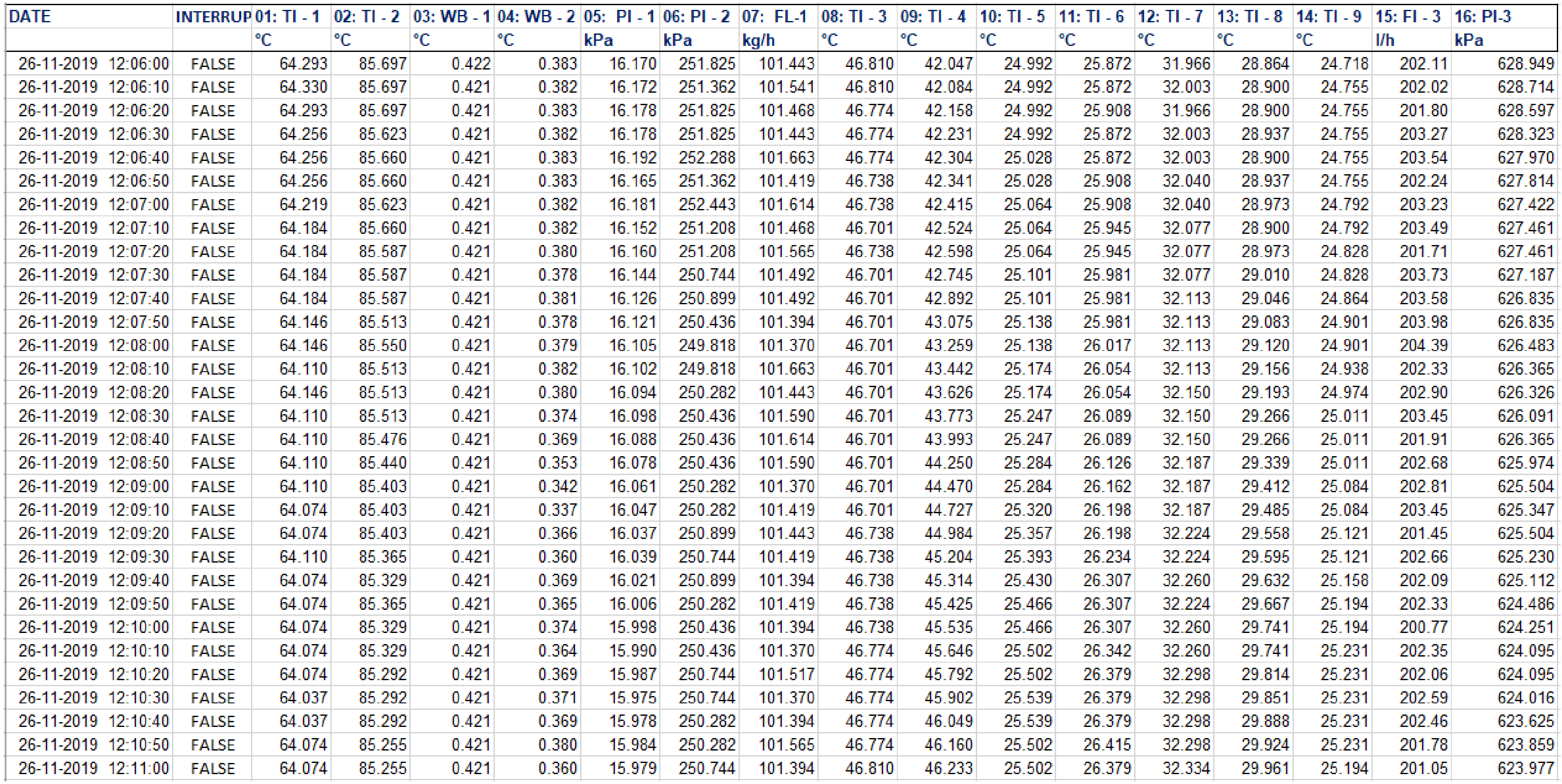

DATE	INTERRUP	01: TI - 1	02: TI - 2	03: WB - 1	04: WB - 2	05: PI - 1	06: PI - 2	07: FL-1	08: TI - 3	09: TI - 4	10: TI - 5	11: TI - 6	12: TI - 7	13: TI - 8	14: TI - 9	15: FI - 3	16: PI-3
		°C	°C	°C	°C	kPa	kPa	kg/h	°C	°C	°C	°C	°C	°C	°C	l/h	kPa
26-11-2019 12:06:00	FALSE	64.293	85.697	0.422	0.383	16.170	251.825	101.443	46.810	42.047	24.992	25.872	31.966	28.864	24.718	202.11	628.949
26-11-2019 12:06:10	FALSE	64.330	85.697	0.421	0.382	16.172	251.362	101.541	46.810	42.084	24.992	25.872	32.003	28.900	24.755	202.02	628.714
26-11-2019 12:06:20	FALSE	64.293	85.697	0.421	0.383	16.178	251.825	101.468	46.774	42.158	24.992	25.908	31.966	28.900	24.755	201.80	628.597
26-11-2019 12:06:30	FALSE	64.256	85.623	0.421	0.382	16.178	251.825	101.443	46.774	42.231	24.992	25.872	32.003	28.937	24.755	203.27	628.323
26-11-2019 12:06:40	FALSE	64.256	85.660	0.421	0.383	16.192	252.288	101.663	46.774	42.304	25.028	25.872	32.003	28.900	24.755	203.54	627.970
26-11-2019 12:06:50	FALSE	64.256	85.660	0.421	0.383	16.165	251.362	101.419	46.738	42.341	25.028	25.908	32.040	28.937	24.755	202.24	627.814
26-11-2019 12:07:00	FALSE	64.219	85.623	0.421	0.382	16.181	252.443	101.614	46.738	42.415	25.064	25.908	32.040	28.973	24.792	203.23	627.422
26-11-2019 12:07:10	FALSE	64.184	85.660	0.421	0.382	16.152	251.208	101.468	46.701	42.524	25.064	25.945	32.077	28.900	24.792	203.49	627.461
26-11-2019 12:07:20	FALSE	64.184	85.587	0.421	0.380	16.160	251.208	101.565	46.738	42.598	25.064	25.945	32.077	28.973	24.828	201.71	627.461
26-11-2019 12:07:30	FALSE	64.184	85.587	0.421	0.378	16.144	250.744	101.492	46.701	42.745	25.101	25.981	32.077	29.010	24.828	203.73	627.187
26-11-2019 12:07:40	FALSE	64.184	85.587	0.421	0.381	16.126	250.899	101.492	46.701	42.892	25.101	25.981	32.113	29.046	24.864	203.58	626.835
26-11-2019 12:07:50	FALSE	64.146	85.513	0.421	0.378	16.121	250.436	101.394	46.701	43.075	25.138	25.981	32.113	29.083	24.901	203.98	626.835
26-11-2019 12:08:00	FALSE	64.146	85.550	0.421	0.379	16.105	249.818	101.370	46.701	43.259	25.138	26.017	32.113	29.120	24.901	204.39	626.483
26-11-2019 12:08:10	FALSE	64.110	85.513	0.421	0.382	16.102	249.818	101.663	46.701	43.442	25.174	26.054	32.113	29.156	24.938	202.33	626.365
26-11-2019 12:08:20	FALSE	64.146	85.513	0.421	0.380	16.094	250.282	101.443	46.701	43.626	25.174	26.054	32.150	29.193	24.974	202.90	626.326
26-11-2019 12:08:30	FALSE	64.110	85.513	0.421	0.374	16.098	250.436	101.590	46.701	43.773	25.247	26.089	32.150	29.266	25.011	203.45	626.091
26-11-2019 12:08:40	FALSE	64.110	85.476	0.421	0.369	16.088	250.436	101.614	46.701	43.993	25.247	26.089	32.150	29.266	25.011	201.91	626.365
26-11-2019 12:08:50	FALSE	64.110	85.440	0.421	0.353	16.078	250.436	101.590	46.701	44.250	25.284	26.126	32.187	29.339	25.011	202.68	625.974
26-11-2019 12:09:00	FALSE	64.110	85.403	0.421	0.342	16.061	250.282	101.370	46.701	44.470	25.284	26.162	32.187	29.412	25.084	202.81	625.504
26-11-2019 12:09:10	FALSE	64.074	85.403	0.421	0.337	16.047	250.282	101.419	46.701	44.727	25.320	26.198	32.187	29.485	25.084	203.45	625.347
26-11-2019 12:09:20	FALSE	64.074	85.403	0.421	0.366	16.037	250.899	101.443	46.738	44.984	25.357	26.198	32.224	29.558	25.121	201.45	625.504
26-11-2019 12:09:30	FALSE	64.110	85.365	0.421	0.360	16.039	250.744	101.419	46.738	45.204	25.393	26.234	32.224	29.595	25.121	202.66	625.230
26-11-2019 12:09:40	FALSE	64.074	85.329	0.421	0.369	16.021	250.899	101.394	46.738	45.314	25.430	26.307	32.260	29.632	25.158	202.09	625.112
26-11-2019 12:09:50	FALSE	64.074	85.365	0.421	0.365	16.006	250.282	101.419	46.738	45.425	25.466	26.307	32.224	29.667	25.194	202.33	624.486
26-11-2019 12:10:00	FALSE	64.074	85.329	0.421	0.374	15.998	250.436	101.394	46.738	45.535	25.466	26.307	32.260	29.741	25.194	200.77	624.251
26-11-2019 12:10:10	FALSE	64.074	85.329	0.421	0.364	15.990	250.436	101.370	46.774	45.646	25.502	26.342	32.260	29.741	25.231	202.35	624.095
26-11-2019 12:10:20	FALSE	64.074	85.292	0.421	0.369	15.987	250.744	101.517	46.774	45.792	25.502	26.379	32.298	29.814	25.231	202.06	624.095
26-11-2019 12:10:30	FALSE	64.037	85.292	0.421	0.371	15.975	250.744	101.370	46.774	45.902	25.539	26.379	32.298	29.851	25.231	202.59	624.016
26-11-2019 12:10:40	FALSE	64.037	85.292	0.421	0.369	15.978	250.282	101.394	46.774	46.049	25.539	26.379	32.298	29.888	25.231	202.46	623.625
26-11-2019 12:10:50	FALSE	64.074	85.255	0.421	0.380	15.984	250.282	101.565	46.774	46.160	25.502	26.415	32.298	29.924	25.231	201.78	623.859
26-11-2019 12:11:00	FALSE	64.074	85.255	0.421	0.360	15.979	250.744	101.394	46.810	46.233	25.502	26.379	32.334	29.961	25.194	201.05	623.977

Figure 34: First five minutes of the experimental data used in data case 2 for the viscosity check

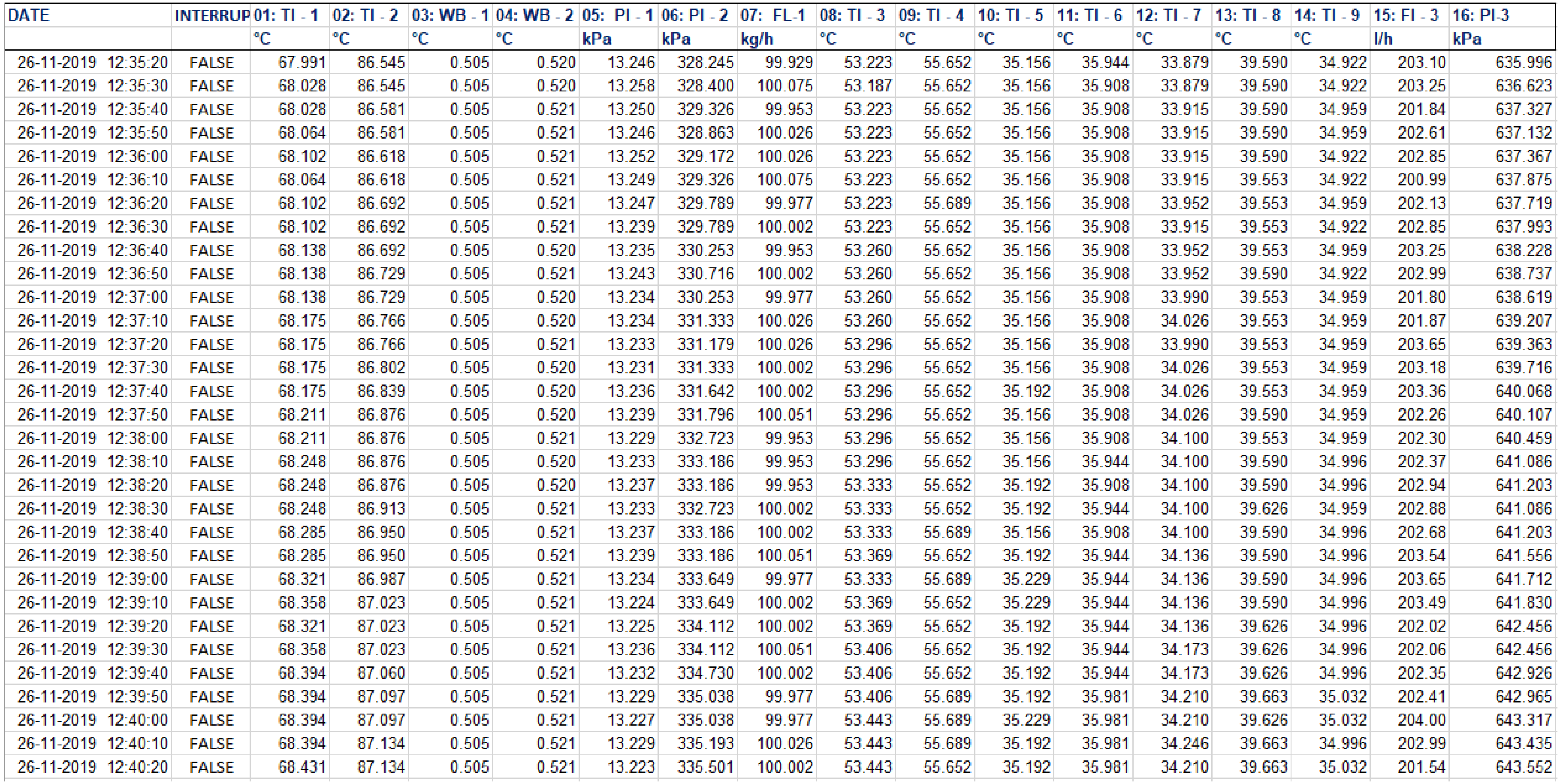

DATE	INTERRUP	01: TI - 1	02: TI - 2	03: WB - 1	04: WB - 2	05: PI - 1	06: PI - 2	07: FL-1	08: TI - 3	09: TI - 4	10: TI - 5	11: TI - 6	12: TI - 7	13: TI - 8	14: TI - 9	15: FI - 3	16: PI-3
		°C	°C	°C	°C	kPa	kPa	kg/h	°C	°C	°C	°C	°C	°C	°C	l/h	kPa
26-11-2019 12:35:20	FALSE	67.991	86.545	0.505	0.520	13.246	328.245	99.929	53.223	55.652	35.156	35.944	33.879	39.590	34.922	203.10	635.996
26-11-2019 12:35:30	FALSE	68.028	86.545	0.505	0.520	13.258	328.400	100.075	53.187	55.652	35.156	35.908	33.879	39.590	34.922	203.25	636.623
26-11-2019 12:35:40	FALSE	68.028	86.581	0.505	0.521	13.250	329.326	99.953	53.223	55.652	35.156	35.908	33.915	39.590	34.959	201.84	637.327
26-11-2019 12:35:50	FALSE	68.064	86.581	0.505	0.521	13.246	328.863	100.026	53.223	55.652	35.156	35.908	33.915	39.590	34.959	202.61	637.132
26-11-2019 12:36:00	FALSE	68.102	86.618	0.505	0.521	13.252	329.172	100.026	53.223	55.652	35.156	35.908	33.915	39.590	34.922	202.85	637.367
26-11-2019 12:36:10	FALSE	68.064	86.618	0.505	0.521	13.249	329.326	100.075	53.223	55.652	35.156	35.908	33.915	39.553	34.922	200.99	637.875
26-11-2019 12:36:20	FALSE	68.102	86.692	0.505	0.521	13.247	329.789	99.977	53.223	55.689	35.156	35.908	33.952	39.553	34.959	202.13	637.719
26-11-2019 12:36:30	FALSE	68.102	86.692	0.505	0.521	13.239	329.789	100.002	53.223	55.652	35.156	35.908	33.915	39.553	34.922	202.85	637.993
26-11-2019 12:36:40	FALSE	68.138	86.692	0.505	0.520	13.235	330.253	99.953	53.260	55.652	35.156	35.908	33.952	39.553	34.959	203.25	638.228
26-11-2019 12:36:50	FALSE	68.138	86.729	0.505	0.521	13.243	330.716	100.002	53.260	55.652	35.156	35.908	33.952	39.590	34.922	202.99	638.737
26-11-2019 12:37:00	FALSE	68.138	86.729	0.505	0.520	13.234	330.253	99.977	53.260	55.652	35.156	35.908	33.990	39.553	34.959	201.80	638.619
26-11-2019 12:37:10	FALSE	68.175	86.766	0.505	0.520	13.234	331.333	100.026	53.260	55.652	35.156	35.908	34.026	39.553	34.959	201.87	639.207
26-11-2019 12:37:20	FALSE	68.175	86.766	0.505	0.521	13.233	331.179	100.026	53.296	55.652	35.156	35.908	33.990	39.553	34.959	203.65	639.363
26-11-2019 12:37:30	FALSE	68.175	86.802	0.505	0.520	13.231	331.333	100.002	53.296	55.652	35.156	35.908	34.026	39.553	34.959	203.18	639.716
26-11-2019 12:37:40	FALSE	68.175	86.839	0.505	0.520	13.236	331.642	100.002	53.296	55.652	35.192	35.908	34.026	39.553	34.959	203.36	640.068
26-11-2019 12:37:50	FALSE	68.211	86.876	0.505	0.520	13.239	331.796	100.051	53.296	55.652	35.156	35.908	34.026	39.590	34.959	202.26	640.107
26-11-2019 12:38:00	FALSE	68.211	86.876	0.505	0.521	13.229	332.723	99.953	53.296	55.652	35.156	35.908	34.100	39.553	34.959	202.30	640.459
26-11-2019 12:38:10	FALSE	68.248	86.876	0.505	0.520	13.233	333.186	99.953	53.296	55.652	35.156	35.944	34.100	39.590	34.996	202.37	641.086
26-11-2019 12:38:20	FALSE	68.248	86.876	0.505	0.520	13.237	333.186	99.953	53.333	55.652	35.192	35.908	34.100	39.590	34.996	202.94	641.203
26-11-2019 12:38:30	FALSE	68.248	86.913	0.505	0.521	13.233	332.723	100.002	53.333	55.652	35.192	35.944	34.100	39.626	34.959	202.88	641.086
26-11-2019 12:38:40	FALSE	68.285	86.950	0.505	0.521	13.237	333.186	100.002	53.333	55.689	35.156	35.908	34.100	39.590	34.996	202.68	641.203
26-11-2019 12:38:50	FALSE	68.285	86.950	0.505	0.521	13.239	333.186	100.051	53.369	55.652	35.192	35.944	34.136	39.590	34.996	203.54	641.556
26-11-2019 12:39:00	FALSE	68.321	86.987	0.505	0.521	13.234	333.649	99.977	53.333	55.689	35.229	35.944	34.136	39.590	34.996	203.65	641.712
26-11-2019 12:39:10	FALSE	68.358	87.023	0.505	0.521	13.224	333.649	100.002	53.369	55.652	35.229	35.944	34.136	39.590	34.996	203.49	641.830
26-11-2019 12:39:20	FALSE	68.321	87.023	0.505	0.521	13.225	334.112	100.002	53.369	55.652	35.192	35.944	34.136	39.626	34.996	202.02	642.456
26-11-2019 12:39:30	FALSE	68.358	87.023	0.505	0.521	13.236	334.112	100.051	53.406	55.652	35.192	35.944	34.173	39.626	34.996	202.06	642.456
26-11-2019 12:39:40	FALSE	68.394	87.060	0.505	0.521	13.232	334.730	100.002	53.406	55.652	35.192	35.944	34.173	39.626	34.996	202.35	642.926
26-11-2019 12:39:50	FALSE	68.394	87.097	0.505	0.521	13.229	335.038	99.977	53.406	55.689	35.192	35.981	34.210	39.663	35.032	202.41	642.965
26-11-2019 12:40:00	FALSE	68.394	87.097	0.505	0.521	13.227	335.038	99.977	53.443	55.689	35.229	35.981	34.210	39.626	35.032	204.00	643.317
26-11-2019 12:40:10	FALSE	68.394	87.134	0.505	0.521	13.229	335.193	100.026	53.443	55.689	35.192	35.981	34.246	39.663	34.996	202.99	643.435
26-11-2019 12:40:20	FALSE	68.431	87.134	0.505	0.521	13.223	335.501	100.002	53.443	55.652	35.192	35.981	34.210	39.663	35.032	201.54	643.552

Figure 35: First five minutes of the experimental data used in data case 3 for the viscosity check

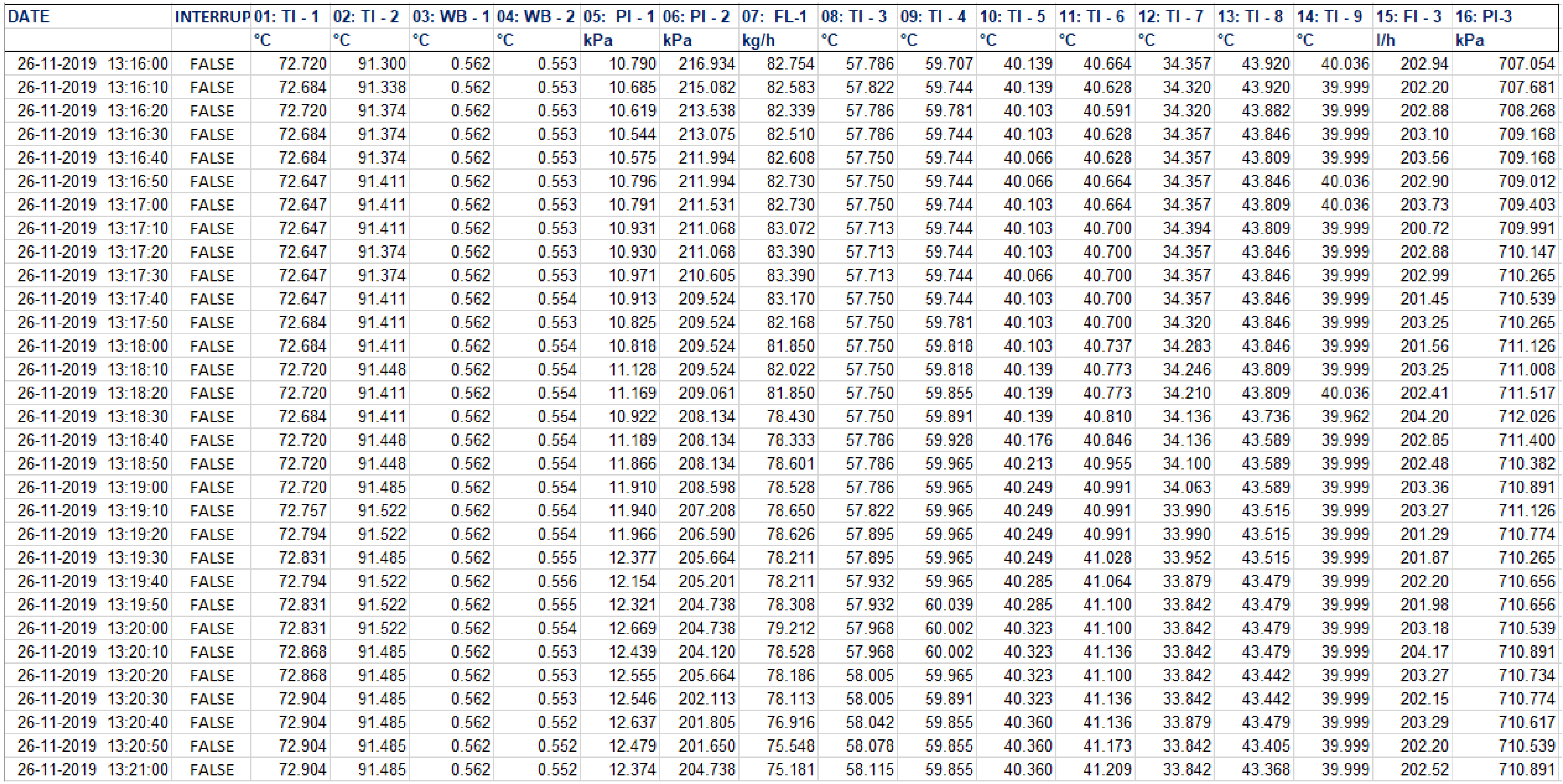

DATE	INTERRUP	01: TI - 1	02: TI - 2	03: WB - 1	04: WB - 2	05: PI - 1	06: PI - 2	07: FL-1	08: TI - 3	09: TI - 4	10: TI - 5	11: TI - 6	12: TI - 7	13: TI - 8	14: TI - 9	15: FI - 3	16: PI-3
		°C	°C	°C	°C	kPa	kPa	kg/h	°C	°C	°C	°C	°C	°C	°C	l/h	kPa
26-11-2019 13:16:00	FALSE	72.720	91.300	0.562	0.553	10.790	216.934	82.754	57.786	59.707	40.139	40.664	34.357	43.920	40.036	202.94	707.054
26-11-2019 13:16:10	FALSE	72.684	91.338	0.562	0.553	10.685	215.082	82.583	57.822	59.744	40.139	40.628	34.320	43.920	39.999	202.20	707.681
26-11-2019 13:16:20	FALSE	72.720	91.374	0.562	0.553	10.619	213.538	82.339	57.786	59.781	40.103	40.591	34.320	43.882	39.999	202.88	708.268
26-11-2019 13:16:30	FALSE	72.684	91.374	0.562	0.553	10.544	213.075	82.510	57.786	59.744	40.103	40.628	34.357	43.846	39.999	203.10	709.168
26-11-2019 13:16:40	FALSE	72.684	91.374	0.562	0.553	10.575	211.994	82.608	57.750	59.744	40.066	40.628	34.357	43.809	39.999	203.56	709.168
26-11-2019 13:16:50	FALSE	72.647	91.411	0.562	0.553	10.796	211.994	82.730	57.750	59.744	40.066	40.664	34.357	43.846	40.036	202.90	709.012
26-11-2019 13:17:00	FALSE	72.647	91.411	0.562	0.553	10.791	211.531	82.730	57.750	59.744	40.103	40.664	34.357	43.809	40.036	203.73	709.403
26-11-2019 13:17:10	FALSE	72.647	91.411	0.562	0.553	10.931	211.068	83.072	57.713	59.744	40.103	40.700	34.394	43.809	39.999	200.72	709.991
26-11-2019 13:17:20	FALSE	72.647	91.374	0.562	0.553	10.930	211.068	83.390	57.713	59.744	40.103	40.700	34.357	43.846	39.999	202.88	710.147
26-11-2019 13:17:30	FALSE	72.647	91.374	0.562	0.553	10.971	210.605	83.390	57.713	59.744	40.066	40.700	34.357	43.846	39.999	202.99	710.265
26-11-2019 13:17:40	FALSE	72.647	91.411	0.562	0.554	10.913	209.524	83.170	57.750	59.744	40.103	40.700	34.357	43.846	39.999	201.45	710.539
26-11-2019 13:17:50	FALSE	72.684	91.411	0.562	0.553	10.825	209.524	82.168	57.750	59.781	40.103	40.700	34.320	43.846	39.999	203.25	710.265
26-11-2019 13:18:00	FALSE	72.684	91.411	0.562	0.554	10.818	209.524	81.850	57.750	59.818	40.103	40.737	34.283	43.846	39.999	201.56	711.126
26-11-2019 13:18:10	FALSE	72.720	91.448	0.562	0.554	11.128	209.524	82.022	57.750	59.818	40.139	40.773	34.246	43.809	39.999	203.25	711.008
26-11-2019 13:18:20	FALSE	72.720	91.411	0.562	0.554	11.169	209.061	81.850	57.750	59.855	40.139	40.773	34.210	43.809	40.036	202.41	711.517
26-11-2019 13:18:30	FALSE	72.684	91.411	0.562	0.554	10.922	208.134	78.430	57.750	59.891	40.139	40.810	34.136	43.736	39.962	204.20	712.026
26-11-2019 13:18:40	FALSE	72.720	91.448	0.562	0.554	11.189	208.134	78.333	57.786	59.928	40.176	40.846	34.136	43.589	39.999	202.85	711.400
26-11-2019 13:18:50	FALSE	72.720	91.448	0.562	0.554	11.866	208.134	78.601	57.786	59.965	40.213	40.955	34.100	43.589	39.999	202.48	710.382
26-11-2019 13:19:00	FALSE	72.720	91.485	0.562	0.554	11.910	208.598	78.528	57.786	59.965	40.249	40.991	34.063	43.589	39.999	203.36	710.891
26-11-2019 13:19:10	FALSE	72.757	91.522	0.562	0.554	11.940	207.208	78.650	57.822	59.965	40.249	40.991	33.990	43.515	39.999	203.27	711.126
26-11-2019 13:19:20	FALSE	72.794	91.522	0.562	0.554	11.966	206.590	78.626	57.895	59.965	40.249	40.991	33.990	43.515	39.999	201.29	710.774
26-11-2019 13:19:30	FALSE	72.831	91.485	0.562	0.555	12.377	205.664	78.211	57.895	59.965	40.249	41.028	33.952	43.515	39.999	201.87	710.265
26-11-2019 13:19:40	FALSE	72.794	91.522	0.562	0.556	12.154	205.201	78.211	57.932	59.965	40.285	41.064	33.879	43.479	39.999	202.20	710.656
26-11-2019 13:19:50	FALSE	72.831	91.522	0.562	0.555	12.321	204.738	78.308	57.932	60.039	40.285	41.100	33.842	43.479	39.999	201.98	710.656
26-11-2019 13:20:00	FALSE	72.831	91.522	0.562	0.554	12.669	204.738	79.212	57.968	60.002	40.323	41.100	33.842	43.479	39.999	203.18	710.539
26-11-2019 13:20:10	FALSE	72.868	91.485	0.562	0.553	12.439	204.120	78.528	57.968	60.002	40.323	41.136	33.842	43.479	39.999	204.17	710.891
26-11-2019 13:20:20	FALSE	72.868	91.485	0.562	0.553	12.555	205.664	78.186	58.005	59.965	40.323	41.100	33.842	43.442	39.999	203.27	710.734
26-11-2019 13:20:30	FALSE	72.904	91.485	0.562	0.553	12.546	202.113	78.113	58.005	59.891	40.323	41.136	33.842	43.442	39.999	202.15	710.774
26-11-2019 13:20:40	FALSE	72.904	91.485	0.562	0.552	12.637	201.805	76.916	58.042	59.855	40.360	41.136	33.879	43.479	39.999	203.29	710.617
26-11-2019 13:20:50	FALSE	72.904	91.485	0.562	0.552	12.479	201.650	75.548	58.078	59.855	40.360	41.173	33.842	43.405	39.999	202.20	710.539
26-11-2019 13:21:00	FALSE	72.904	91.485	0.562	0.552	12.374	204.738	75.181	58.115	59.855	40.360	41.209	33.842	43.368	39.999	202.52	710.891

Figure 36: First five minutes of the experimental data used in data case 4 for the viscosity check

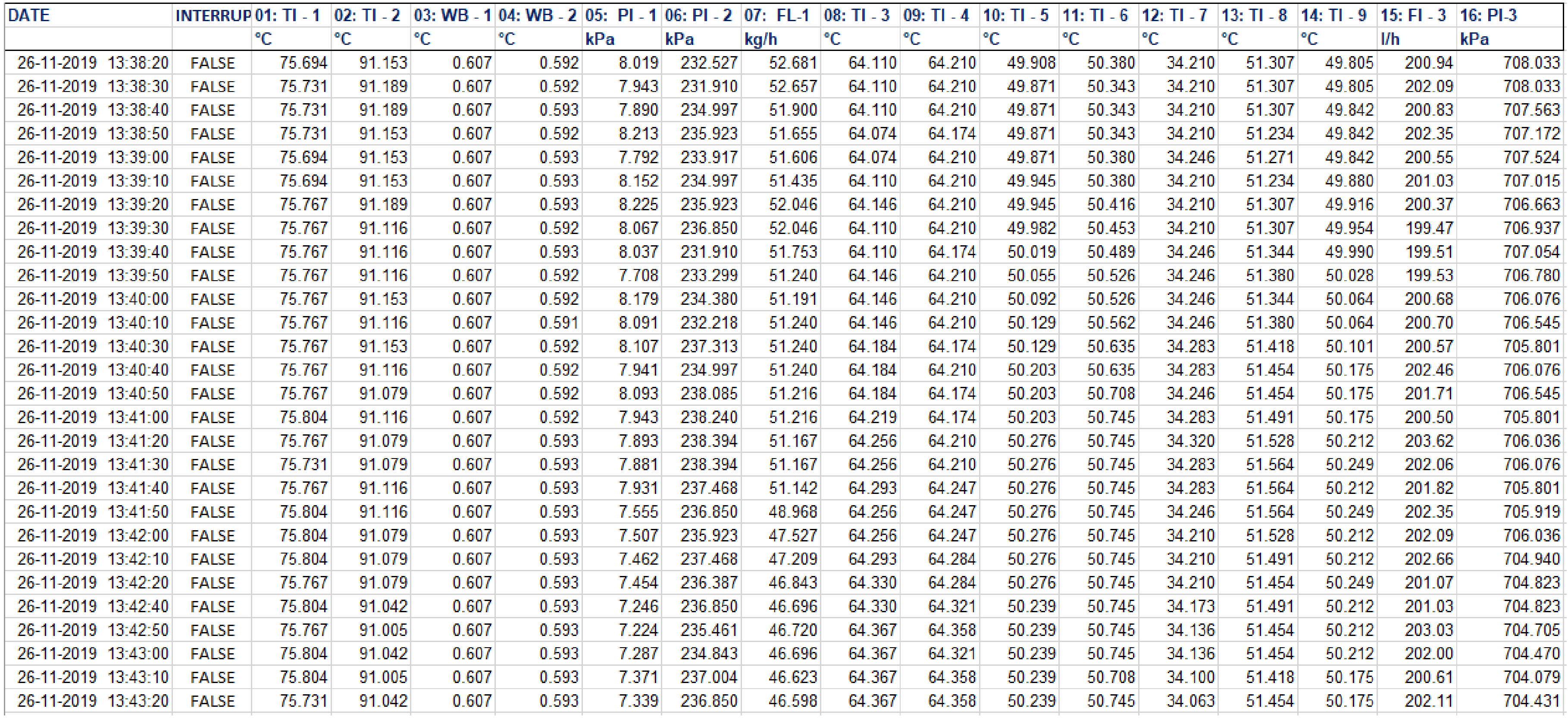

DATE	INTERRUP	01: TI - 1	02: TI - 2	03: WB - 1	04: WB - 2	05: PI - 1	06: PI - 2	07: FL-1	08: TI - 3	09: TI - 4	10: TI - 5	11: TI - 6	12: TI - 7	13: TI - 8	14: TI - 9	15: FI - 3	16: PI-3
		°C	°C	°C	°C	kPa	kPa	kg/h	°C	°C	°C	°C	°C	°C	°C	l/h	kPa
26-11-2019 13:38:20	FALSE	75.694	91.153	0.607	0.592	8.019	232.527	52.681	64.110	64.210	49.908	50.380	34.210	51.307	49.805	200.94	708.033
26-11-2019 13:38:30	FALSE	75.731	91.189	0.607	0.592	7.943	231.910	52.657	64.110	64.210	49.871	50.343	34.210	51.307	49.805	202.09	708.033
26-11-2019 13:38:40	FALSE	75.731	91.189	0.607	0.593	7.890	234.997	51.900	64.110	64.210	49.871	50.343	34.210	51.307	49.842	200.83	707.563
26-11-2019 13:38:50	FALSE	75.731	91.153	0.607	0.592	8.213	235.923	51.655	64.074	64.174	49.871	50.343	34.210	51.234	49.842	202.35	707.172
26-11-2019 13:39:00	FALSE	75.694	91.153	0.607	0.593	7.792	233.917	51.606	64.074	64.210	49.871	50.380	34.246	51.271	49.842	200.55	707.524
26-11-2019 13:39:10	FALSE	75.694	91.153	0.607	0.593	8.152	234.997	51.435	64.110	64.210	49.945	50.380	34.210	51.234	49.880	201.03	707.015
26-11-2019 13:39:20	FALSE	75.767	91.189	0.607	0.593	8.225	235.923	52.046	64.146	64.210	49.945	50.416	34.210	51.307	49.916	200.37	706.663
26-11-2019 13:39:30	FALSE	75.767	91.116	0.607	0.592	8.067	236.850	52.046	64.110	64.210	49.982	50.453	34.210	51.307	49.954	199.47	706.937
26-11-2019 13:39:40	FALSE	75.767	91.116	0.607	0.593	8.037	231.910	51.753	64.110	64.174	50.019	50.489	34.246	51.344	49.990	199.51	707.054
26-11-2019 13:39:50	FALSE	75.767	91.116	0.607	0.592	7.708	233.299	51.240	64.146	64.210	50.055	50.526	34.246	51.380	50.028	199.53	706.780
26-11-2019 13:40:00	FALSE	75.767	91.153	0.607	0.592	8.179	234.380	51.191	64.146	64.210	50.092	50.526	34.246	51.344	50.064	200.68	706.076
26-11-2019 13:40:10	FALSE	75.767	91.116	0.607	0.591	8.091	232.218	51.240	64.146	64.210	50.129	50.562	34.246	51.380	50.064	200.70	706.545
26-11-2019 13:40:30	FALSE	75.767	91.153	0.607	0.592	8.107	237.313	51.240	64.184	64.174	50.129	50.635	34.283	51.418	50.101	200.57	705.801
26-11-2019 13:40:40	FALSE	75.767	91.116	0.607	0.592	7.941	234.997	51.240	64.184	64.210	50.203	50.635	34.283	51.454	50.175	202.46	706.076
26-11-2019 13:40:50	FALSE	75.767	91.079	0.607	0.592	8.093	238.085	51.216	64.184	64.174	50.203	50.708	34.246	51.454	50.175	201.71	706.545
26-11-2019 13:41:00	FALSE	75.804	91.116	0.607	0.592	7.943	238.240	51.216	64.219	64.174	50.203	50.745	34.283	51.491	50.175	200.50	705.801
26-11-2019 13:41:20	FALSE	75.767	91.079	0.607	0.593	7.893	238.394	51.167	64.256	64.210	50.276	50.745	34.320	51.528	50.212	203.62	706.036
26-11-2019 13:41:30	FALSE	75.731	91.079	0.607	0.593	7.881	238.394	51.167	64.256	64.210	50.276	50.745	34.283	51.564	50.249	202.06	706.076
26-11-2019 13:41:40	FALSE	75.767	91.116	0.607	0.593	7.931	237.468	51.142	64.293	64.247	50.276	50.745	34.283	51.564	50.212	201.82	705.801
26-11-2019 13:41:50	FALSE	75.804	91.116	0.607	0.593	7.555	236.850	48.968	64.256	64.247	50.276	50.745	34.246	51.564	50.249	202.35	705.919
26-11-2019 13:42:00	FALSE	75.804	91.079	0.607	0.593	7.507	235.923	47.527	64.256	64.247	50.276	50.745	34.210	51.528	50.212	202.09	706.036
26-11-2019 13:42:10	FALSE	75.804	91.079	0.607	0.593	7.462	237.468	47.209	64.293	64.284	50.276	50.745	34.210	51.491	50.212	202.66	704.940
26-11-2019 13:42:20	FALSE	75.767	91.079	0.607	0.593	7.454	236.387	46.843	64.330	64.284	50.276	50.745	34.210	51.454	50.249	201.07	704.823
26-11-2019 13:42:40	FALSE	75.804	91.042	0.607	0.593	7.246	236.850	46.696	64.330	64.321	50.239	50.745	34.173	51.491	50.212	201.03	704.823
26-11-2019 13:42:50	FALSE	75.767	91.005	0.607	0.593	7.224	235.461	46.720	64.367	64.358	50.239	50.745	34.136	51.454	50.212	203.03	704.705
26-11-2019 13:43:00	FALSE	75.804	91.042	0.607	0.593	7.287	234.843	46.696	64.367	64.321	50.239	50.745	34.136	51.454	50.212	202.00	704.470
26-11-2019 13:43:10	FALSE	75.804	91.005	0.607	0.593	7.371	237.004	46.623	64.367	64.358	50.239	50.708	34.100	51.418	50.175	200.61	704.079
26-11-2019 13:43:20	FALSE	75.731	91.042	0.607	0.593	7.339	236.850	46.598	64.367	64.358	50.239	50.745	34.063	51.454	50.175	202.11	704.431

Figure 37: First five minutes of the experimental data used in data case 5 for the viscosity check